ADSORPTION AND SWITCHING OF SINGLE AZOBENZENE MOLECULES AT SILVER NANOHEMISPHERE FACETS STUDIED BY SURFACE−ENHANCED RAMAN SCATTERING

By

ÇAĞRI ÖZGE TOPAL

Bachelor of Science in Mechanical Engineering
Dokuz Eylul University
İzmir, Turkey
2006

Master of Science in Mechanical Engineering
Oklahoma State University
Stillwater, Oklahoma
2010

Submitted to the Faculty of the
Graduate College of the
Oklahoma State University
in partial fulfillment of
the requirements for
the Degree of
DOCTOR OF PHILOSOPHY
July, 2019

ADSORPTION AND SWITCHING OF SINGLE AZOBENZENE MOLECULES AT SILVER NANOHEMISPHERE FACETS STUDIED BY SURFACE−ENHANCED RAMAN SCATTERING

Dissertation Approved:

Dr. Heather Fahlenkamp

Committee Chair

Dr. Raman Singh

Dr. Sandip Harimkar

Dr. Nicholas Materer

ACKNOWLEDGEMENTS

I would like to thank everyone who have helped me throughout my PhD education. First of all, I would like to thank Dr. Heather Fahlenkamp for taking over as my committee chair and for guiding me in the completion of my dissertation. I also would like to thank Dr. Raman Singh, Dr. Sandip Harimkar, and Dr. Nicholas Materer for their time, contributions, and efforts through serving on my committee. The work described here was performed under the supervision of Dr. Kaan Kalkan. I would like acknowledge him for the resources and guidance he has provided to me.

Next, I would like to thank my family for their endless love, support, and encouragement. This work is dedicated to my parents Gülşen and Yusuf Topal, my twin brother Çaĝdaş Topal, my sister and my brother-in-law Duygu and Bora Kiriş and my niece Luna Kiriş.

I also would like to thank my dear friends, especially to Nicholas Flynn, Sriharsha Karumuri and Poornima Vijayakumar, who have always been there for me.

Finally, I would like to extend my sincere thanks to the College of Engineering, Architecture and Technology and to the Graduate College at Oklahoma State University for the opportunities provided to me.

Name: ÇAĞRI ÖZGE TOPAL

Date of Degree: JULY, 2019

Title of Study: ADSORPTION AND SWITCHING OF SINGLE AZOBENZENE
MOLECULES AT SILVER NANOHEMISPHERE FACETS STUDIED
BY SURFACE−ENHANCED RAMAN SCATTERING

Major Field: MECHANICAL ENGINEERING

Abstract: The promise of molecular machines to control mechanical and electronic components at atomic level has brought molecular switches to the spotlight in the last decade. Among many switching molecules, azobenzene (AB) is one of the most extensively studied owing to its chemical simplicity, and its efficient and reversible photoswitching between a *trans* (*t*-AB) and a *cis* (*c*-AB) form. Immobilization of AB on surfaces is needed for the precise design and control of molecular devices. However, preserving the switching of surface adsorbed AB has been a challenge. Hence, understanding the governing factors of the conformational dynamics of surface adsorbed AB has been a major interest. With the objective of understanding how AB interacts with metal surfaces, the present work studies the adsorption and switching of AB on a metal surface (i.e., Ag facets) at single molecule (SM) level by Surface-enhanced Raman Scattering (SERS).

In the present work, the SM-SERS measurements reveal three distinct species of both *t*-AB and *c*-AB on the surface of plasmonic Ag nanohemispheres (NHSs). With the help of DFT calculations, the observed SM-SERS jumps are assigned to surface adsorbates of *t*-AB and *c*-AB on three facets of different crystal orientation (i.e., (111), (100) and (110)) available on Ag NHSs. The experimental and computational results indicate that adsorption mechanism and the resulting adsorbate geometry of AB varies significantly on surfaces of different crystal orientation. The reversible photoswitching of AB molecules is also observed at single molecule level. The SM-SERS spectra exhibiting switching of AB indicate that surface decoupling of AB is required for switching of AB.

The Ag-on-Ge SERS substrates which provide SM sensitivity in the present study are also investigated. As experimentally demonstrated and computationally elucidated, NHSs exhibit remarkably different plasmonic characteristics as compared to nanospheres. The by asymmetric particle shape leads to dipolar modes parallel (in-plane) and normal to the base (out-of-plane), which are significantly different in terms of energy, excitation dependence on polarization, and electromagnetic coupling. The unique characteristics discovered in the present study point to potential applications of Ag-on-Ge substrates in various plasmonic applications, including photovoltaics, photocatalysis, UV plasmonics, and chemical detection (i.e., LSPR and SERS).

TABLE OF CONTENTS

LIST OF TABLES

LIST OF FIGURES

CHAPTER I

INTRODUCTION

In his famous 1959 visionary lecture, “There's Plenty of Room at the Bottom”, Richard Feymann gave a glimpse of a world which had yet to come. A world where precisely controlled “tiny” machines deliver drugs to specific tumor sites [1], light microscopes image live cells at a resolution beyond Abbe’s stipulated limit of 0.2 micrometers [2-8], molecular “arms” [9-13] synthesize or assemble molecules, “nanocars” [14] race against each other on a 100 nm-long race track made of gold atoms, molecules act as a lift or an artificial muscle [15, 16], and molecular on-and-off switches build 160-kilobit memory at a density of today’s commercial memory devices [17]. At the heart of many of these ground breaking innovations lie the molecular switches whose physical and/or chemical characteristics can be reversibly switched with an external stimuli, such as electric field, light, heat or changes in chemical environment (e.g., pH). While molecular switches have long fascinated researchers, the possibility of incorporating them into molecular devices in recent years have started a new wave of interest into understanding and controlling their switching properties.

Among many switching molecules, azobenzene (AB) is one of the most extensively studied owing to its chemical simplicity, and its efficient and reversible photoswitching between a planar *trans* form and a non-planar *cis* form (Figure 1.1a) [18-22]. Implementation of AB and its derivatives in molecular devices require immobilization and ordering on solid surfaces, such as close-packed coinage metals (i.e., Au, Ag, and Cu). However, this poses a challenge, since the adsorption onto surfaces may change the switching behavior of the molecules due to electronic interactions with the metal [23-29]. Hence, a better understanding of these interactions is required for the design of future molecular devices. This constitutes one the main goals of this dissertation; *studying the adsorption and switching of AB on a metal surface (i.e., Ag facets) at single molecule level by Surface-enhanced Raman Spectroscopy (SERS)* which is addressed in *Chapter IV*.

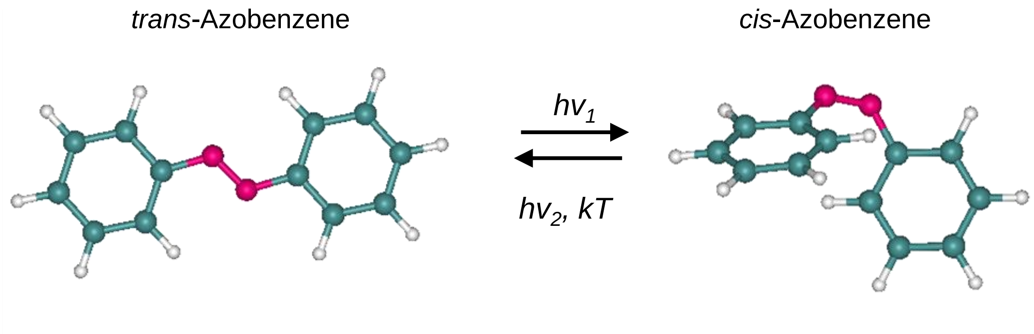

Figure 1.1. Ball-stick models showing planar *tran*-azobenzene (*t*-AB) and non-planar *cis*-azobenzene (*c*-AB). H: white, C: green, N: magenta.

SERS is a vibrational spectroscopy technique where the signal is amplified due to enhanced electromagnetic fields generated by surface plasmon resonances in metal nanoparticles. It inherently involves the adsorption of molecules onto metal nanoparticle (NP) surfaces (e.g., Au or Ag), and thus provides a platform to study the adsorption configuration and conformational dynamics of molecules on a metal surface. Further, vibrational frequencies are highly sensitive to changes in conformational modifications induced by the interaction of molecules with their environment (e.g., bonding or charge transfer), making SERS a powerful tool to study surface interactions of photoswitching molecules. In addition, studying molecules at single molecule (SM) level provides crucial information on the individual physical chemistry by resolving conformational and electronic states/transitions of single molecules in the absence of ensemble averaging.

As detailed in *Chapter IV*, the present work reveals six distinct adsorbate states of single AB molecules on Ag NPs by SERS. By the help of *ab initio* Density Functional Theory (DFT) calculations, these six different AB adsorbates are associated with three different crystal orientations of the Ag surface and two different isomers of AB (i.e., *trans* and *cis*). Further, *trans* ↔ *cis* photoswitching of AB is demonstrated on Ag NPs at SM level.

For the last 10 years, our group has used SERS to "watch single molecules in action" at time resolutions as high as 40 ms. For example, single photo-active yellow protein (PYP) proteins were captured in 1-s time resolution while the chromophore underwent protonation-deprotonation, as well as *cis* ↔ *trans* isomerization during the protein photocycle [30]. Most recently, the vibrational spectrum of a non-*cis* (i.e., non-planar) form of wild-type GFP chromophore was observed by SM-SERS [31]. The same study also resolved the transitions between the *cis* and the non-*cis* conformation, as well as the transitions between the protonated and deprotonated forms of both conformations in 50-100 ms intervals. In this dissertation, we continue our contribution to the SERS literature with our work on AB at SM level.

Our ability to resolve such dynamic events at single molecule level with such time-resolutions (i.e., 40-100 ms) relies on our plasmonic Ag-nanohemispheres-on-Ge-nanoposts substrates [30-33]. In recent years, exploring the plasmonic properties of these unique substrates have become an interest of our group not only from the SM-SERS perspective, but also from the perspective of plasmonic characteristics of such asymmetric (i.e., hemisphere) particles and their potential in other plasmonic applications. This constitutes another main goal of this dissertation; *investigation of plasmonic properties of Ag-nanohemispheres-on-Ge-nanoposts monolayers*.

As addressed in *Chapter II*, the broken symmetry by hemispherical shape of Ag NP leads to dipolar modes parallel and perpendicular to the base, which are significantly different in terms of energy, excitation dependence on polarization and particle-particle as well as particle-substrate couplings. The parallel mode offers distinct advantages in plasmonic applications (e.g., light coupling in photovoltaics or SM detection) over nanospheres. On the other hand the significantly narrow line width of the perpendicular modes in Ag NHSs is ideal for LSPR applications. Further, perpendicular modes observed in the UV region makes NHSs a good candidate for UV plasmonics.

In *Chapter III*, our SM-SERS technique using Ag-nanohemispheres-on-Ge-nanoposts substrates is demonstrated for two analytes; wild-type green fluorescent protein (wt-GFP) and AB. Further, our rigorous work on validating the SM nature of our SERS spectra is provided. While single molecule spectroscopy opens up a window into the private world of molecules, single molecules themselves can be reporters for the local environment. In this dissertation, such value of single molecule spectroscopy is demonstrated where the differentiating effect of surface crystal orientations in Ag NPs on the adsorption configuration of AB SMs, as distinguished from their distinct SERS spectra, is observed. Hence, this dissertation provides another contribution to the SERS literature by shedding light into one of the sources of heterogeneity in SERS.

1.1. Status of Current Research on Azobenzene

Under UV-visible light, AB exhibits a reversible photo-induced switching between *trans* (*t*-AB) and *cis* form (*c*-AB) (Figure 1.2a). In ground electronic state, *t*-AB is 0.6 eV more stable than *c*-AB. When left in dark, meta-stable *c*-AB thermally transforms back to the *t*-AB with an activation barrier of 1 eV (Figure 1.2b) [34, 35]. As seen in Figure 1.3, the absorption spectrum of both *t*-AB (kept in dark) and *c*-AB (exposed to UV light) exhibit a weak band in the visible region at ~420 nm and a strong band in the UV region at ~310 nm. The absorption band at ~420 nm corresponds to $S_1 \leftarrow S_0$ transition which is related to n−π* transition and is symmetry-forbidden for *t*-AB, while the band at ~310 nm is the $S_2 \leftarrow S_0$ transition which corresponds to the π−π* transition.

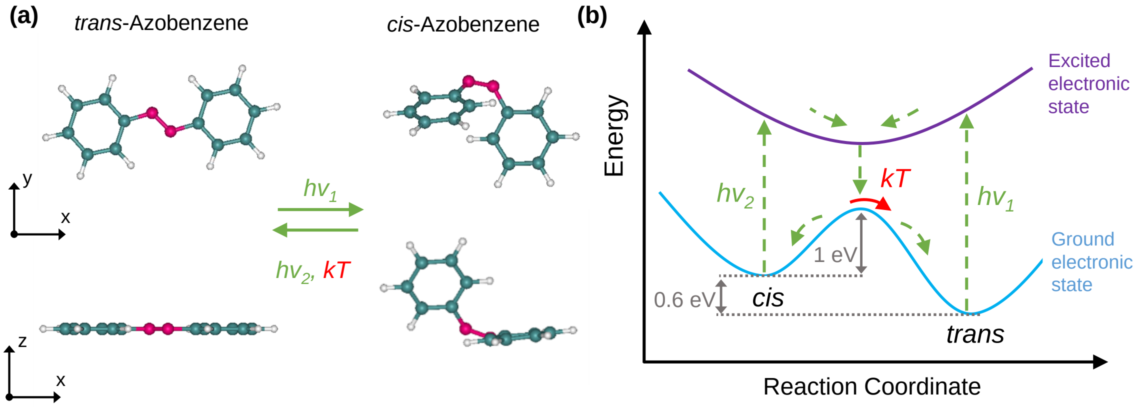

Figure 1.2. (a) Ball-and-stick models showing planar *t*-AB and non-planar *c*-AB in xy (top) and xz (bottom) planes (H: white, C: green, N: magenta). **(b)** Schematic illustrating the reversible photo-induced switching *t*-AB and *c*-AB on the potential energy surface (only the first excited electronic state is shown). Alternatively, conversion from *c*-AB to *t*-AB can be induced thermally.

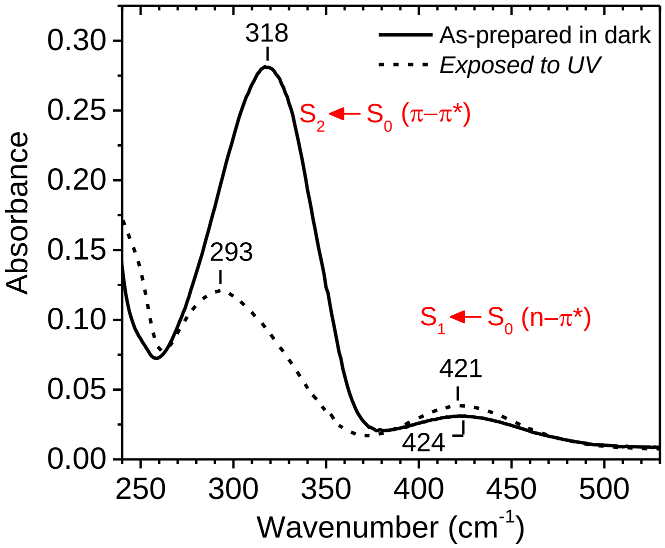

Figure 1.3. Absorption spectrum of 10^{-7} M AB in water: as prepared in dark (solid) and exposed to UV illumination (dashed).

Photo switching quantum yield (φ) of AB is wavelength dependent. For instance, in 80/20 (v/v) solution of H_2O and EtOH, $\varphi_{t\rightarrow c}$= 0.21 and 0.35 at 317 and 413 nm, respectively, and $\varphi_{c\rightarrow t}$= 0.4 and 0.41 at 317 and 413 nm, respectively [36, 37]. Such violation of Kasha's rule is explained by the existence of two different switching pathways on S_1 and S_2 surfaces. Initial studies on AB photochemistry agreed that $S_2 \leftarrow S_0$ excitation leads to switching through rotation, while $S_1 \leftarrow S_0$ excitation results in switching through in-plane inversion (Figure 1.4) [38-40]. Rotational pathway (Figure 1.4) involves cleavage of N═N double bond (azo-bridge) which leads to an increase in its length and decrease in C─N bond length. Inversion, on the other hand, involves rehybridization from sp^2 to sp state due to conversion of one of the N lone-pair dipoles of the azo-bridge to a p-orbital. It is anticipated that during inversion, the N═N bond length is decreased.

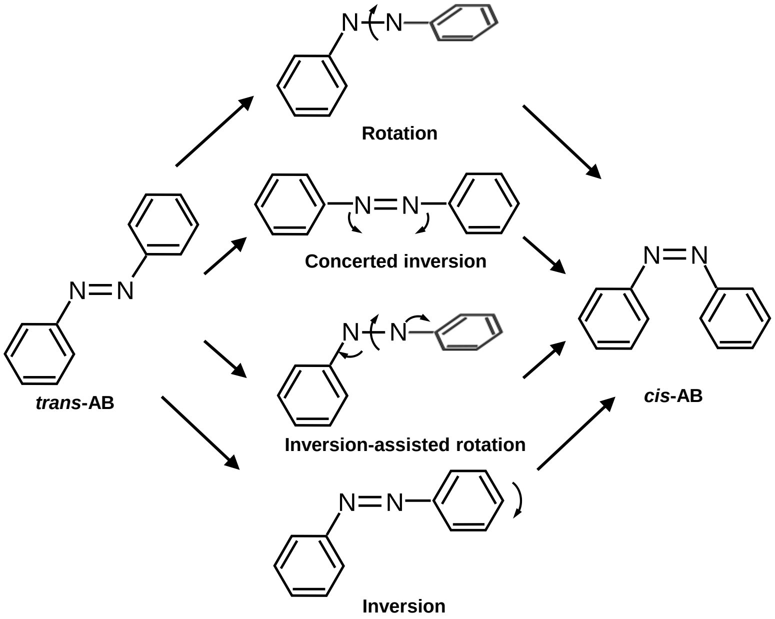

Figure 1.4. Proposed *trans→cis* switching pathways of AB.

Later studies, however, suggested a completely different scenario. Computational and experimental studies showed that following $S_2 \leftarrow S_0$ excitation AB relaxes to S_1 state [41-43]. Further, femtosecond time-resolved Raman spectroscopy studies indicated that the N═N bond retains its double bond character following $S_2 \leftarrow S_0$ excitation and the C─N bond length increases while the N═N and C─C bond lengths decrease following $S_1 \leftarrow S_0$ excitation [41, 43, 44]. These results suggested that regardless of excitation wavelength, switching happens from S_1 state by inversion and rotational pathway starting from S_2 state doesn't exist.

Inversion pathway was also precluded due to a high energy barrier and large $S_0 - S_1$ band gap in the inversion pathway [45]. On the other hand, a conical intersection between S_2 and S_1 potential energy surfaces along the rotation pathway was found in ab initio studies supporting the rotational pathway following $S_1 \leftarrow S_0$ excitation [43-45]. While the existence of inversion and rotation pathways was still under debate, recently two additional pathways, concerted inversion and inversion-assisted rotation, were proposed (Figure 1.4) [46, 47].

Although a consensus on the switching mechanism has yet to be reached, there has been a growing interest on implementing AB in molecular devices which require its immobilization on solid surfaces. While immobilization might be necessary for the localization and ordering of the molecules on surfaces, especially in solid state applications, it may also induce changes in the switching properties of AB due to structural and electronic interactions with the substrate [48]. In the world of molecular devices, it is desired that the active components of a system, i.e., molecular switches, maintain their switching capabilities. Further, a precise control over the switching properties are required which can only be gained by precise control of the adsorption geometries.

Due to their relatively low reactivity, close-packed coinage metal surfaces, in particular the Au (111) surface, have been explored extensively. However, many studies have shown that AB loses its photoswitching capability even on this surface. Certain strategies, such as electronically decoupling the molecule from the metal by introducing an insulating layer to the substrate surface or “spacer legs” to the molecule to prevent the excited-state quenching, were successful in gaining the switching function back. For example, an AB derivative with four tetr-butyl ligands, 3; 3’; 5; 5’-tetra-tert-butyl-azobenzene (TTBA), was successfully isomerized between *trans* and *cis* conformer induced by UV-light and thermal activation [25, 27, 49, 50]. Due to its four tert-butly groups (“spacer legs”), the separation between the TBA molecule and the surface is increased, resulting in reduced electronic interaction of the π system of the molecule with the substrate. A detailed analysis into the photo-induced switching of TTBA using two-photon photoemission (2PPE) spectroscopy revealed that the switching is not driven by direct photon absorption by the molecule. It is rather a result of a charge transfer from Au d-orbitals to the highest-occupied molecular orbital (HOMO) of TTBA [27]. Interestingly, photoswitching of a similar AB derivative with two tetr-butyl ligands (i.e., 4; 4’-di-tert-butyl-azobenzene (DTBA)) could not be induced.

While the photoswitching of AB and its derivatives on coinage metals has proven to be challenging, switching induced by other stimuli, such as inelastic tunneling electrons, and electric field, has also been explored. Switching of TTBA molecule which was successfully isomerized by photo and thermal excitation, was also induced by electric field and inelastic tunneling electron on Au(111) by STM [23, 51]. Intriguingly, inelastic tunneling electron-induced switching of the same molecule (i.e., TTBA) could not be induced on Cu(111) and Au(100) surfaces [27]. Electron-induced switching was also demonstrated for other AB derivatives. For example, reversible electron-induced switching for AB and a derivative of AB, Disperse Orange 3, was demonstrated on Au (111) [52, 53]. The bias voltage used in both studies (1.5 eV and 0.65 eV in [52] and [53], respectively) were significantly lower than the minimum photon energy (~2.88 eV) required for photoswitching. The significantly lower energy required for electron-induced switching was interpreted to a change in the molecular electronic state of AB on Au (111) surface resulting in the reduction of the excited state barrier, or to ground state switching by crossing over the ground state switching barrier or by vibrational excitation.

Another AB derivative, Methyl Orange (MO), was also studied on Au (111) surface by STM [54]. Although the *trans→cis* switching of MO could be induced by inelastic tunneling electrons, the reverse switching was not observed. Further, *cis*-MO was observed 5 times more than *trans*-MO on Au(111) surface, despite the fact that *trans*-MO is energetically more favorable than *cis*-MO by 0.95 eV in gas phase. This indicated that *cis*-MO is energetically favored conformer on Au(111) surface, and thus explains why *cis→trans* switching of MO could not be induced [54]. Tunneling electron-induced switching of another AB derivative, dimeta-cyani-AB (DMC), was achieved on Cu(100), despite the fact Cu(100) is one of the most reactive among the surfaces that have been used to study the switching of AB [27]. Interestingly, switching of the same molecule could not be observed on Au(111) surface [55].

CHAPTER II

SURFACE PLASMON MODES IN SILVER NANOHEMISPHERE MONOLAYERS

2.1. Introduction

Plasmonic devices, such as chemical sensors [56-60], surface enhanced Raman scattering (SERS) substrates [30, 32, 61-63], light coupling layers in photovoltaics [64-68], and plasmonic photocatalysts [69-71] are conveniently prepared by immobilization of metal nanoparticles (NPs) on a substrate. When NPs are synthesized directly on a substrate (e.g., vapor deposition, electrochemical reduction), the metal adatom surface diffusion length may be comparable to or larger than the NP size. As a result, the NP can approach thermodynamic equilibrium and minimize the total surface energy, resulting in the formation of a certain contact angle between the metal–ambient and metal–substrate interfaces. The contact angle can be significantly less than 180°; that is, the metal wets the substrate. Hence, the particles may be truncated spheres (i.e., hemispheres) rather than spheroids [60, 68, 69, 72-74]. As computationally demonstrated, hemispheres show higher diversity of localized surface plasmon modes compared to spheres due to broken symmetry [9, 75]. However, experimental verification of these diverse plasmonic properties have not been done. More than just verification, the experimental characterization of plasmons in hemispherical NPS are needed to explore their potential applications to various plasmonic devices.

In the present work, the plasmon modes in random 2D ensembles of Ag nanohemispheres (NHSs) exhibiting short range order are investigated under s- and p-polarized incident radiation at various angles. While, the present work focuses on the electrochemically reduced NPs on glass substrates, the similar plasmonic characteristics are also found for Ag NPs deposited on glass substrates by physical vapor deposition (PVD). Further, the plasmon modes are studied by in situ extinction acquisitions during NP synthesis and complimented by finite integral time domain (FITD) simulations for the investigation of particle–substrate and particle–particle couplings as well as plasmon damping.

It is revealed that the broken symmetry by asymmetric particle shape leads to dipolar modes parallel and normal to the base, which are significantly different in terms of energy, excitation dependence on polarization, and particle–particle as well as particle–substrate couplings. High field concentrations are induced at the sharp edges (i.e., lightening rod effect) leading to enhanced coupling with the substrate or adjacent NHSs. Unlike in spherical NPs, the dipole moment of the plasmon modes parallel to the base is located close to the substrate. Thus, strong electric fields at the particle–substrate interface is observed for NHS as opposed to spherical NPs of similar size

Further, the high field concentrations at the sharp edges of NHS lead to enhanced particle–particle coupling. Interestingly, unlike in a spherical dimer, where the field intensity peaks in the middle of the gap, the maximum field in a NHS dimer gap occurs on the metal surface (i.e., at the edges), overlaying with the chemical enhancement. Hence, higher sensitivity molecular detection/sensing is anticipated with coupled NHSs.

The electrochemical reduction technique used in the present work includes the reduction of NPs on Ge thin films deposited on glass substrates where Ge functions as the reducing agent [30, 73]. A unique feature of this Galvanic displacement technique is found to be consumption of Ge everywhere, except just below the center of NPs, resulting in mushroom-like structures. NHSs are essentially immobilized on Ge nanoposts of uniform height from the glass substrate. A useful attribute of the mushroom-like structure is separation of the hemisphere edges, where the highest electromagnetic field concentration are observed, from the substrate. This separation allows reduced substrate coupling and damping. Hence, the extinction peaks are narrower and easier to resolve for different modes.

2.2. Methods

2.2.1. Ag Nanoparticle Synthesis on Ge Thin Films

Ag NPs were prepared on Ge thin films by electroless deposition technique in which the Ge thin film acts as a reducer agent, and also immobilizes the nanoparticles [30, 33]. The Ge films of 4.5 nm thickness were deposited on 25 mm × 25 mm glass slides using a Cressington 208C Physical Vapor Deposition (PVD) system at a deposition rate of ≈0.2 nm/s. Prior to deposition, the Eagle XG glass slides (Corning Inc.) on which the Ge thin films were deposited were scrub cleaned using a brush in a solution of 50% isopropanol in DI water. Subsequently, the glass slides were ultrasonicated in the same solution for 10 min at 40 °C. Next, they were rinsed by ultrasonication in DI water for 5 min at 40 °C. The rinsed slides were blow-dried with Ar gas and placed on a hot plate at 150 °C for 10 min to desorb the water on the surface.

Ag nanoparticles were synthesized by immersing the Ge-coated slides in 2 mM $AgNO_3$ solution for 30 s. The reaction was stopped by dipping the substrates into DI water and the substrates were blow-dried with Ar gas.

2.2.2. Ag Nanoparticle Synthesis by Physical Vapor Deposition (PVD)

Ag nanoparticles (NPs) were synthesized on Eagle XG glass slides by PVD. Same substrate cleaning procedure as in Ge deposition (*Section 2.2.1*) was followed. The deposition was performed at a deposition rate of 0.1 nm/s. An effective Ag thickness of 1 nm, which results in Ag NP formation, was deposited as monitored by the thickness crystal monitor of the deposition system.

2.2.3. Characterization of Ag-on-Ge Substrates

Ag NPs reduced on Ge were characterized for size, shape and interparticle separation using an FEI Quanta 600 FEG Field-emission SEM. To avoid electrostatic charging, the Ge films for the SEM study were deposited on transparent and conductive indium tin oxide (ITO) coated glass substrates (R_s= 5-15 Ω), purchased from Delta Technologies, Ltd. The SEM samples exhibited nearly identical optical extinction characteristics with those deposited on uncoated Corning Eagle XG glass slides. Therefore, the NPs synthesized using Ge thin films deposited on ITO substrates were anticipated to have the same distribution of size and interparticle separation as those synthesized using Ge thin films deposited on glass substrates. To determine the size and the shape of the particles, SEM images were captured at a 90º (i.e. top-view) and at a 45º angle with respect to the substrate plane.

AFM characterization of the Ag NPs and the underlying Ge thin film were performed by a Veeco Multimode V Scanning Probe Microscope in the TappingMode® setting. The particle height and basal diameter were analyzed for 965 particles using NanoScope Analysis v1.40r1 software. For the AFM characterization of the Ge film, the Ag NPs were removed by dissolving Ag into a mercury droplet through Ag amalgam formation.

2.2.4. Optical Extinction Spectra of the Ag-on-Ge Substrates

The extinction spectra of the substrates were acquired by a Cary 300 double-beam spectrometer using polarization filters (American Polarizers, APUV-UV linear polarizer) for both the reference and the sample. An uncoated glass substrate was used as the reference. Baseline correction was performed prior to the measurement of the extinction spectra. The incidence angle was varied from 0 to 75° at intervals of 15° by rotation of the sample and reference using a house-made rotating substrate holder.

2.2.5. Kinetics of Ag Nanoparticle Growth Monitored by In-situ Extinction Spectroscopy

The in-situ extinction acquisitions were performed using a StellarNet BLK-CXR-SR CCD spectrometer. The Ge-coated glass substrates were diced to 8 mm × 12 mm pieces and mounted in a quartz optical cell (1 cm optical path length) with a plastic clip. Subsequently, 3 mL of 2 mM $AgNO_3$ was delivered into the optical cell with a pipette and the time-series spectra were collected at 5 s intervals with 1 s signal accumulation per spectrum. The acquisitions were reproduced 3 times with negligible standard deviation. The acquired spectra were also baseline-corrected for the glass substrate, optical cell as well as Ge film. Accordingly, time-series spectra for optical cell + glass substrate + Ge film + Ag NPs + $AgNO_3$ solution were first acquired against air, S1(t), where t denotes time. Time at the onset of increasing extinction was precisely set to zero. Additionally, spectrum for optical cell + glass substrate + water was acquired against air (S2). Next, spectrum for optical cell + glass substrate + Ge film (unconsumed) + water was acquired against air (S3). The extinction of original (unconsumed) Ge film was derived as S4 = S3 – S2. Next, the extinction spectra of Ag NPs were obtained as S5(t) = S1(t) – S2 – K(t)×S4, where K(t) is the subtraction factor for the Ge film. K(t) gradually decreases during the NP reduction because of consumption of Ge. Hence, K(t) measures the fraction of remaining Ge. Accordingly, 1 – K(t) is the fraction of Ag reduced. However, reduction of Ag essentially stops before all Ge is consumed. Hence, to show the extend of Ag reduction, the fraction, (1 – K(t)) / (1– Ks) was adopted where Ks is the fraction of Ge remaining at saturation.

2.2.6. Numerical Simulations

To elucidate the plasmon modes, finite integral time domain (FITD) simulations of Ag NHS arrays were carried out using the commercial software CST MICROWAVE STUDIO®. The numerical model consisted of uniformly spaced NHSs in square lattice positioned on a 4.5 nm thick Ge layer standing on a semi-infinite glass domain. Although a triangular lattice is better representative of the synthesized Ag NHSs, a square unit cell enclosing a NHS in its center allows for computational stability and ease. Unit cell boundary conditions were utilized in x- and y-directions. This configuration ensures that an infinite number of unit cells in both the x- and y-directions were taken into account in the simulation. Open floquet ports were used as input and output ports to calculate transmission/reflection from/through the structure. The ports were placed at distances of Zmin from the base and Zmax from the top of the structure. The excitation plane wave source signal was placed at the port located at Zmax which propagates along the negative z-direction. The frequency domain solver was then employed with tetrahedral meshing in order to extract reflection, transmission coefficients and the electric field distributions.

2.3. Results and Discussion

2.3.1. Characterization of Ag Nanohemispheres and the Underlying Ge Film

Ag NPs reduced on Ge were characterized for size, shape and interparticle separation using SEM. Figure 2.1a shows the plan-view SEM image of Ag NPs reduced on Ge. Imaging of the substrate at an oblique angle of 45º by SEM (Figure 2.1b) reveals that the particles are essentially truncated spheres. As seen in Figure, 2.1a, the Ag NPs are distributed randomly, lacking a long-range order. However, a short-range order of the particles, forming linear and non-linear conjugates such as dimers, trimers, tetramers, and higher order chains are observed.

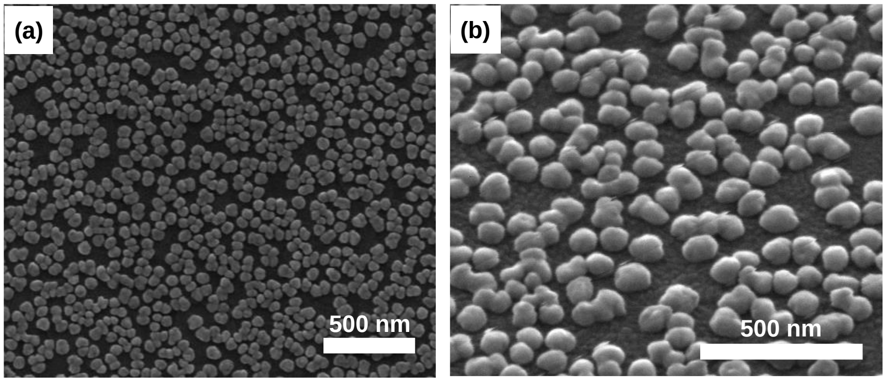

Figure 2.1. Plan **(a)** and oblique (45°) **(b)** SEM images of the Ag NPs reduced on 4.5 nm thick Ge film (30 s immersion time).

The size of the major and minor axes of the particles, which represent the basal diameter (d) and the apparent height (h'), respectively, were computed for 100 particles using ImageJ image analysis software [76] and the distributions are given in Figure 2.2.a. The average d was computed to be 65±13 nm. With the assumption that NPs are hemispheres, it is driven that $h' = r(1+\cos(45°))$, where r is the particle radius, as illustrated in Figure 2.2b. Accordingly, r is computed as 29 ± 5 nm for measured value of $h' = 49 \pm 9$ nm. The computed r is

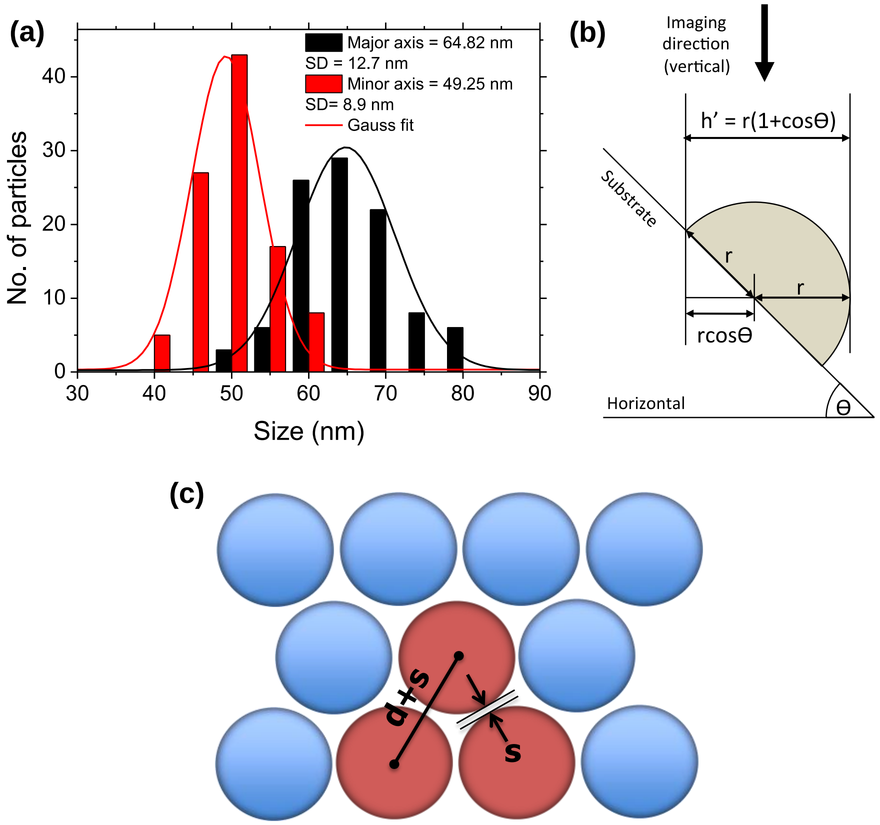

Figure 2.2. Diameter and apparent height distributions of the Ag NHSs obtained from oblique angle (45°) SEM image **(a)**. The relation between apparent height and radius of a Ag NHS imaged by oblique angle SEM **(b)**. Schematic depiction of the equilateral triangular lattice arrangement of Ag NPs **(c)**.

approximately half of the value of the basal diameter, d (65±13 nm). Therefore, the assumption that the particles are of hemispherical geometry is valid.

In order to calculate the interparticle separation, s, the particle arrangement is approximated to be an equilateral triangular lattice with lattice constant of $d + s$ as illustrated in Figure 2.2c. In such an arrangement (i.e., equilateral triangle), there is ½ particle per unit cell. Accordingly, the particle density, N, is given by

$$N = \frac{0.5}{(\sqrt{3}/4)(d+s)^2} \qquad (1)$$

The average density of the particles was calculated as $N = 2.57x10^{-4}$ nm^{-2} from the plan view SEM image (Figure 2.1a). Using Equation 1, the average interparticle separation is found as $s =$ 2 nm.

The basal particle diameter, d, and the interparticle separation, s, were corroborated by AFM analysis of the substrates (Figure 2.3). Distribution of d, which was created by analyzing 965 particles is given in Figure 2.3b where average d was computed as 67±6 nm. However, since the AFM tip is much larger than the interparticle separation (radius of a MikroMasch NSC 18 probe is 8 nm and height is 12-18 μm), this value represents valley-to-valley or peak-to-peak distance in the AFM map (i.e., s+d). Hence, given s is calculated to be 2 nm from the SEM study, d is found as 65 nm which is identical to the SEM result. Further, particle height was determined as 33±2 nm from the base. Here, the base was adopted as the lowest height, and it was measured at locations, where several adjacent NPs lifted off and opened up sufficiently large area for AFM tip to come in contact with the substrate.

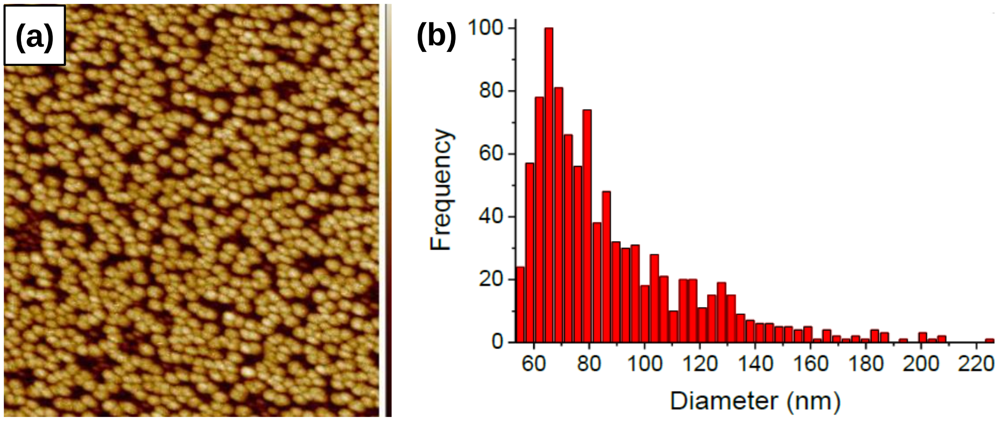

Figure 2.3. Representative AFM height map of Ag NHSs reduced on Ge **(a)**. Corresponding distribution of NP diameters **(b)**.

During the synthesis of Ag NHSs, the Ge film serves as the reducing agent, and hence is expected to diminish because of oxidation and dissolution in water during the Galvanic displacement. In order to characterize the remaining Ge film, the Ag NHSs were dissolved and washed-off in a mercury aliquot through amalgam formation. This process allows the removal of Ag nanoparticles without disturbing the remaining Ge thin film. The AFM image of the substrates after the removal of the particles reveals Ge nanopost of ~4 nm height as seen in Figure 2.4a. This value is identical to the Ge thickness measured by the quartz crystal microbalance of the deposition system (i.e., 4.5 nm). Hence, it is anticipated that during the NP synthesis, Ge film is consumed and dissolved leaving behind nanoposts just below the center of the Ag NPs, forming mushroom-like structures as illustrated in Figure 2.4b.

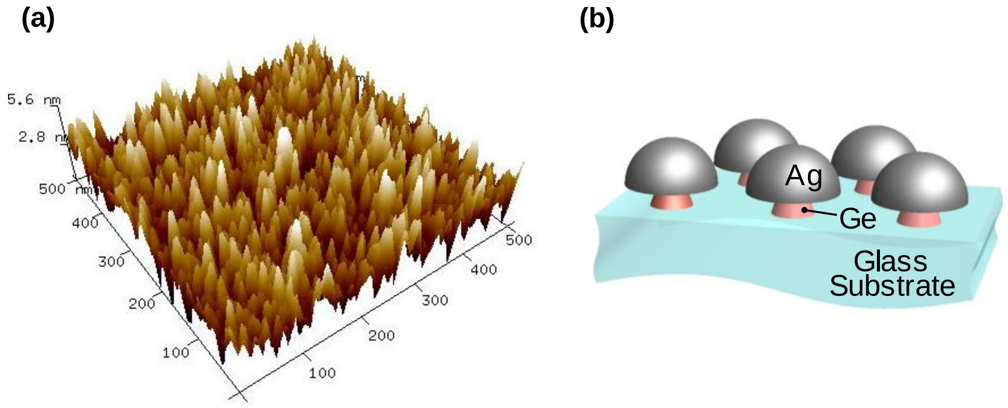

Figure 2.4. AFM image showing the Ge nanoposts after the removal of Ag by amalgam formation **(a)**. Illustration of mushroom-like structures where Ag NHSs are formed on Ge nanoposts **(b)**.

2.3.2. Plasmonic Properties of Ag NHSs-on-Ge Nanoposts Substrates

i) Experimental Characterization of Optical Properties

Figure 2.5a and 2.5b show representative extinction spectra of Ag NPs at various incidence angles (θ) using s- and p-polarized incident radiation (Figure 2.5c), respectively. When the incident radiation is s-polarized (Figure 2.5c), the extinction spectrum exhibits a broad band centered at 482 nm and a weak shoulder band centered at 352 nm. However, when the incident radiation is p-polarized and at an angle relative to the substrate plane (i.e. oblique incidence), additional extinction features appear in the UV region of the spectrum (Figure 2.5b).

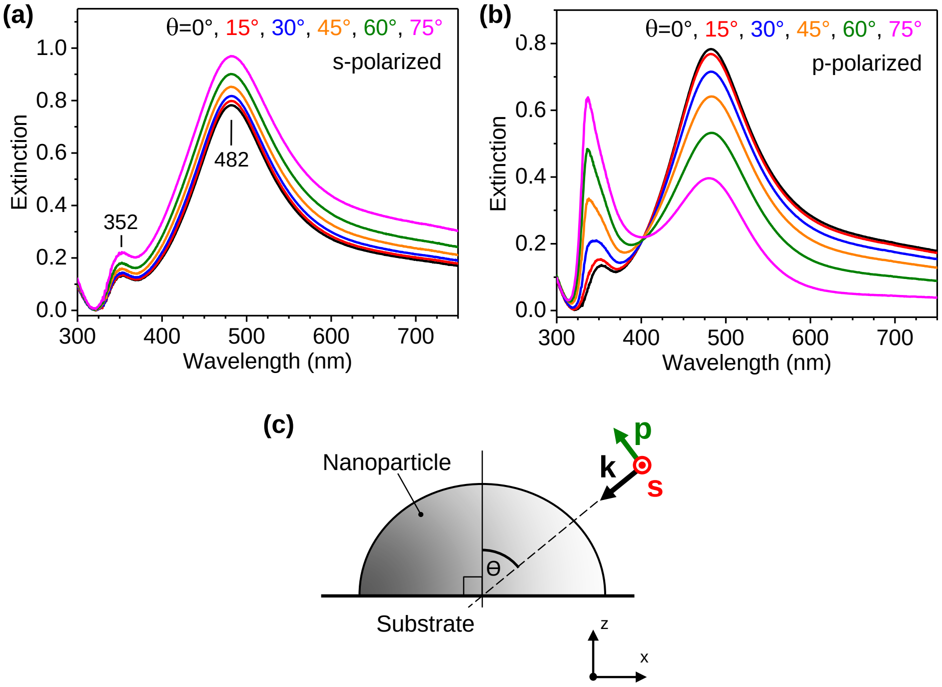

Figure 2.5. Extinction spectra of Ag NHSs reduced on Ge thin films at varying angle of incidence (0-75°) for s- and p-polarization **(a)** and **(b)**, respectively. Definitions of incidence angle and s- and p-polarizations **(c)**.

In order to gain insight into the relationship between the extinction spectrum and the angle of incidence, the extinction spectra in Figure 2.5b were fitted to Gaussian peaks using MagicPlot software as shown in Figures 2.6a-f. At $\theta=0^{o}$, the spectra is resolved into 6 Gaussian at 2.22, 2.58, 3.05, 3.45, 3.55, and 3.64 eV (560, 480, 407, 359, 349, and 341 nm). The position and line width of the resolved peaks essentially has no dependence on the incidence angle as seen in Figures 2.6g and 2.6i. As evident from Figure 2.6h, the modes at 359, 349 and 341 nm (color coded as orange, cyan and green, respectively) are minimally excited in the presence of s-polarized radiation at any θ, and of p-polarized radiation at normal incidence ($\theta=0^{o}$). On the other hand, the modes at 560 and 480 nm (color coded as brown and blue, respectively) are strongly excited under the same conditions. Further, when the incident field is p-polarized, the intensity of the modes at 359, 349 and 341 nm increases while the intensity of the modes at 560 and 480 nm decreases with increasing θ (Figure 2.5h).

An isolated sphere has 3 dipolar plasmon modes corresponding to 3 orthogonal axes (i.e., normal modes). While two of the dipolar modes are parallel (D═) the other is perpendicular (D⊥), to the basal plane, and conveniently to the substrate surface in case of immobilization. These normal modes are degenerate in a single energy due to symmetry. In a hemisphere on the other hand, the broken symmetry lifts the degeneracy of dipolar modes. The energies of D⊥ and D═ are different from each other as well as that of a sphere of equal volume due to shape-modified restoring force constants for the electron gas (equivalently polarizabilities). When the incident field is s-polarized or p-polarized and $\theta=0^{o}$, the dipole moment induced by the field is orthogonal with the dipole moment associated with D⊥. As a result, D⊥ is not excited, while D═ is excited. In contrast, p-polarized radiation at oblique incidence has polarization vector having both parallel and perpendicular components to the substrate. Hence, the induced dipole moment has projections on both D⊥ and D═ dipole moments. Therefore, both parallel and perpendicular modes are excited.

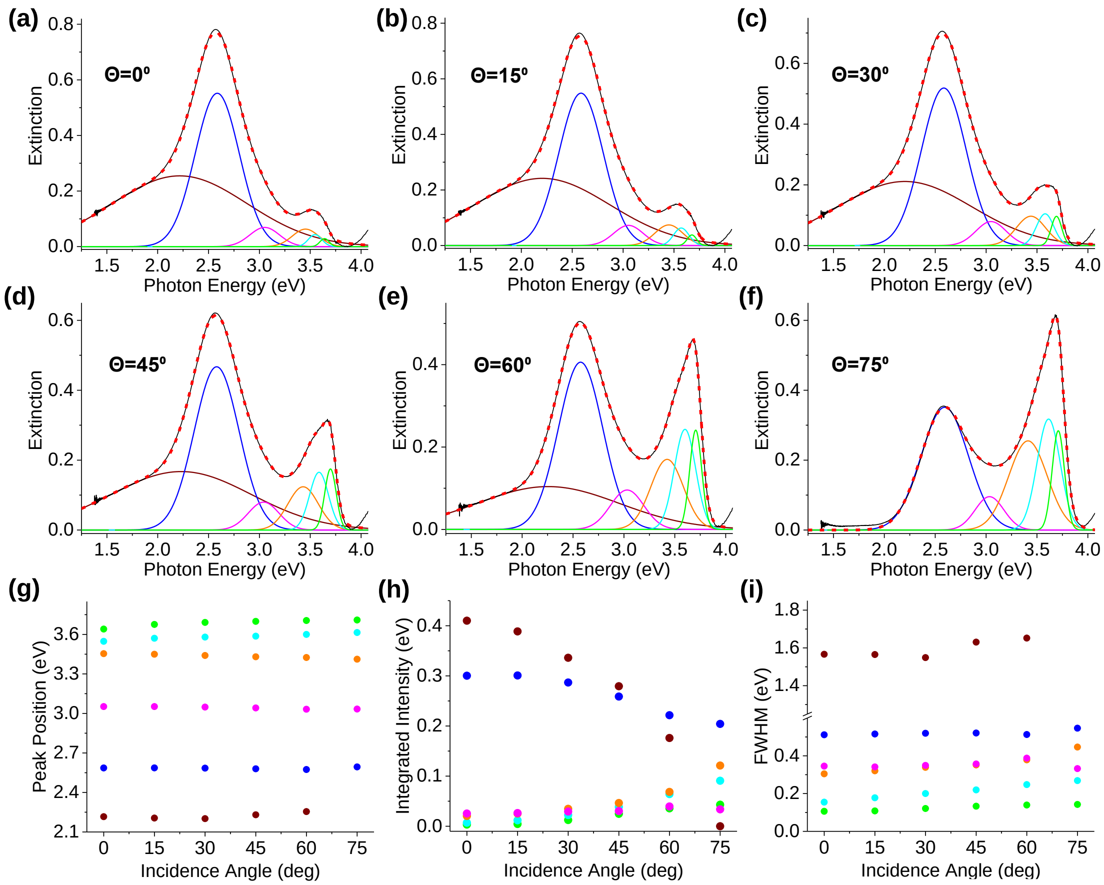

Figure 2.6. Deconvoluted peaks of the extinction spectra for p-polarized incidence at 0-75º, coded with different colors **(a-f)**. Incident angle dependence of peak position, integrated intensity, and width (FWHM) **(g-i)**, color coding is same as in **(a-f)**.

Further, in Ag NPs with large sizes (i.e., d=65 nm), multipolar (MP) modes (e.g., quadrupole, hexapole, or octupole) can be excited due to phase retardation of the incident field inside the material as a consequence of nonhomogeneous polarization of the light [77-80]. When light is p-polarized and θ≠0º, the phase of the incident field varies on the substrate surface with a repeating distance of λ'=λ/sinθ. With increasing θ, λ' becomes shorter and the vertical field patterns better match the multipoles of this mode (MP) leading to a stronger excitation. However, a similar match does not occur with s-polarized excitation. Thus, the dependence of excitation of a MP mode on incidence polarization and θ is similar to that of D⊥, but driven by a different mechanism. Accordingly, the modes at 359, 349 and 341 inferred to be associated with D⊥ or MP, while the modes at 560 and 480 nm are inferred to be associated with D═.

While no change in the extinction profile of the substrates is observed when the light is s-polarized, the extinction intensity increases with the increasing θ as observed in Figure 2.5a. This is attributed to the increased length of the light path passing through the substrate with increasing θ. Indeed, this effect is believed to counter balance the anticipated decrease in the intensity of the mode at 407 nm, which is inferred to be associated with D═, with increasing θ (Figure 2.6h).

ii) Optical Properties Studied by Numerical Simulations

The computed extinction spectra for a monolayer of Ag NHSs were shown in Figures 2.7a and 2.7b for s- and p-polarized incident radiation, respectively. The numerical model consists of uniformly spaced NHSs in square lattice positioned on a 4.5 nm thick Ge layer standing on a semi-infinite glass domain. As inferred from Figure 2.4a, a large fraction of the Ge film is consumed as reducing agent during Ag NHS synthesis (i.e., Galvanic displacement). Accordingly, the Ge layer was modeled as a porous medium and its dielectric function was computed using dielectric mixing (i.e., Ge in vacuum by zero-order effective medium approximation) [81]. As-deposited Ge films were characterized as amorphous by Raman spectroscopy. Therefore, the dielectric function of Ge is adopted as that for amorphous Ge [82].

If a square cell is set with the experimentally measured average separation of 2 nm along the unit cell edge, then separation along the diagonal direction is 27 nm. Hence, adopting the polarization along the unit cell edge maximizes and exaggerates the particle−particle coupling along the unit cell edge. This situation does not ideally represent the effective coupling in the experimental case, which is orientation-averaged (isotropic) due to disorder. As shown in Figure 2.7., separation of 8 nm (along the cell edge) and Ge filling factor (FF) of 0.05 yield an optimum match with experiment in terms of the parallel (to NHS base) dipolar mode wavelength.

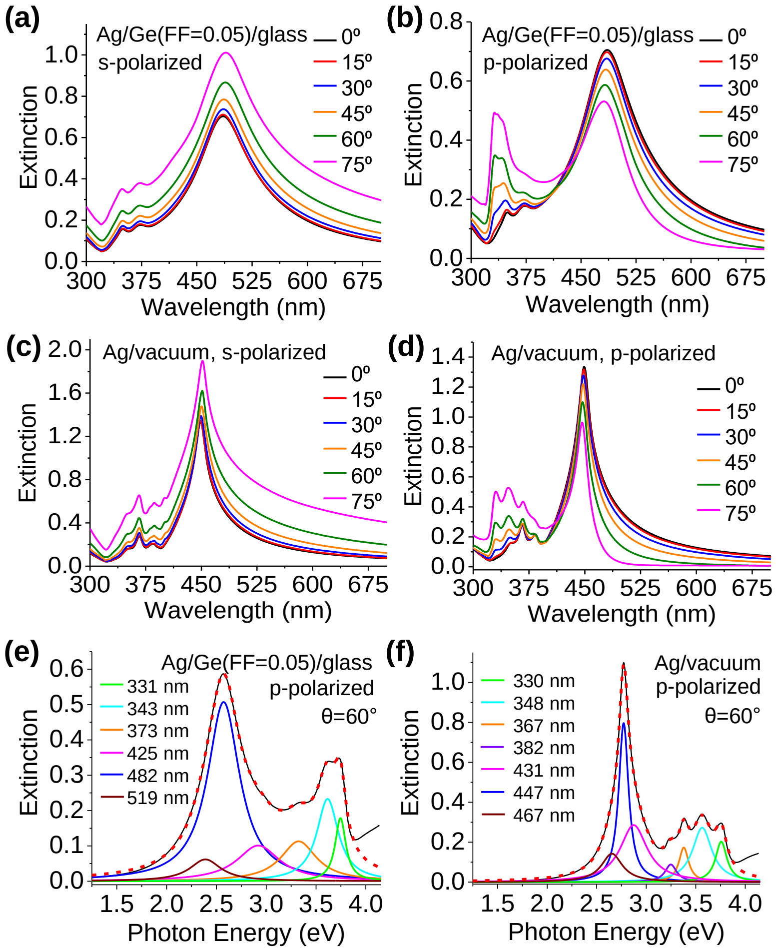

Figure 2.7. Simulated extinction spectra of Ag NHSs. The incidence angle, polarization state and substrate information (Ge filling factor (FF) or vacuum) are given in each plot. Deconvoluted peaks in (e) and (f) are Lorentzian, and their resonance wavelengths are given in the figure legends. Interparticle spacing, s, is 8 nm.

Here, an exact match between experiment and simulation is not expected, especially for strongly coupled modes (particle−particle coupling), as the experimental case of an ensemble involves short-range order against the ideal periodicity of the simulated arrays. The objective of the numerical study in the present work is to identify the weakly coupled modes and major strongly coupled modes as well as to compare the plasmon excitation trends (i.e., with incident angle/polarization, substrate/particle coupling) to gain insights. Nevertheless, a reasonable agreement is found between the measured (Figures. 2.5a-b) and simulated spectra (Figures. 2.7ab, respectively) in terms of resonant wavelengths as well as dependence on incident polarization and θ.

Compared to the experimental case, the simulated resonances exhibit narrower widths. This is due to lack of heterogeneity in particle size, shape and separation (both distance and direction with respect to excitation field). In addition, the damping due to electron surface scattering is absent in the simulated case since it is not taken into account in the dielectric function of bulk Ag employed in the simulations. In particular, the 'no substrate' case (Figures 2.7c-d) exhibits the sharpest resonances due to absence of electromagnetic coupling with the substrate. Figures 2.7e and 2.7f show the deconvoluted extinction peaks in the presence and absence of substrate, respectively, for p-polarized incident radiation at θ = 60°, where both parallel and vertical modes are excited.

iii) Plasmon Mode Assignments

With the help of simulated electric field vector maps shown in Figures 2.8a-d, the modes were identified and denoted from longer to shorter wavelength (i.e., 482, 373, 343 and 331 nm) as 'dipolar parallel to the base', D═, 'dipolar perpendicular to the base', $D\perp_1$, multipolar, MP, and 'dipolar perpendicular to the base', $D\perp_2$, respectively. Computations for the no-substrate case essentially produce the same modes (i.e., same field distributions) at 447, 367, 348 and 330 nm, respectively (Figures 2.8e-h). In Figure 2.8, the slight asymmetry in field distributions along the x-axis is attributed to oblique incidence (i.e., θ = 75°).

For a single Ag NHS (radius of 20 nm in vacuum), Attanayake et al. reported 3 different resonances for D═ excited in the case of parallel incident polarization (401, 380, and 365 nm) [75]. We reproduced the computational results of Attanayake et al. for single NHSs of the same geometry. However, the two shorter wavelength modes are weakly excited and their configurations are not clearly identified from the field profiles, which are overshadowed by that of the 401 nm mode. In the experimental case, this major parallel mode is observed as a broad resonance band centered at 482 nm. It is redshifted due to particle as well as substrate coupling, and heterogeneously broadened due to distribution in particle shape, size and particle−particle coupling.

Attanayake et al. also observed two resonances at 345 and 375 nm and assigned them to “split perpendicular dipolar modes”. However, the simulated field amplitude map for a NHS dimer at 373 nm excitation ($D\perp_1$) in Figure 2.9 shows that the charges are concentrated at the base of the NHSs and they are connected in the form of a ring. Further, the opposite charge for this mode is concentrated at the apex. Thus, while the mode at 375 nm, $D\perp_1$, is dipolar perpendicular as inferred by Attanayake et al., it is not a “split” mode.

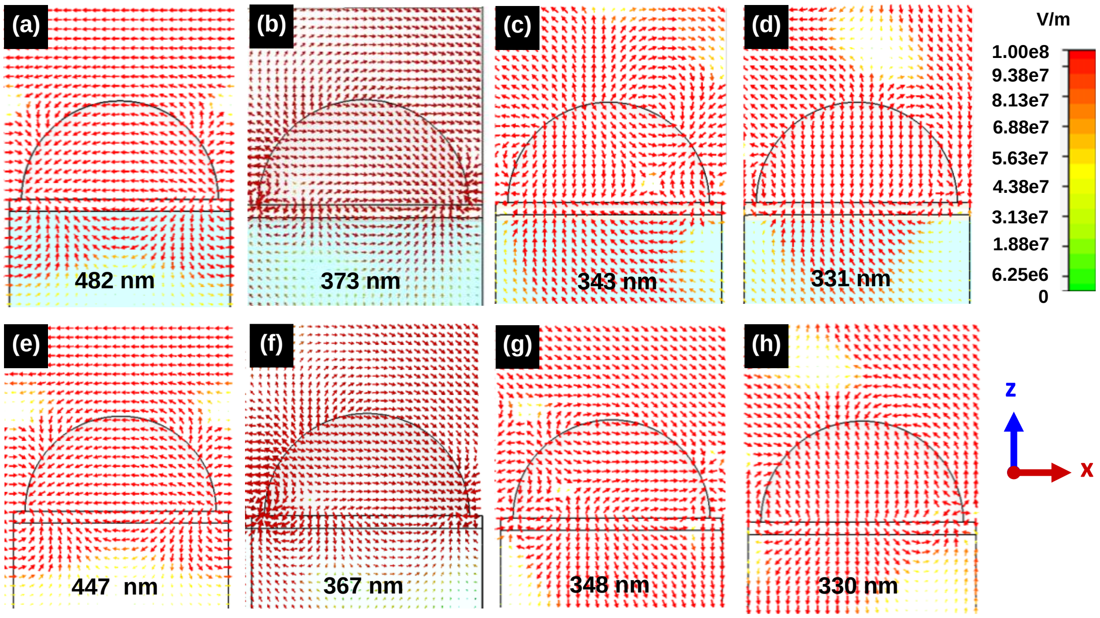

Figure 2.8. Electric field vector maps (x-z cross section) characterizing four different plasmon modes in Ag NHSs on Ge (filling factor = 0.05) on glass **(a-d)** and no substrate **(e-h)**, $D=$, $D\perp_1$, MP and $D\perp_2$, respectively from left to right. The incident radiation is p-polarized and θ=75°, except in (a) where θ=0°. Interparticle spacing for all cases is 8 nm.

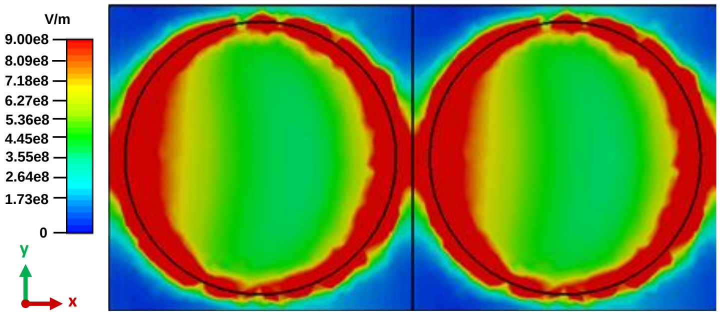

Figure 2.9. Simulated field amplitude map for Ag NHS arrays on Ge on glass (FF = 0.05) showing the xy-plane intersecting the base of two NHSs during resonant excitation of D⊥$_1$ at 373 nm. The incident radiation is p-polarized with θ=75º. The interparticle distance, s, is 8 nm. A ring-like distribution of the pole charge at the hemisphere base is inferred.

Similarly, the 343 nm mode also complex and its assignments based on field amplitude maps of an axial cross section, as done in [75], is not sufficient. To describe this mode, phase-series field vector maps of the xz axial cross section (essentially identical to that of the yz axial cross section) and the xy basal plane were given in Figure 2.10. These field distributions are derived from the simulation of a single NHS of 40 nm diameter in vacuum (matching [75]), for incidence angle of 90°, and at peak excitation of the mode (i.e., 350 nm). The simulations were performed using open boundaries with the source being a plane wave of 1 V/m magnitude. In Figure 2.10, oscillating poles are seen at the edge perimeter (in the form of a ring), center base, and top. The charge distribution appears dipolar at 30° phase, while it is far from a dipolar at 120° phase, where the charge at the base splits into opposite polarities at the edge periphery (ring) and center. Therefore, at best, this mode can be expressed as an expansion of multipoles oscillating with phase differences, hence the notation MP. Nevertheless, MP has a strong perpendicular dipole moment based on its increasing excitation with increasing θ. On the other hand, the complexity of field patterns in Figure 2.10 is not due to interference from D⊥$_1$ and D⊥$_2$. On the basis of the deconvoluted D⊥$_1$ and D⊥$_2$ peaks in Figure 2.7f, excitation of these modes is insignificant at the wavelength, for which MP reaches full resonance.

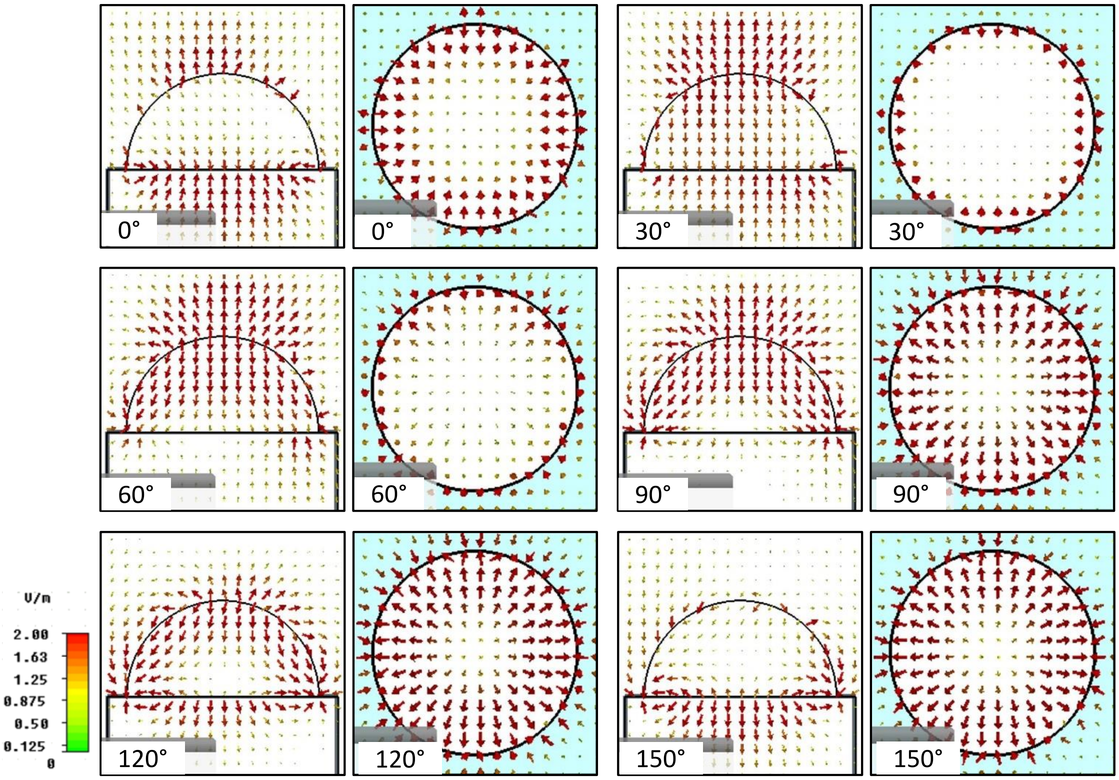

Figure 2.10. Description of the MP mode with phase-series electric field vector maps of XZ axial cross section (left) and XY base plane (right). The phase-series maps are shown in intervals of 30° from 0° to 150° which are antisymmetric with those from 180° to 330°, respectively.

iv.) Substrate Coupling of the Plasmon Modes

As aforementioned, the resonance energy of $D\perp_1$, MP, $D\perp_2$ are essentially same for the simulations of Ag NHSs on Ge (FF=0.05) and in vacuum (i.e., no-substrate) (373, 343, and 331 vs 367, 348, and 331). In addition, these wavelengths also agree with those for isolated NHSs in vacuum [75]. This confirms that $D\perp_1$, MP, $D\perp_2$ exhibit weak substrate as well as particle−particle coupling. On the other hand, a redshift from 447 to 482 nm is observed for D═ in the presence of substrate (i.e. Ge (FF=0.05)/glass). Thus, it is inferred that D═ is strongly coupled to the substrate. The substrate coupling of D═ can also be observe in Figure 2.11, where the Ge FF is varied between 0.01 and 0.51. Here, it can be observed that substrate coupling not

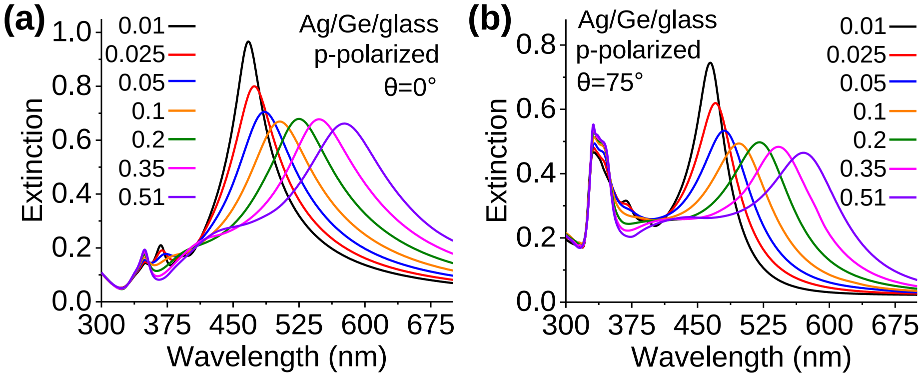

Figure 2.11. Simulated extinction spectra of Ag NHSs on Ge/glass at varying filling factor (FF) at p-polarized incidence of 0^{o} **(a)** and 75^{o} angle **(b)**. The interparticle seperation is 8 nm.

only leads to shifts in the resonance frequency, but also broadens the linewidths due to energy transfer/dissipation.

An interesting plasmonic characteristic distinguishing NHSs from nanospheres is the stronger coupling of D═ with the substrate. As such, D═ systematically shifts from 467 to 577 nm as Ge FF is increased from 0.01 to 0.50 (Figure 2.11a). For comparison, nanospheres of the same diameter, separation and substrate as the NHSs were simulated. In contrast, D═ in nanospheres shifts only from 369 to 372 nm as Ge FF is increased from 0.01 to 0.50 (spectra not shown here). The stronger substrate coupling of D═ in NHSs may be explained by the dipole moment being located close to the basal plane and thus to the substrate. As illustrated in Figure 2.12, the electric field lines from (+) to (−) pole have significant intersection with the substrate resulting in a larger interaction. On the other hand, in a nanosphere the dipole moment passes through the sphere center and is located above the substrate by a distance of its radius.

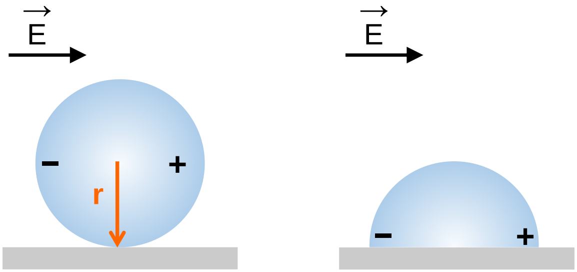

Figure 2.12. Illustration of substrate coupling of a dipole for a sphere (left), and hemisphere (right). Induced fields on the substrate are not shown.

The strong substrate coupling of D= may benefit thin film photovoltaics by efficient light coupling. As reported by Gao et al., 2D Ag NHSs array on crystalline silicon (c-Si) ultrathin solar cell films couple the incident light to fundamental waveguide modes and excite the localized surface plasmon modes (LSPR) in Si [83]. Further, they show a 22 % enhancement in short-circuit current density relative to that for a bare 100 nm thick c-Si ultrathin film solar cell.

Further, for D= in NHSs, the oscillating polar charges squeeze in the sharp edges forming more concentrated fields than those for a sphere. Figures 2.13a-c illustrate the penetration of these strong fields into the substrate at the edges for 3 different interparticle distances. Nevertheless, in the experimental case of mushroom nanostructures, these hot zones miss the Ge stems (posts) and penetrate into low dielectric-constant glass only. Additional evidence for strong substrate coupling for the D= mode is obtained from peak broadening (i.e., increased damping). While the FWHM is computed as 0.12 eV in vacuum, it dramatically increases to 0.41 and 0.47 eV on Ge (on glass) for FF of 0.05 and 0.5, respectively. The increased damping is due to both optical absorption and Ohmic losses associated with charge oscillations in the Ge film by strong plasmon coupling.

A significant application of these high field concentrations induced at the sharp edges might be in the field of hot electron-induced photocatalysis. It is shown that plasmon generated hot electron can be transferred to the molecular orbital of a nearby molecule, resulting in various photo-driven chemical reactions such as oxidation [84, 85], water splitting [86, 87], catalysis [88], and H_2 generation [89, 90]. It is reported by Sil et al. that Au NHSs deposited on glass exhibit enhanced hot electron-induced photocatalytic activity where H_2 dissociation leads to formation of metastable gold hydride (AuH_x) complexes [69]. As discussed by Sil et al., and also shown in the present study, unlike in spherical nanoparticles, the dipole moment of the plasmon modes parallel to the base is located close to the substrate. Thus, strong electric fields at the particle−substrate interface is observed for NHS as opposed to spherical nanoparticles of similar size [91, 92].

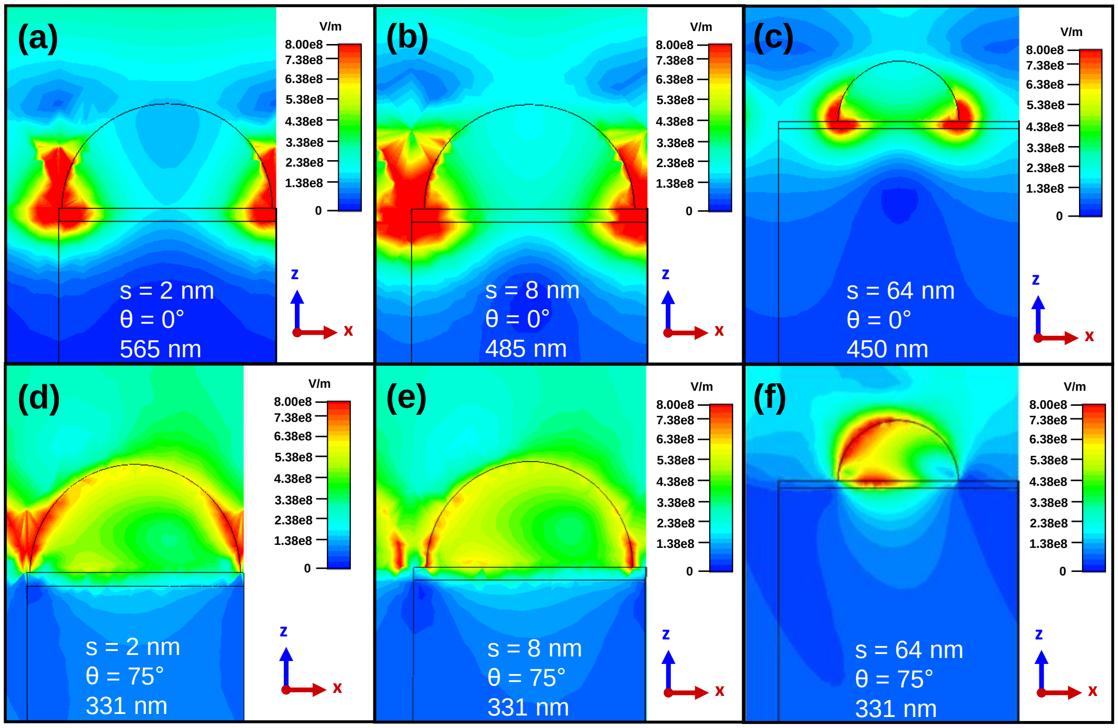

Figure 2.13. Simulated field amplitude maps at the resonant excitation of D═ **(a-c)** and D$\perp_2$ **(d-f)** for Ag NHS arrays on Ge on glass (FF = 0.05) at various interparticle spacing (s). The maps are showing the xz-planes, cross-sectioning Ag NHSs at the center. The incident radiation is p-polarized. The interparticle distance (s), incidence angle (θ), and excitation wavelength are provided in each figure.

v.) Particle−Particle Coupling of the Plasmon Modes

The impact of particle−particle coupling was studied by conducting numerical simulations varying the interparticle separation, s, systematically. Figures. 2.14a and 2.14b compare the extinction spectra for s = 2, 4, 8, 16 and 64 nm for p-polarized incident radiation at incidence angles of 0° and 75°, respectively. Corresponding field maps for different interparticle separations are given in Figures 2.13a-f.

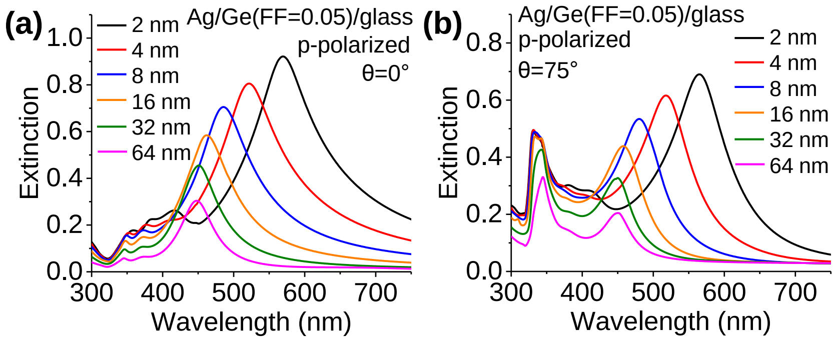

Figure 2.14. Simulated extinction spectra of Ag NHSs on Ge (FF=0.05)/glass at varying interparticle separation (s) at p-polarized incidence of 0^o **(a)** and 75^o angle **(b)**.

Coupled plasmon modes for adjacent NHSs may be examined in the context of plasmon hybridization model as shown in Figure 2.15 [93, 94]. Considering a NHS dimer, hybridization of D═ occurs in 4 normal modes (Figure 2.15a). These modes have oscillating dipoles being either parallel, DJ═ (J-conjugation), or perpendicular, DH═ (H-conjugation), to the interparticle axis. Further, each case has symmetric (in-phase) and antisymmetric (out-of-phase) combinations. In the absence of phase retardation, the antisymmetric modes are not excited by incident radiation because of zero total dipole moment. Compared with D═ in a single NHS, DJ═ is associated with a lower force constant (restoring force) per conduction electron mass due to dipole e−dipole attraction and therefore the resonance shifts towards lower frequencies with decreasing NP separation (i.e., increasing attraction) [94]. An opposite trend occurs for DH═

because of dipole−dipole repulsion. For our simulations, we observe D═ shifting from 450 to 565 nm as s decreases from 64 to 2 nm in Figure 2.14a, indicative of DJ═ characteristics being dominant. The experimental data best match with the simulated case of s = 8 nm, where significant field coupling between NHSs is observed from Figure 2.13b. Whereas, Figure 2.13c indicates essentially no overlap of near fields between NHSs at s = 64 nm for D═ resonance (450 nm).

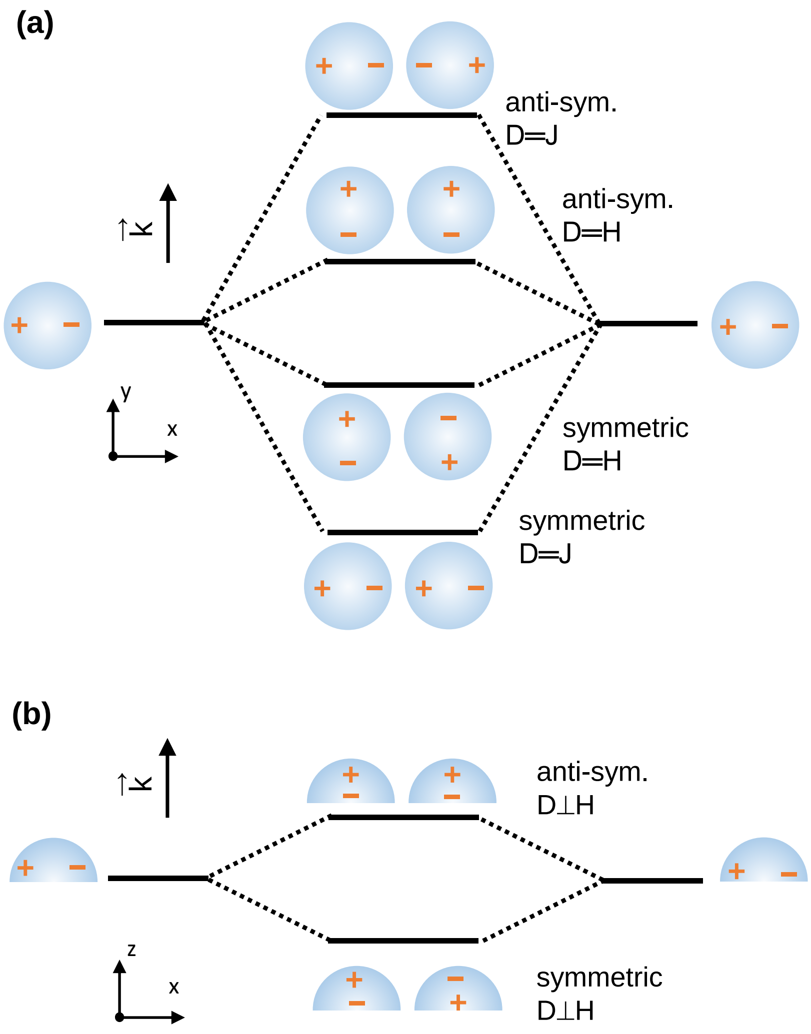

Figure 2.15. Model showing the hybridization of D═ **(a)** and D⊥ **(b)** modes in interacting hemispherical nanoparticles.

Unlike D═, $D\perp_1$ and $D\perp_2$ do not exhibit any notable coupling between NHSs. Since the dipole moment for D⊥ is perpendicular to the dimer axis, hybridization involves H-conjugation (Figure 2.15b). Accordingly, DH⊥ modes are expected to shift to higher frequencies with decreasing interparticle distance as discussed above. Figure 2.14b confirms such spectral shift, but it is negligible. Additionally, the distribution of interparticle distances does not lead to any heterogeneous broadening in D⊥ modes owing to absence of particle−particle coupling. The wavelengths of the D⊥ modes essentially remain constant and equal to those of a single Ag NHS as computed in.[75]. .[75] also reports insignificant shift of DH⊥ with particle separation in dimers. This insignificant level of coupling/hybridization for D⊥ in NHS ensembles positioned on a plane is attributed to weak interaction of dipole moments, which are effectively positioned along the NHS symmetry axes and therefore separated by relatively larger distances. More precisely, for D⊥ , the pole at the base of the NHS involves charge distribution either being uniform over the basal area or ring-shaped around the NHS edge. Therefore, the fraction of base pole charge, which is adjacent to the gap between the particles, is much lower compared to that in DJ═. Hence, coupling across the NHS gaps is weaker for both D⊥ modes.

In reality, the coupling of D═ does not really occur in the form of just J- or just H-conjugates. If an array of 4 particles is considered, each positioned at one corner of a square (i.e., the simplest array), the mode with the highest symmetry involves all 4 dipoles oscillating in phase along one of the square edges. Clearly, each dipole oscillation interacts with others as both J- and H-conjugates simultaneously in the same mode. More complex modes involve combinations of symmetric and antisymmetric oscillations as well as oscillations along the lattice diagonals. With increased number of dipoles in the array, the number/complexity of the modes increases. The majority of these modes are not excited, or are only weakly excited by incident radiation, as the mode patterns do not fit the excitation field patterns. Nevertheless, when the D═ band is analyzed, combinations of multiple peaks are seen in Figures 2.6 and 2.7e for both experiment and simulation, respectively. Hence, excitation of different D═ modes is inferred. The highest intensity peak in Figure 2.7e is attributed to D═ with coherent coupled dipole oscillations everywhere in the array. This mode is strongly excited by normal incidence, where the excitation field is of uniform phase over the array. On the other hand, for oblique incidence, the phase of the excitation field changes over the array and is expected to excite modes with symmetric and antisymmetric combinations. As such, we observe new peaks for oblique angle incidence. Unfortunately, the deconvoluted peaks cannot be assigned to specific modes, because the field patterns obtain from the simulations are associated with overlapping resonances of different parallel modes. In addition, the complex coupled modes determined from the simulations may be symmetry-forbidden in the experimental ensembles because of disorder. The lack of long-range order in Ag NHS ensembles in the experimental case is expected to limit the modes to shorter range, too. Additionally, the objective of the array simulations in the present work is to gain basic insights to explain our experimental results.

vi.) Line Widths and Damping

From Figure 2.6i, the line widths, full width at half maximum (FWHM), of D═ modes at 480 and 407 nm and $D\perp_2$ are 0.40, 0.51, and 0.14 eV, respectively. The significantly lower line width of $D\perp_2$ is attributed to lack of plasmon damping due to energy lost to the substrate (i.e., substrate coupling). Indeed, simulation in vacuum (Figures 2.7c-d) removes the impact of substrate coupling and size/distance distribution, where the line width for $D\perp_2$ is found to be 0.14 eV verifying the lack of substrate coupling of $D\perp_2$. Additionally, as discussed earlier, distribution of interparticle distances (s) does not lead to any heterogeneous broadening in $D\perp_2$ due to absence of particle−particle coupling. On the other hand, when substrate is included in the simulations, the line width of major D═ mode increases from 0.12 eV to 0.41 eV. Hence, the simulations underscore the role of substrate coupling in increased damping, where D═ is dramatically impacted but $D\perp_2$ is not susceptible at all.

Interestingly, the experimental line width, 0.14 eV, is narrower than the numerically computed line width for a single NHS in vacuum by Attanayake et al., 0.19 eV[75]. In the analytical solution, the damping due to electron surface scattering (interface damping) is not taken into account in the imaginary part of the dielectric function governing the nonraditative damping in the bulk dielectric function of Palik [95] which is used in [75]. Thus, the line width in the experimental case is expected to be broader due to interface damping. Therefore, it is inferred that the anomalously lower damping of $D\perp_2$ is due to a photonic effect in the form of reduced radiative damping or subradiance. In fact, Zhou and Odom, in their investigation of cylindrical Ag NP arrays deposited on glass substrates, discuss suppression of radiative damping for the out-of-plane plasmon mode, which is similar to $D\perp_2$ [96]. According to Zhou and Odom, because the *k*-vector of the radiation emitted by D⊥ is on the substrate plane, the emitted energy can be collected by neighboring particles as plasmons and trap the radiation in the array plane instead of losing it to the far field. Thereby, the radiative damping is suppressed accounting for a narrower line width.

2.3.3. Electromagnetic Field Enhancements in Coupled Nanohemispheres

It has been well established that field concentrations occurring due to the excitation of localized surface plasmons (LSP) in metal NPs can approach two-orders of magnitude in narrow gaps. This electromagnetic enhancement is the main contributor of SERS enhancement factor (EF), which can approach ~10^8 allowing for detection of SERS from single molecules [30, 32, 97, 98]. Figure 2.16 shows the simulated field amplitude maps and the corresponding field EF profiles of two NHSs during resonant excitation of D═ for interparticle separation of 8 nm and 2 nm. As demonstrated by Figure 2.16b, the maximum electromagnetic field EF between two NHSs is calculated to be ~6×10^3 for a nanoparticle separation of 2 nm, which is the experimental interparticle separation. The local field intensity (I_{loc}) is proportional to the square of the incident field (E_{inc}):

$$I_{loc} \propto E_{inc}^2 \propto E^2 \tag{2}$$

In SERS, not only the incident field, but also the scattered field (E_{sc}) is enhanced, and its intensity (I_{sc}) is also proportional to the square of E_{inc}:

$$I_{sc} \propto E_{sc}^2 \propto E^2 \tag{3}$$

Hence, the total intensity of enhanced field, I_{SERS}, can be written as the product of both the scattered and local field:

$$I_{SERS} \propto I_{loc} I_{sc} \propto E^4 \tag{4}$$

Accordingly, for field EF of ~6×10^3, the calculated electromagnetic SERS EF for NHS dimers is on the order of 10^{15}.

Unlike, in the case of nanosphere dimers where the field intensity peaks in the middle of the gap [99], the maximum field intensity for 8 nm particle separation occurs on the metal surface (Figure 2.16a), overlaying with the chemical enhancement. However, for smaller interparticle separations (i.e., 2 nm), the regions with maximum field between two NHSs shifts towards the middle of the gap. Nevertless, the field EF on the metal surface is still significant (~3×10^3). In SERS, while electromagnetic enhancement is the main contributor, chemical enhancement (on the order of 10^2-10^3) is also thought to have a contribution to the overall SERS enhancement [100-103]. Chemical enhancement occurs due to the increased polarizability, and therefore the Raman cross-section, of the adsorbate in the presence of the metal surface. The

Raman efficiency may also increase due to broadened or shifted adsorbate electronic states, or formation of new electronic states as a result of charge transfer between molecule and metal [103-105]. Accordingly, adsorption of the molecules to the metal surface is a prerequisite for chemical enhancement mechanism. Hence, compared to nanospheres, higher sensitivity molecular detection/sensing is anticipated with coupled NHSs due to overlapping of the chemical enhancement with the highest electromagnetic enhancement.

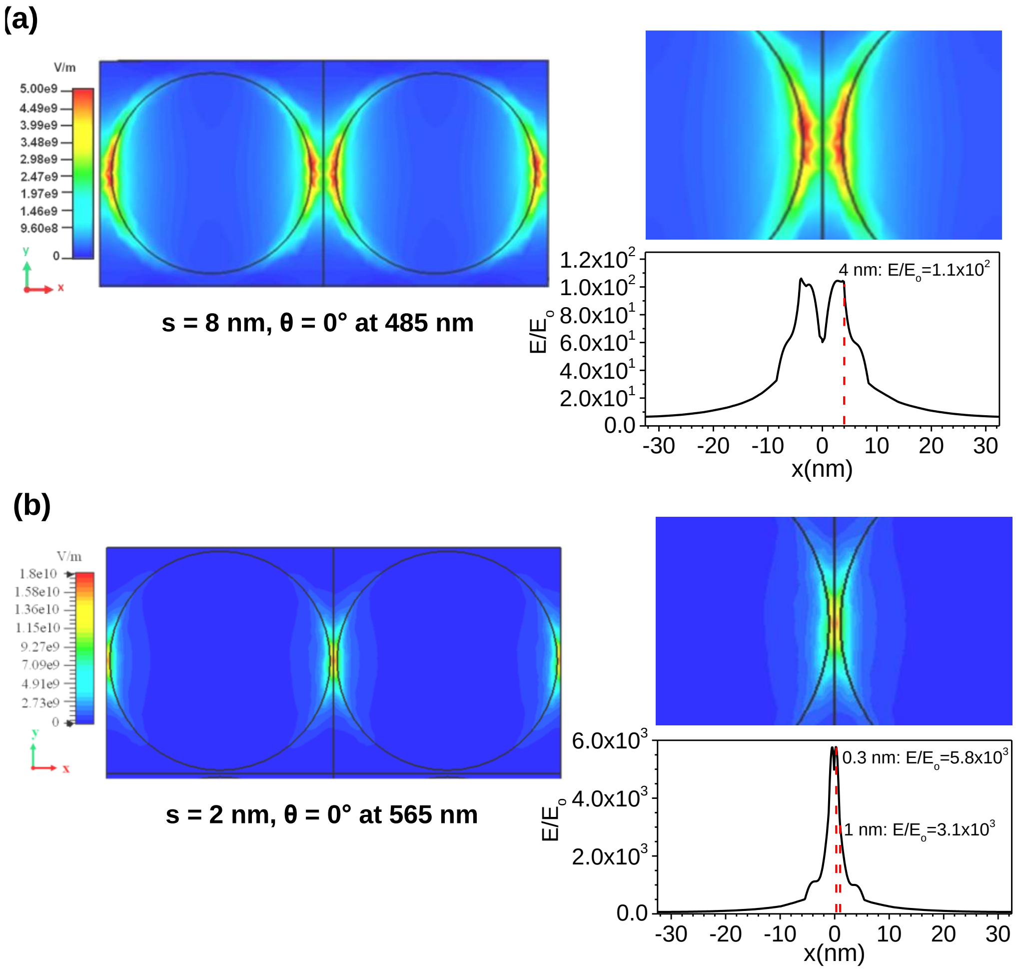

Figure 2.16. Simulated field amplitude maps of two NHSs during resonant excitation of D═ at θ=0° for interparticle separation of 8 nm **(a)** and 2 nm **(b)** in xy-planes intersecting the bases of the NHSs. Corresponding field enhancement factor profiles along the dimer as well as dipole axis (x-axis) are given. The maximum field enhancements and the field enhancements at the metal surface are given on the field enhancement factor profile plots.

2.3.4. Kinetics of NHS Growth Monitored by In-situ Extinction

To elucidate the experimentally observed parallel modes, the time-series extinction spectra of the NHSs with parallel polarization (i.e., normal incidence) were acquired while they were being synthesized in an optical cell (Figure 2.17). This allowed for continuous monitoring of the modes while the dipole−dipole coupling increases progressively with reduction time because of growing NHSs, i.e., increasing NHS density and decreasing interparticle distances. The acquired spectra was fitted to Gaussians using MagicPlot, and the spectral trends of the deconvoluted peaks were analyzed to characterize the plasmon modes, and identify the associated nanostructures (Figure 2.17). During the synthesis of Ag NPs, the progressive oxidation/dissolution of the Ge film (reducing agent) changes the dielectric environment around the NHSs. This impacts the modes (i.e., resonance frequencies, and widths) which are strongly coupled to the substrate, and thus helps distinguish them as those with strong versus weak substrate coupling.

Figures 2.17 show only the spectra acquired at 5, 10, 20, 30, 40, 50, 60, 90, 120, and 150 s. As displayed in each frame (a-j), the spectra can be most optimally fit to five Gaussians. Here, the emphasis will be given to the three lowest energy peaks in Figure 2.17 (brown, blue, and magenta), which constitute the D═ band. These modes are strongly excited in the SERS experiment setup where the angle of the incidence is expected to be ~24º in air, and ~18º in water for numerical aperture (NA) of 0.4 of the objective lens used. In addition, D═ modes are associated with hotspots (high field enhancement sites) yielding detectable SM signal. Thus, monitoring their evolution during the synthesis process is crucial.

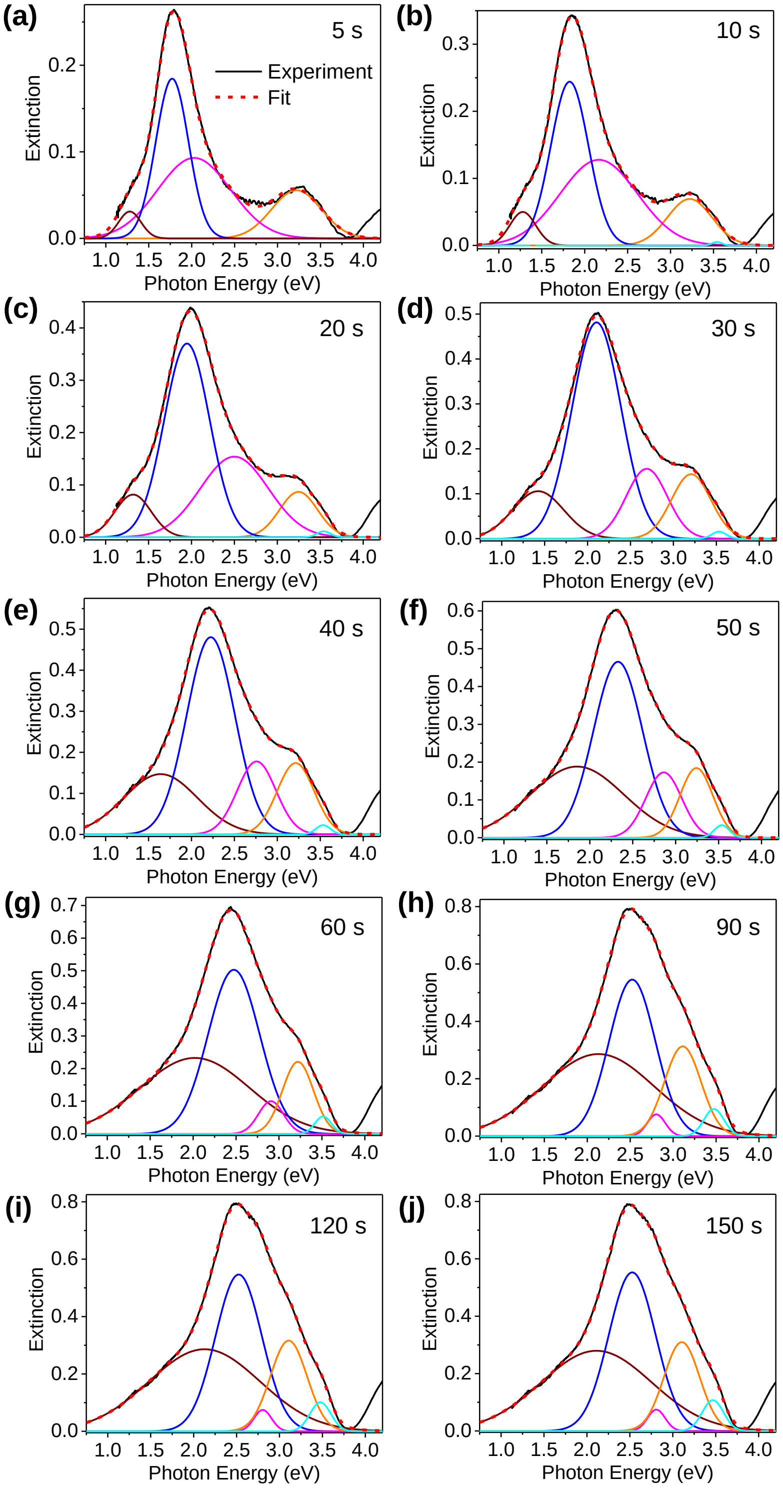

Figure 2.17. In-situ extinction spectra of Ag NHSs in 2 mM $AgNO_3$ solution during synthesis. Only the spectra acquired at 5, 10, 20, 30, 40, 50, 60, 90, 120, and 150 s of immersion are shown **(a-j)**, respectively. The spectra are fit to 5 Gaussians, color coded same as in Figure 2.6.

Figure 2.17 also reveals two Gaussians in the UV region, which spectrally match with $D\perp_1$ and MP. Although, the excitation field is expected to be parallel under normal incidence, and not excite $D\perp_1$, the beam employed by the UV-Vis spectrometer is not strictly collimated. Additionally, the retarded fields of the neighboring NPs acting on a NP have vertical components. Hence, $D\perp_1$ can be excited, at least weakly. Similarly, $D\perp_1$ and $D\perp_2$ are also observed in Figures 2.5a and 2.5b under s-polarized radiation and p-polarized radiation of normal incidence ($\theta=0^o$), respectively. When, the extinction spectrum of the substrate corresponding to 60 s reduction (Figure 2.17g) is acquired at incidence angle of 45° (Figure 2.18), $D\perp_2$ can be resolved, too. In Figures 2.17 and 2.18, the modes are coded with the same colors as in Figure 2.6.

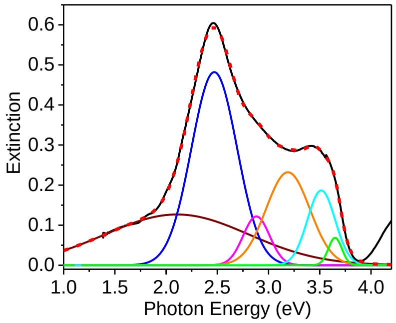

Figure 2.18. Extinction spectrum of the sample corresponding to Figure 2.17g for $\theta=45°$

Figures 2.19a and 2.19b provide the energy, integrated intensity, and the FWHM of the peaks, as a function of time, respectively. A significant blueshift is seen for all tree D═ (magenta, blue, and blue) during Ag reduction. The blueshift is attributed to decreased coupling with the underlying Ge film. The Ge film serves as the reducing agent and hence diminishes because of oxidation and dissolution in water during the Galvanic displacement. This finding underscores the significant degree of substrate coupling in NHSs and how it can be avoided with immobilization of the NHSs on the nanoposts (i.e., mushroom structures). As detailed in *Section 2.2.5*, the fraction of unconsumed Ge computed through baseline correction of the extinction spectra (Figure 2.20a) and thereby the amount of Ag reduced can also be quantified (Figure

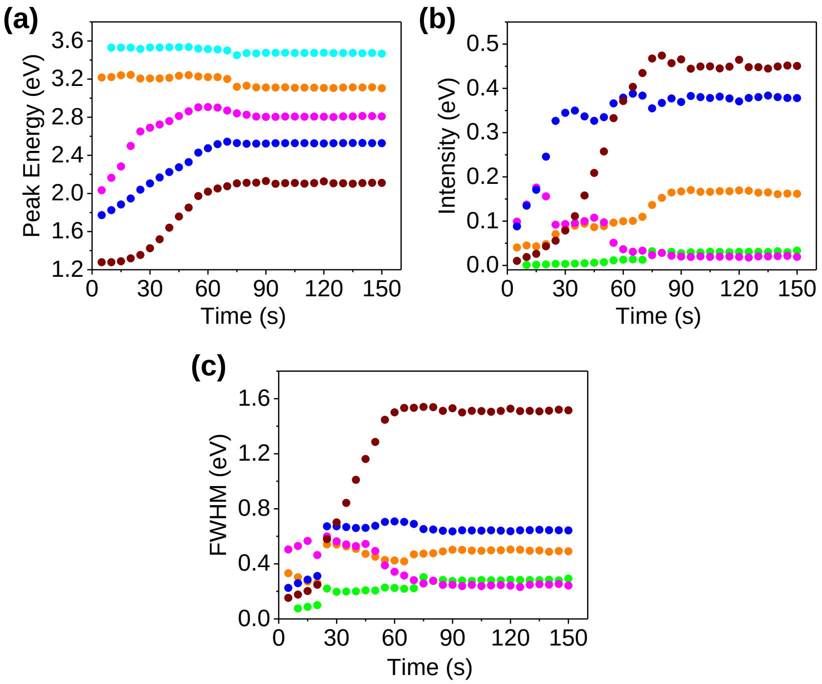

Figure 2.19. Time evolution of peak energy **(a)**, integrated intensity **(b)**, and linewidth (FWHM) **(c)** during in-situ reduction Ag NHS at 5 s intervals (colors as in Figure 2.15).

2.20b). As seen in Figure 2.20b, the Ag reduction, and hence the Ge consumption, is complete around 80s. This is also supported by the fact that around the same time (80s), the observed changes in the peak energies, intensities, and widths cease.

As seen in Figures 2.19b, the intensity of the highest energy parallel mode (magenta) starts to decrease after 15s. Simultaneously, its FWHM of decreases as seen in Figure 2.19c. Assuming the particle nucleation is homogenous, the particle density (number and size) increases with time during which the particles form dimers, trimers or chains. Thus, the number of isolated particles decrease over time. Hence, this mode (magenta) is assigned to $D{=}_{\text{isolated}}$ associated with weakly-coupled or uncoupled NHSs, $D{=}_{\text{isolated}}$. The reduction in the FWHM can be attributed to the reduced heterogeneous broadening due decreased number of particles contributing to this mode. Another contribution to $D{=}_{\text{isolated}}$ is likely due plasmon oscillations along the transverse axis of a dimer, trimer or tetramer (i.e., linear chains), which are again weakly coupled. For transverse oscillations in a linear chain, the dipole charges in NPs are separated by more than the average diameter and the coupling inside the chain (i.e., H-conjugation) is weak. Hence, frequency of the transverse mode is close to that for an isolated single particle [106, 107].

The $\mathrm{D}{=}$ bands at lower energy than $\mathrm{D}{=}_{\mathrm{isolated}}$, namely the blue and brown Gaussians, are attributed to strongly-coupled longitudinal oscillations in dimers and higher order linear chains (e.g., trimers, tetramers), $\mathrm{D}{=}_{\mathrm{dimer}}$ and $\mathrm{D}{=}_{\mathrm{chain}}$, respectively. In these coupled modes, the symmetric charge oscillations of the NPs are subject to attraction across the narrow gaps that account for decreased restoring force constants. Therefore, the resonances redshift with respect to $\mathrm{D}{=}_{\mathrm{isolated}}$. Accordingly, the lowest energy peak (i.e., $\mathrm{D}{=}_{\mathrm{chain}}$) is assigned to highest degree of attractive coupling (plasmon hybridization/bonding). The intensity kinetics in Figure 2.19b shows that while $\mathrm{D}{=}_{\mathrm{isolated}}$ starts to fade after 15s, the $\mathrm{D}{=}_{\mathrm{dimer}}$ continues to rise due to formation of new dimers. With increased density and size of NPs over time, the probability of formation of trimers and chains increases leading to higher excitation of $\mathrm{D}{=}_{\mathrm{chain}}$. As observed from Figure 2.19b, the kinetics of $\mathrm{D}{=}_{\mathrm{chain}}$ lag behind $\mathrm{D}{=}_{\mathrm{dimer}}$ (i.e., slower rise and later saturation) suggesting the highest degree of coordination associated with this band; that is, formation of trimers and tetramers take longer time than that of dimers. Further, the remarkably larger width of $\mathrm{D}{=}_{\mathrm{chain}}$ (Figure 2.19.c) is owed to heterogenous broadening due to multiple structures contributing to it, such as trimers, tetramers, etc. as well as distribution of gap lengths. The SEM image of Figure 2.1a confirms the abundance of linear chain structures such as trimers and tetramers, while linear chains of 5 NHSs or more are rare.

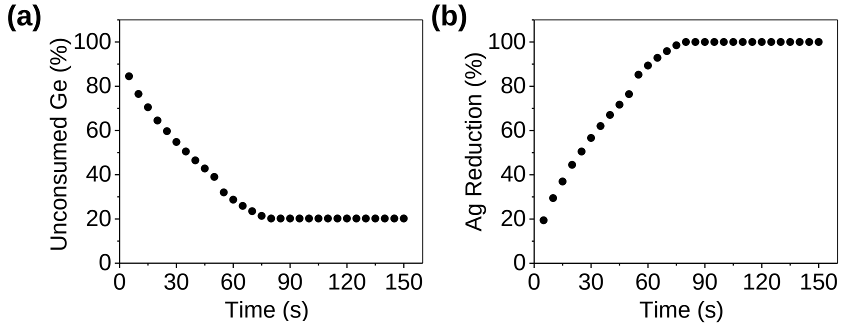

Figure 2.20. Amount of unconsumed Ge **(a)** and extend of Ag reduction (i.e. $(1-(t))/(1-Ks)$) **(b).**

Consistently, as seen from Figure 2.19a, among all $\mathrm{D}{=}$ modes (magenta, blue, brown), $\mathrm{D}{=}_{\mathrm{chain}}$ (brown) exhibits the slowest blueshift. While $\mathrm{D}{=}_{\mathrm{chain}}$ continuously blueshift during the course of NP synthesis due to decreasing substrate coupling led by consumption of Ge, the increasing particle−particle coupling in this mode redshifts the plasmon resonance. As a result, the particle−particle coupling lessens the rate of the net blueshift. On the other hand, the observed blueshift is faster for $\mathrm{D}{=}_{\mathrm{dimer}}$ (blue) and the fastest for $\mathrm{D}{=}_{\mathrm{isolated}}$ (magenta) due to lower and no particle−particle couplings, respectively. No blueshift is observed for the modes in the UV, verifying the computational results (Figure 2.10b), that is, insignificant substrate coupling for these modes ($\mathrm{D}\perp$ and MP). For a plasmonic sphere, the radial component of the electric field scales as $r^{(l-1)}$ and $r^{(-(l+2))}$ inside and outside the sphere, respectively, where r is the radius and l is the angular momentum number that characterizes the charge distribution of the plasma oscillation (1 for dipolar, 2 for quadrupolar, etc.). Therefore, for the multipolar mode, MP, the electric field is more bound to the surface than that for the dipolar mode. A similar situation is expected for the hemispheres. Hence, MP mode oscillations are less susceptible to coupling between NPs as well as with the substrate and environment. Based on the discussions made in this section, as well as in *Section 2.3.2*, all plasmon modes and their associated nanostructures are illustrated in Figure 2.21.

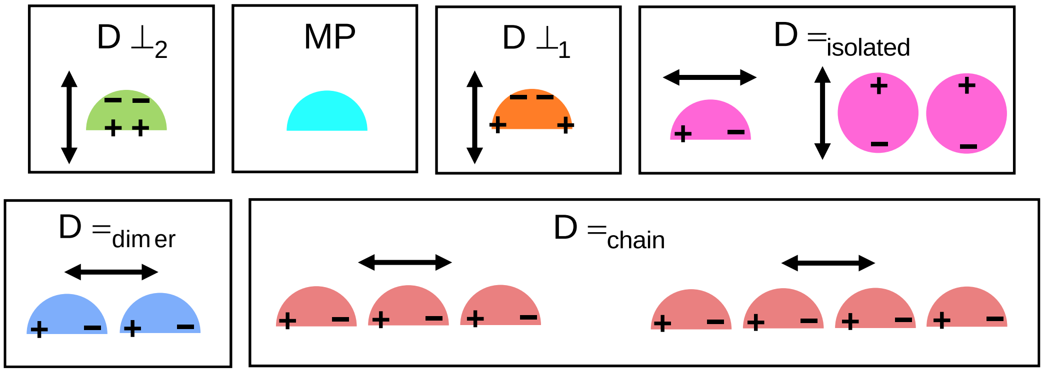

Figure 2.21. Illustration of mode configurations and associated nanostructures coded in the same colors as in Figures. 2.6 a-i. The arrows indicate the orientation of the dipole moments, associated with the modes.

2.3.5. Ag Nanohemispheres Synthesized by PVD

Plasmonic properties of Ag NHSs deposited directly on glass substrates by physical vapor deposition (PVD) were also investigated. Figure 2.22a and Figure 2.22b shows the extinction spectra of Ag NHS at various incidence angles (θ) using s- and p-polarized incident radiation, respectively. Definitions of incidence angle and s- and polarizations are as in Figure 2.5c.

Ag NHSs deposited directly on glass show similar dependence to incident polarization and angle as in Ag NHSs synthesized by reduction. As seen in Figure 2.22c, UV region of the spectrum for p-polarized incidence at 60° is deconvoluted to 3 peaks (Gaussians) at close frequencies to those for Ag NHSs synthesized by reduction. Further, these modes are also excited in the presence of incident field having a normal component to the substrate (i.e., p-polarization and oblique incidence). Therefore, the resonances at 390, 354 and 339 nm are assigned to $D\perp_1$, MP, $D\perp_2$, respectively. The slight shift of the mode frequencies from those in Ag NHSs (i.e., 362, 344, 335 nm) is may be attributed to minor deviation from hemispherical

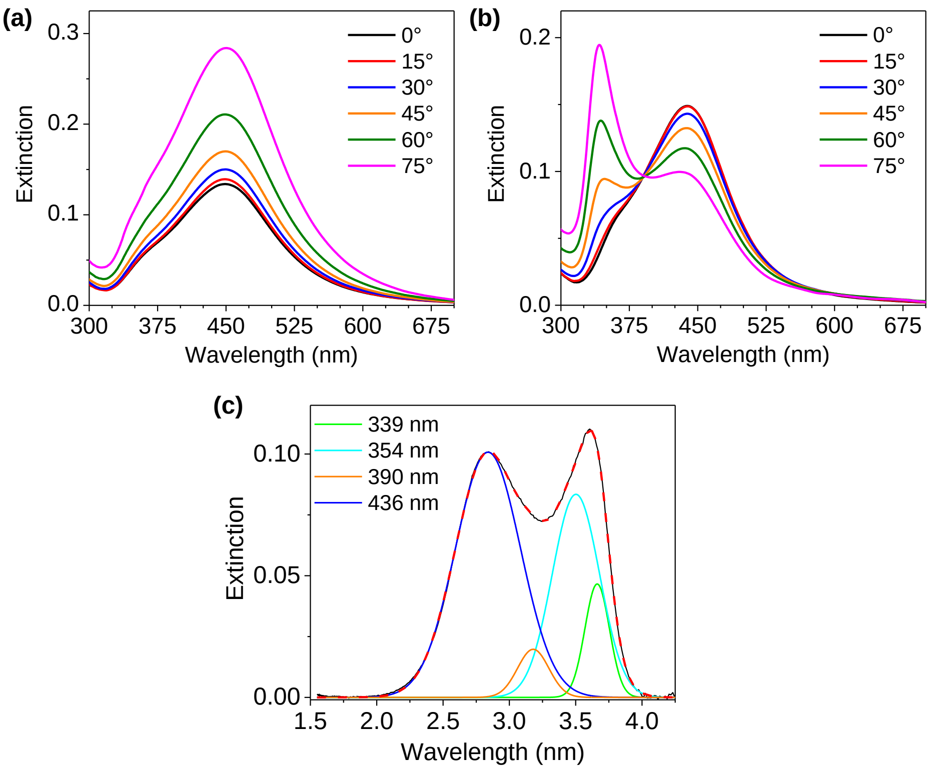

Figure 2.22. Extinction spectra of Ag NHSs synthesized by thermal evaporation on glass at varying angle of incidence (0-75$^{\text{o}}$) for s-polarization **(a)** and p-polarization **(b)**. Deconvoluted peaks of the extinction spectrum for p-polarized incidence at 60$^{\text{o}}$ **(c)**.

shape (e.g., contact angle wider than 90°). In addition, higher substrate coupling is expected for Ag NPs deposited directly on glass compared to the NHS that are separated from the glass substrate by Ge nanoposts in mushroom-like structures.

On the other hand, only a single Gaussian is resolved for the parallel mode, D═. The D═ band (436 nm) is blueshifted with respect to that in the Ag NHSs immobilized on Ge nanoposts (482 nm), despite a stronger substrate coupling expected. Hence, the blueshift of D═ is attributed to weaker interparticle coupling. This inference is supported by the AFM image of the Ag NPs in Figure 2.23, where a wider interparticle separation is seen. Further, a broader distribution of particle diameters and a higher degree of disorder are observed in Figure 2.23. While D═ band is expected to be dominantly contributed by D═$_{\text{dimer}}$, it is curious that D═ of higher order coupled particles cannot be resolved despite the fact that trimers and tetramer linear chains are seen in Figure 2.23, too. It is likely that due to higher degree of disorder and longer interparticle separation, extended linear conjugates such as trimers, tetramers and higher order chain structures do not assemble as efficiently, explaining the absence of $D{=}_{\text{chain}}$ resonance. Further, it is also possible that deconvolution of the resonances is hampered by the peak broadenings because of higher damping due to substrate coupling as well as broader distribution of particle sizes and separations.

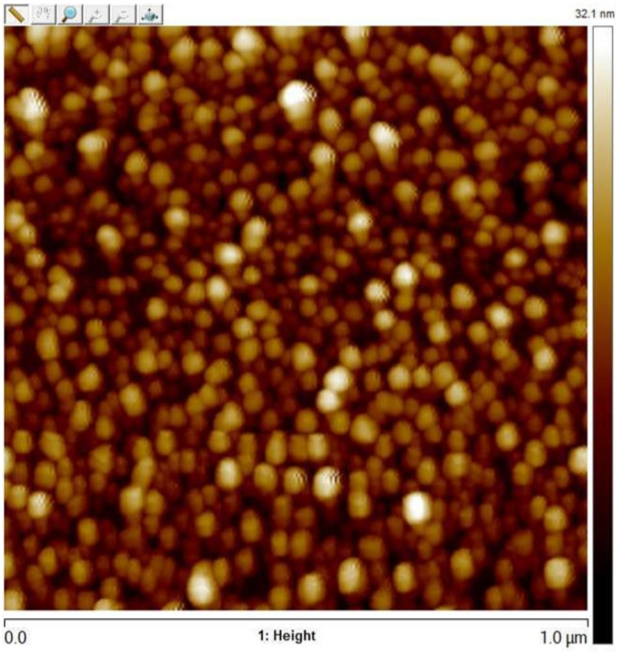

Figure 2.23. AFM image of the Ag NPs synthesized by PVD on glass.

2.4. Conclusions

NP assemblies fabricated by deposition (i.e., chemical or physical) on various substrates are commonly used as plasmonic devices. When particles are directly deposited on a surface, the thermodynamics generally favor the truncated sphere geometry (e.g., hemisphere). Often, such particles are mischaracterized as being spherical using conventional techniques (e.g., AFM, TEM, or excitation/scattering spectroscopy) where oblique-angle characterization is not common. Consequently, their optical properties are also assumed to be same as those of spherical nanoparticles.

As experimentally demonstrated and computationally elucidated in the present work, NHSs exhibit remarkably different plasmonic characteristics as compared to nanospheres. The broken symmetry by asymmetric particle shape leads to dipolar modes parallel (in-plane) and normal to the base (out-of-plane), which are significantly different in terms of energy, excitation dependence on polarization, and electromagnetic coupling. While the perpendicular modes exhibit essentially no substrate/particle coupling, the parallel modes strongly couple to the substrate which may be beneficial for efficient light coupling in photovoltaic applications.

The monitoring of NP reduction indicates that excited parallel modes are strongly coupled. The extinction associated with these coupled modes is resolved to two resonance bands, which we attribute to dimers and higher order chains (e.g., trimers, tetramers). The polarization dependence of the modes has interesting consequences. For example, if a NHS monolayer is employed as a SERS substrate, the coupled parallel mode(s) will be instrumental. Excitation and scattering of these modes dominantly involve parallel polarization, where a low numerical aperture lens will be more efficient than a high numerical aperture one. Similarly, the excitation dependence on incident angle should be taken into account in other plasmonic applications employing NHSs.

Unlike the parallel modes, the perpendicular dipolar modes exhibit insignificant particle−substrate and particle−particle coupling. This is also verified by significantly narrow line width of $D\perp_2$ in experiments, as well as in computations. Interestingly, experimental linewidth of $D\perp_2$ is narrower than the computed line width of a single NHS in vacuum which is attributed to suppression of radiative damping. The significantly narrow line width of $D\perp_2$ in Ag NHSs is ideal for LSPR application, due to which high resolution in the changes of LSPR resonance can be obtained. Additionally, the $D\perp$ modes observed in the UV region makes NHSs a good candidate for UV plasmonics.

The strong field concentrations shown to be induced at the sharp edges of a NHS may enhance hot electron injection to the substrate in a photocatalyst. These higher field concentrations at the edges also account for enhanced coupling with adjacent NHSs. Interestingly, unlike in a spherical dimer, where the field intensity peaks in the middle of the gap, the maximum field in a NHS dimer gap occurs on the metal surface (i.e., at the edges), overlaying with the chemical enhancement. Hence, higher enhancement factor SERS is anticipated with coupled NHSs. Indeed, the next chapter of the present work (*Chapter III*) will discuss the implications of these unique plasmonic properties for SERS by investigating the detection of single molecules on Ag-nanohemispheres-on-Ge-nanoposts substrates.

Acknowledgements: This chapter (*Chapter II*) was previously published as Topal Ç.Ö., Jaradat H. M., Karumuri S., O’Hara J. F., Akyurtlu A., and Kalkan A. K., *Plasmon resonances in nanohemisphere monolayers.* The Journal of Physical Chemistry C, 2017. **121**(42): p. 23599-23608.

CHAPTER III

DETECTING SINGLE MOLECULES USING SILVER NANOHEMISPHERE MONOLAYERS

1. Introduction

Single molecule (SM) spectroscopy is a powerful technique for resolving individual properties of molecules, and hence provide direct information on their physical chemistry in the absence of ensemble averaging. One of the spectroscopy techniques capable of detecting SMs is Surface Enhanced Raman Scattering (SERS). SERS is the amplification of Raman scattering of molecules, which are absorbed on, or at proximity of (i.e., within 10 nm) metal nanostructures [108, 109]. It has been well established in the literature that field concentrations in narrow gaps between plasmonic Ag NPs can exceed two orders of magnitude, allowing for detection of SERS from SMs. The typical electromagnetic SERS enhancement factors reported for SM detection are on the order of 10^8 [97, 98, 110]. In the presence of chemical enhancement, the total SERS enhancement factors can approach 10^{12} [97, 98, 110-112]. Given that electromagnetic SERS enhancements as high as 10^{14} are calculated in the junction of nanohemisphere (NHS) dimers in *Chapter II*, SM detection is anticipated with Ag nanohemisphere-on-Ge nanopost substrates. Indeed, using these substrates, our group has studied various analytes (i.e., photoactive yellow.

protein (PYP), green fluorescent protein (GFP), hemoglobin, quantum dots, and azobenzene (AB)) at SM level [30, 31, 112-114]

The high sensitivity chemical detection with coupled NHS dimers was also anticipated earlier by Attanayake et al. [75]. However, the correlation between the plasmonic properties of NHSs and the observed SM signal, has not been investigated before. Hence, in this chapter, we would like to demonstrate the SM detection of two analytes, wild-type GFP (wt-GFP) and AB, in the light of our investigation into the plasmonic properties of NHSs in *Chapter II*.

Our use of two fundamentally different analytes (i.e., wt-GFP and AB), demonstrates the capability of detecting various system using Ag-on-Ge substrates. GFP is a protein containing a chromophore enclosed by a β-barrel (Figure 3.1). The molecular dynamics of the chromophore is restrained by the β-barrel, and hence the radiationless relaxation pathways are blocked. Further, the β-barrel protects the chromophore from fluorescence quenchers, making GFP a highly efficient fluorophore with a quantum yield of 0.8 [115-121]. The β-barrel is also instrumental to weak interaction of the chromophore with the metal surface in our SERS measurements. GFP chromophore has two well-established stable *cis* conformations: protonated (A) state and deprotonated (B) states [122, 123]. As demonstrated by our group, GFP also has a protonated (C) and deprotonates (D) states of a non-*cis* (non-planar) conformer [31, 114]. AB, on the other hand, has a direct electronic interaction with the metal substrate resulting in significant changes in its conformational states and dynamics. As will be discussed in detail in Chapter IV, AB has three distinct adsorption configuration for both of its isomers (i.e., *trans* and *cis*). Using Ag-on-Ge SERS substrates, we not only resolve different states of both analytes, but also capture the transitions between them at SM level.

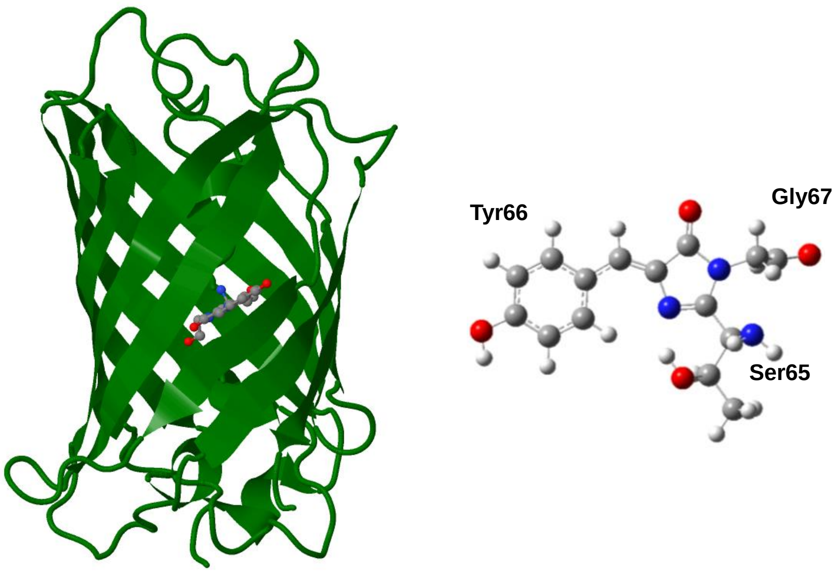

Figure 3.1. Tertiary structure of wt-GFP: The barrel with the chromophore in the center (left). Figure was constructed using Protein Data Bank Entry 1GFL. Ball-stick model of the GFP chromophore (red:O; blue:N; light blue: C) (right).

Since its first demonstration in 1997 [124, 125] detection of single molecules (SMs) by SERS has been reported for numerous molecules and substrates [32, 110, 126-131]. Even more significant than just detecting SMs, is the promise of using SERS in resolving conformational and electronic states/transitions in SMs in the absence of ensemble averaging. However, only a limited number of studies have exploited this potential of SM-SERS. A few of these milestones were in the area of exploring protein structure and dynamics, where the first study monitored the protonation/deprotonation of single green fluorescent proteins (GFP) with a time resolution of 5 s [132]. Later, single photo-active yellow protein (PYP) proteins were “watched in action” in 1-s time resolution while the chromophore underwent protonation-deprotonation, as well as *cis*-*trans* isomerization during the protein photocycle [30]. Most recently, the vibrational spectrum of a non-*cis* (i.e., gauche) form of wild-type GFP chromophore was observed by SM-SERS [31]. The same study also resolved the transitions between the *cis* and the non-*cis* conformations, as well as the transitions between the protonated and deprotonated forms of both conformations in 50-100 ms intervals. SM-SERS has also been utilized in elucidation of chemical reactions. Electrochemical events, including electron transfer dynamics, sequential reduction/oxidation events, and site-specific chemical reactions in SMs have been explored by SERS [133-140]. Recently, SM-SERS has been applied to resolving catalytic reactions, where plasmonic particles not only serve as the SERS substrate, but also as the catalyst [141, 142]. These studies emphasized the uniqueness of SM-SERS technique where chemical events are induced and resolved by the plasmonic particles simultaneously.

Despite SM-SERS being demonstrated for various analytes by several groups, as the above-cited literature represents, it took years of extensive research to prove the reliability of the technique to measure single molecules. Early studies of SM-SERS were performed using ultra-low concentrations of analytes on Ag colloids (~1 molecule per colloid or per scattering volume) [124, 125, 129, 131]. In these studies, the argument that the observed signal must originate from a SM since there cannot be more than one molecule per measurement volume was used as a proof for SM detection. It quickly became clear that the lack of a reliable method for calculating the size of the particles used in these studies lead to errors in calculated molecule:particle ratios [124, 143]. Further, it was observed that only a small fraction of colloids lead to detectable SERS signal, making any statistical argument unreliable [144, 145]. Thus, further evidences were required to prove the SM nature of the observed SERS signals.

Over the years, several techniques have been proposed as direct or indirect proof of SM detection in SERS studies such as, intensity and frequency fluctuations in SERS spectra [111, 112, 146-149], polarization of SERS signal [124, 150, 151], Poisson distribution of quantized SERS signals [125], bi-analyte techniques [127, 145, 152, 153], and spectral fluctuations [127, 154]. While some of these techniques (i.e., Poisson distribution of quantized SERS signals and polarization studies) were shown to be misleading, some of them, such as bi-analyte technique, were proven to be direct proof of SM-SERS detection.

In the present study, we use some of the well-established methods listed above to prove the SM nature of the observed SERS signals on Ag NHSs. Further, we put forward additional evidences supporting SM detection in which we resolve dynamic events such as conformational transitions, protonation/deprotonation, and surface diffusion of a molecule in and out of a hotspot. Unique from many SM-SERS studies in the literature where the time resolutions are on the order of 1s, we detect SMs using integration times of 40-100 ms. This allows us to resolve dynamic events that could not be resolved in previous SM studies due to long integration times used. In addition, we resolve variations in charge transfer reactions between an AB molecule and Ag surface. We attribute the observed variations to the continuous desorption−re-adsorption nature of the surface diffusion, which would only be observed at SM level in the absence of statistical averaging. This provides a direct proof of SM detection in the present study. Further, it demonstrates the role of analyte−metal interactions, and hence the chemical enhancement, in SM-SERS spectra.

Another technique we propose as an evidence for SM detection is the imaging of the Raman flashes (i.e., Raman scattered light) of SMs. In this technique, Raman flashes in the illuminated laser spot during time-series SERS acquisition of wt-GFP are imaged. The analysis of the Raman flashes reveal similar intensity fluctuations observed in SM-SERS spectra. In addition, the flashes are observed to occur repeatedly at certain pixels. Hence, hotspots yielding detectable SM signals are inferred to be specific sites. Accordingly, we attribute these flashes to the Raman images of single wt-GFP molecules whose resolution is limited by diffraction as well as CCD image pixel size.

3.2. Methods

3.2.1. SM-SERS Acquisitions

SERS substrates were prepared using the protocol detailed in *Section 2.2.1* of *Chapter II*. Briefly, the NP synthesize was performed by immersion of ultrathin (i.e., 4.5 nm thick) Ge films in $AgNO_3$, where Ge functions as the reducing agent resulting in formation of nanohemispheres (NHSs). A unique feature of this Galvanic displacement technique is the consumption of Ge everywhere, except just below the center of NHSs, resulting in mushroom-like structures. NHSs are essentially immobilized on Ge nanoposts of uniform height from the glass substrate. In SERS measurements of AB and wt-GFP, typical NP synthesis times of 35-40 s and 25-30 s were used, respectively. Figure 3.2 shows the extinction spectra of a SERS substrate at 30 s synthesis (i.e., immersion) time measured in-situ during nanoparticle growth. During the in-situ measurements, the substrates are immersed in a $AgNO_3$/water solution which also represents the conditions during SERS acquisitions which are performed at liquid analyte/substrate interface as detailed below.

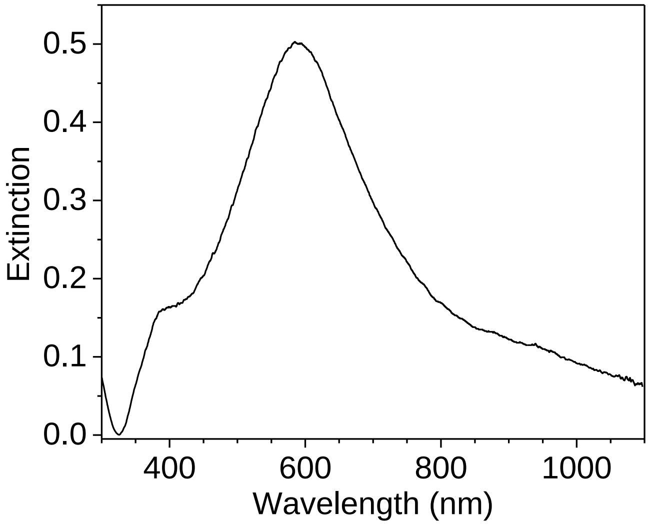

Figure 3.2. Extinction spectra of NHSs in 2 mM $AgNO_3$ solution at 30 s immersion acquired in-situ during particle growth.

AB was purchased from Sigma Aldrich. wt-GFP was gifted by Drs. Klaas Hellingwerf and Johnny Hendriks of University of Amsterdam in lyophilized powder form. The recombinant protein was expressed in Escherichia coli as fused to a polyhistidine tag at the N-terminus and purified in a nickel column. Optical absorption and fluorescence spectra conformed exactly to those of wt-GFP reported in the literature [117]. For SERS acquisitions, AB and GFP was dissolved and diluted in de-ionized water to a final concentration of 1×10^{-8} and 1×10^{-9} M, respectively.

In a typical SERS acquisition, a 1.5 μL aliquot of analyte solution of AB or wt-GFP was spotted on a substrate. In order to prevent the aliquot from drying during acquisition, the substrate was sealed inside an optical cell (Starna Cell; $12.5\times3.5\times45.0$ mm^3) along with a small piece of wet tissue. SM-SERS spectra were collected using a WITec Alpha300M Raman Microscope with a 600 g/mm grating. A 532 nm Nd:YAG (neodymium-doped yttrium aluminium garnet; Nd:Y3Al5O12) laser was employed as the excitation source. The SERS signal was collected from the substrate surface ((i.e., Ag nanoparticles) by focusing the laser to the aliquot-substrate interface using a 20X objective lens with a numerical aperture of 0.4. A laser spot size of 2 μm, and 5 μm was used for AB and wt-GFP, respectively. The incident laser power was 650 and 700 mW for AB and wt-GFP, respectively. Subsequent SERS spectra (time-series) of AB and wt-GFP were continuously recorded for 2 minutes in 40 and 100 ms intervals, respectively.

3.3. Results and Discussion

3.3.1. Single Molecule SERS Jumps

During time-series SERS acquisitions, sudden appearance of Raman peaks are observed as demonstrated for AB and wt-GFP in Figure 3.3 and Figure 3.4, respectively. As seen in both figures, only a weak background signal is observed before the appearance of Raman peaks. The observed Raman peaks appear for less than a second before vanishing, leaving behind a weak background signal. These alternating on/off periods in the SERS spectra, or commonly referred as spectral "jumps" in the literature, are attributed to surface diffusion of a SM in and out of a hotspot [148, 155-157].

It is well established in literature that the hotspots capable of producing detectible SM-SERS signals have high spatial localization [158-161]. The calculated electromagnetic field distributions and the corresponding field enhancement factor maps discussed in *Section 2.3.3* of *Chapter II,* also supports the high localization of hotspots in NHS dimers. Experimentally, this means that a molecule will give detectible SERS signal when it diffuses into this highly localized regions, creating the on periods as in Figures 3.3 and 3.4. However, when the molecule diffuses out of the hotspot, the SERS signal will fall below the detectable level, and thus the signal will turn off.

While the observation of such temporal jumps is consistent with the capturing of SMs, it does not present a conclusive proof of SM-SERS by itself. Other processes such as photo or thermal-induced (due to photo-induced substrate heating) oxidation, desorption, and dissociation of the analyte, as well as surface reconstruction in plasmonic particles, may also give rise to on/off periods in SERS signal [156, 159, 162]. Further, in the hotspots, where the SM signal originates from, these photo-driven processes are expected to be enhanced. Thus, additional evidences are required to validate the SM nature of the observed SERS signal. In the following subsections, additional evidences supporting the SM nature of the SERS signal collected using the Ag-on-Ge substrates are discussed.

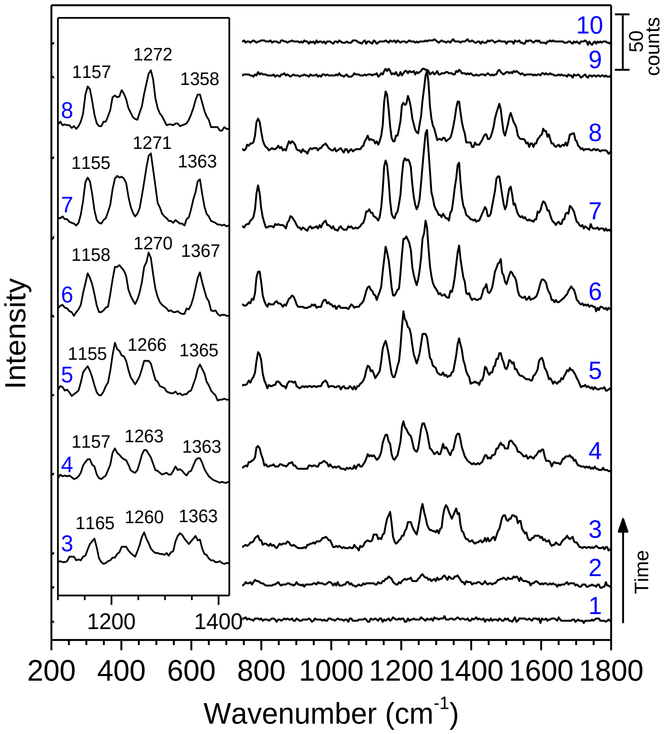

Figure 3.3. Time-series spectra showing a spectral jump associated with capturing a single AB molecule at 40 ms intervals. Inset shows the frequency and intensity fluctuations of the SERS peaks in 1100-1420 cm^{-1} range.

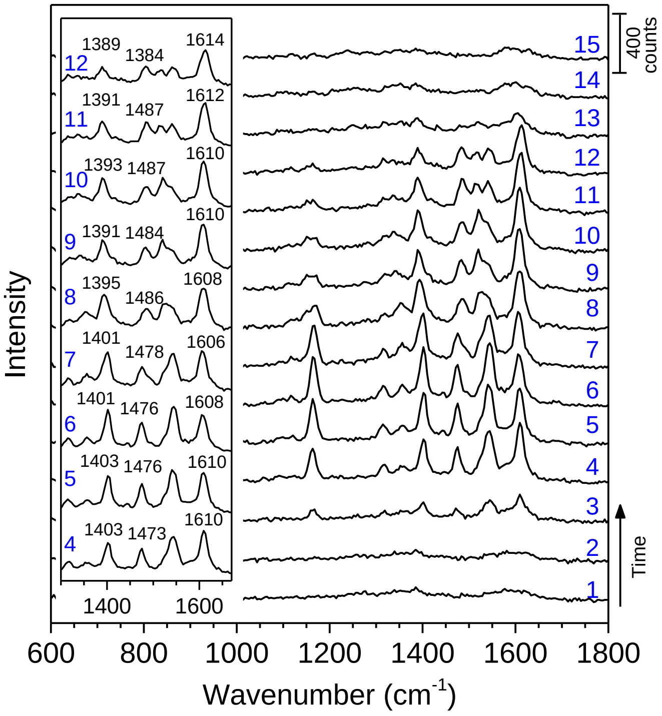

Figure 3.4. Time-series spectra showing a spectral jump associated with capturing a single wt-GFP protein at 100 ms intervals. Inset shows the frequency and intensity fluctuations of the SERS peaks in 1300-1670 cm^{-1} range.

3.3.2. Spectral Wandering and Relative Intensity Fluctuations

Detailed analysis of a spectral jump as in Figure 3.3 and Figure 3.4 reveals random frequency shifts (±5 cm^{-1}) (spectral wandering) and relative intensity fluctuations in the SERS peaks as seen in the inset of Figure 3.3 and Figure 3.4. These temporal fluctuations are attributed to statistical variations in the adsorption configuration, and therefore to variations in the alignment of transition moment directions of the vibrational modes with enhanced field due to surface diffusion. In agreement with SM-SERS literature, the observed fluctuations in the time-series SERS spectra of both AB and wt-GFP is another evidence of capturing single molecules [111, 112, 146-149]. Observation of such fluctuations suggests that the diffusion of an AB and wt-GFP molecule from one adsorption site to another on the Ag surface occurs at a time scale comparable to 40 ms and 100 ms, which is the signal integration time used for detection of AB and wt-GFP, respectively,

3.3.3. Fluctuations in Overall SERS Intensity

Different than the relative intensity fluctuations, changes in the overall intensity of the SERS signal is also observed in some spectral jumps of AB as in Figure 3.5. By carefully analysing the intensities of the peaks at 1140, 1195, 1395 and 1440^{-1} in each spectra, we constructed the normalized peak intensity vs time plot as shown in Figure 3.5. The peak intensities were normalized by those at 0.04 s (onset of the SERS jump). Normalized intensities allow us evaluate the effective enhancement of the peaks within the hotspot by removing the effect of SERS selection rules. As observed in Figure 3.5b, all peak intensity fluctuations follow the same trend. The observed variations in overall intensities are attributed to the surface diffusion of the molecule within the hotspot which results in variation of the SERS enhancement experienced by the molecule. As discussed earlier, SERS enhancement has two major contributors; electromagnetic enhancement and chemical enhancement. Hence, it is important to discuss the contribution of both mechanisms to the fluctuations observed in Figure 3.5.

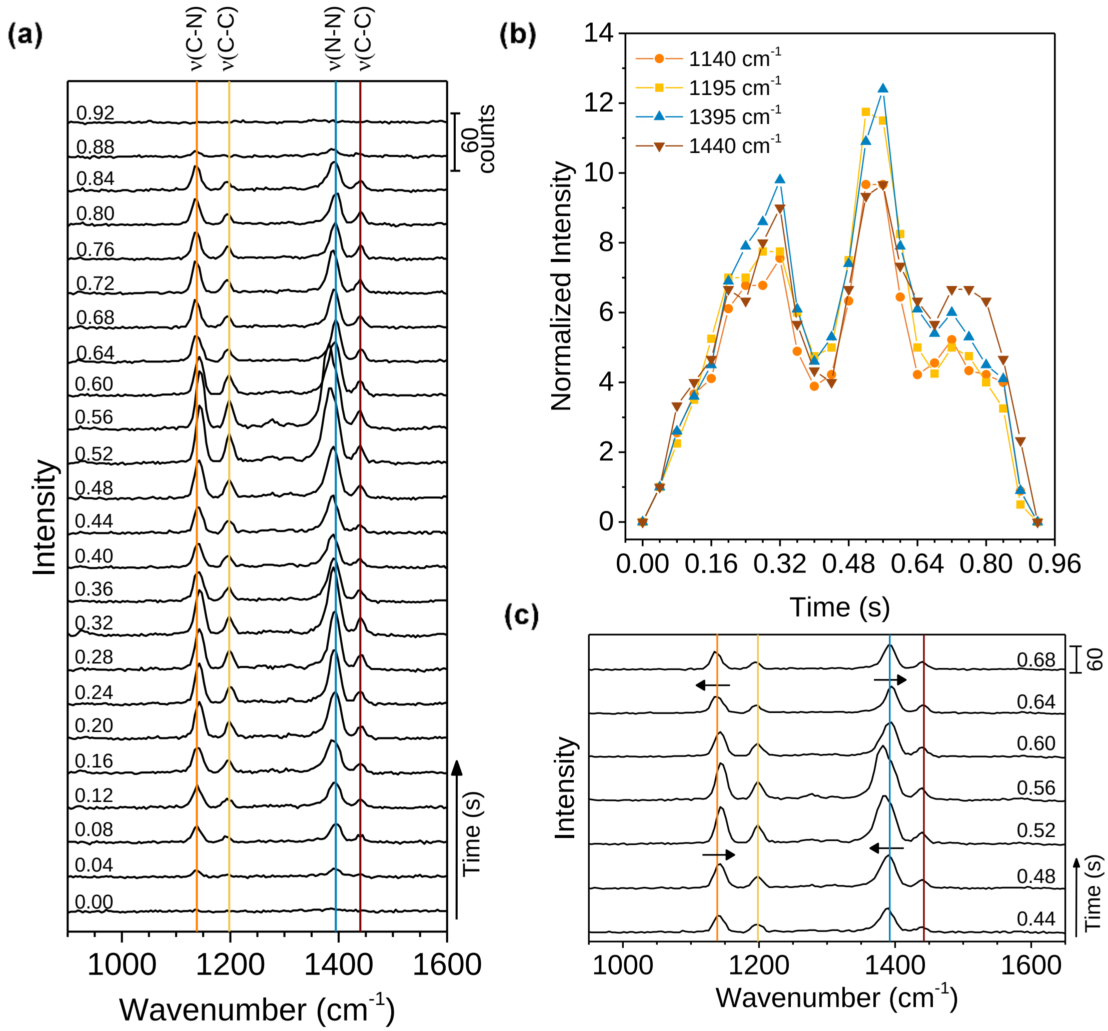

Figure 3.5. A spectral jump showing fluctuations in overall intensity of the signal in the time-series SERS spectra of an AB molecule **(a)**. Normalized peak intensity vs time plot of the four distinct SERS peaks in (a) which are color coded as orange, yellow, blue and brown **(b)**. The spectra between 0.44-0.68 s in (a) showing synchronized intensity and frequency fluctuations **(c)**. Signal integration time is 40 ms.

The electromagnetic SERS enhancement factors calculated based on the field enhancement factors for 65 nm NHS dimers with 2 nm interparticle separation (Figure 2.16) is given in Figure 3.6. As shown in Figure 3.6, the EF at the gap-metal interface is (±1 nm from the center of the gap), is calculated to be ~1×10^{14}. Only 2 nm away from the interface (at ±3 nm), the EF reduces two orders of magnitude. Further, the EF reduces four orders of magnitude at 4.3 nm away from the surface (at ±5.3 nm). Accordingly, significant variations in electromagnetic SERS enhancement experienced by a molecule is expected during surface diffusion within the hotspot region. Indeed, it is observed in Figure 3.5 that the overall SERS signal gradually increases and decreases in the beginning and at the end of the spectra. This is attributed to the surface diffusion of the molecule in an out of a hotspot which supports the EM contribution to the observed fluctuations, particularly in the beginning and at the end of the spectra.

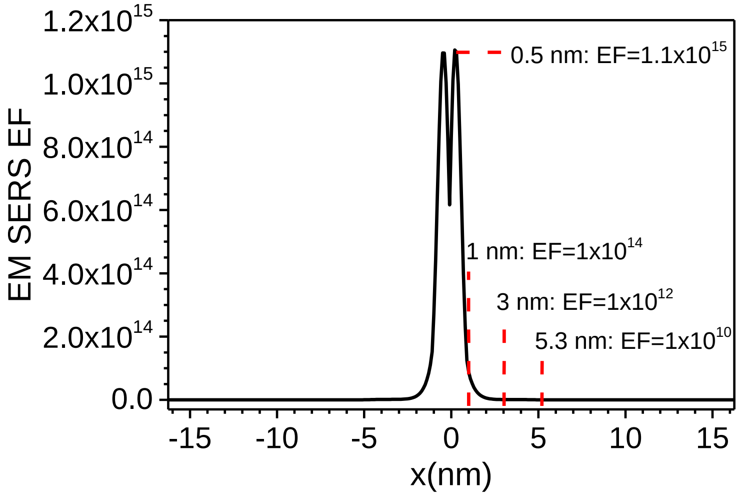

Figure 3.6. Electromagnetic SERS enhancement factor (EF) calculated using field enhancement factor profile along the dimer axis of two NHSs given in Figure 2.16b. The interparticle separation is 2 nm. The EF at various locations of the hotspot is given in the figure.

Intriguingly, during the intense fluctuations observed in 0.32-0.68s time regime in Figure 3.5, significant frequency shifts (±10 cm^{-1}) in 1140 and 1395 cm^{-1} modes are observed. For example, as shown in Figure 3.5c, in the time regime between 0.44 s and 0.60 s, where the peak intensities increase, the peaks at 1140 and 1395 cm^{-1} exhibit a synchronized upward and downward frequency shift, respectively. An opposite trend is observed in the time regime between 0.60 s and 0.68 s, where the peak intensities decrease. On the other hand, the frequency shifts in 1195 and 1440 cm^{-1} peaks in 0.44-0.68 s time regime are observed to be insignificant. Interestingly, modes at 1195 and 1440 cm^{-1} are related to the ring stretching vibrations (i.e., υ(C─C)) while the modes at 1140 and 1395 cm^{-1} are related to the vibrations of the azo-bridge (N═N) (i.e., υ(C─N) and υ(N═N), respectively). The origin of the observed selective frequency fluctuations in vibrational modes related to the azo-bridge of AB molecule might be due to a charge transfer process between the azo-bridge and Ag indicating the contribution of chemical enhancement to the observed SERS signal.

It has been studied in the literature that the Raman efficiency of molecules adsorbed onto metal surfaces may result in broadened or shifted adsorbate electronic states, or formation of new electronic states as a result of charge transfer between molecule and metal [103-105]. As demonstrated for crystal violet (CV) [163] and rhodamine 6G (R6G) [149] at SM level, charge transfer reactions can induce significant intensity fluctuations in selected modes. For example, in SM-SERS spectra of R6G, the modes at 615 and 774 cm^{-1} fluctuate in synchronized fashion while the remaining modes show no fluctuations [149]. The authors of this study attributed the observed fluctuations to the variation in charge transfer energy which depends on the local work function of the metal at specific adsorption sites. This indicated that the surface diffusion of the molecule occurs as subsequent desorption−re-adsorption events. In the present study, we don’t observe intensity fluctuations in selected modes. However, we observe selective frequency fluctuations in the modes related to the azo-bridge, the site associated with adsorption of AB to the metal surface. Thus, we attribute the intense fluctuations coupled with frequency fluctuations in selected modes observed in 0.32-0.68 s time regime (Figure 3.5) to variations in charge transfer energy (i.e., chemical enhancement) between AB molecule and Ag surface during its surface diffusion. Such observation provides a direct proof of desorption−re-adsorption nature of the surface diffusion of AB on Ag surface, and presents a concrete proof of SM detection in the present study.

3.3.4. Observation of Conformational Changes

Spectral jumps also exhibit sudden disappearance of certain peaks with subsequent appearance of new peaks with spectral shifts exceeding ±15 cm^{-1} as shown in Figure 3.7 for AB, and in Figure 3.8 for wt-GFP. Compared to the random fluctuations mentioned earlier, these large spectral shifts lasts for longer time length.s Since a molecule can be in a single conformation at a time, such spectral changes are attributed to transitions between different states of AB and wt-GFP. The AB SERS jump in Figure 3.7 shows a conformational transition from *t*-AB and *c*-AB. On the other hand, the wt-GFP SERS jumps exhibits both conformational (*cis* (B) ↔ *non-cis* (D)) and chemical transitions (deprotonated (D) → protonated(C)) as observed in Figure 3.8a and Figure 3.8b, respectively

Ensemble-averaged measurements cannot resolve such transitions where SERS signal is integrated from different state populations of the molecule. Thus, observing such conformational changes in SERS jumps provides another direct evidence for capturing SMs.

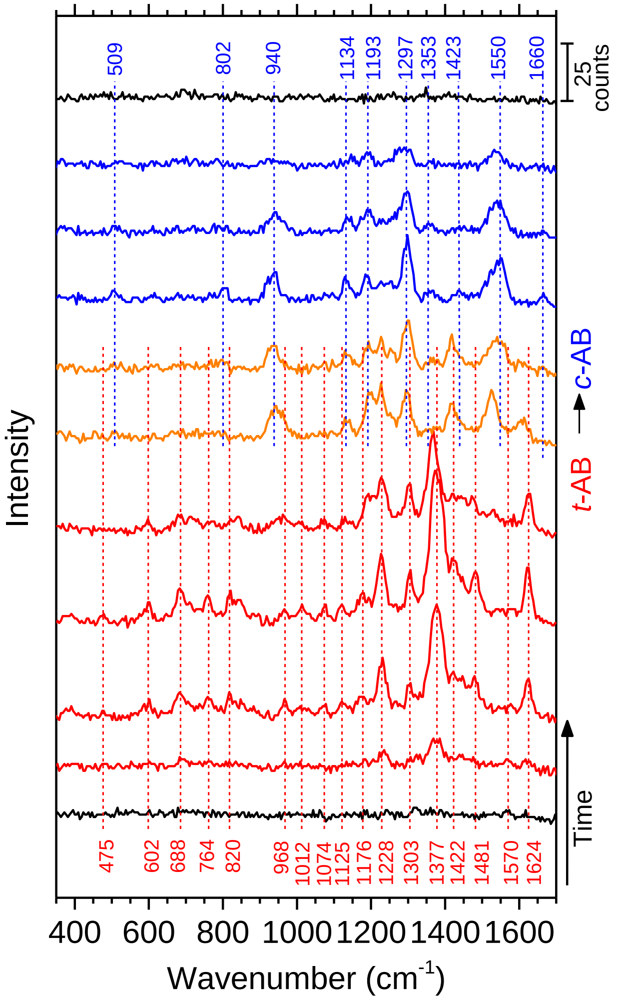

Figure 3.7. Time-series spectra showing *tran* → *cis* switching of a AB molecule on Ag NPs at 40 ms intervals. The red and blue colors represent *trans* and *cis* isomers, respectively. The orange spectra containing the markers of both isomers is transitioning between *trans* and *cis*.

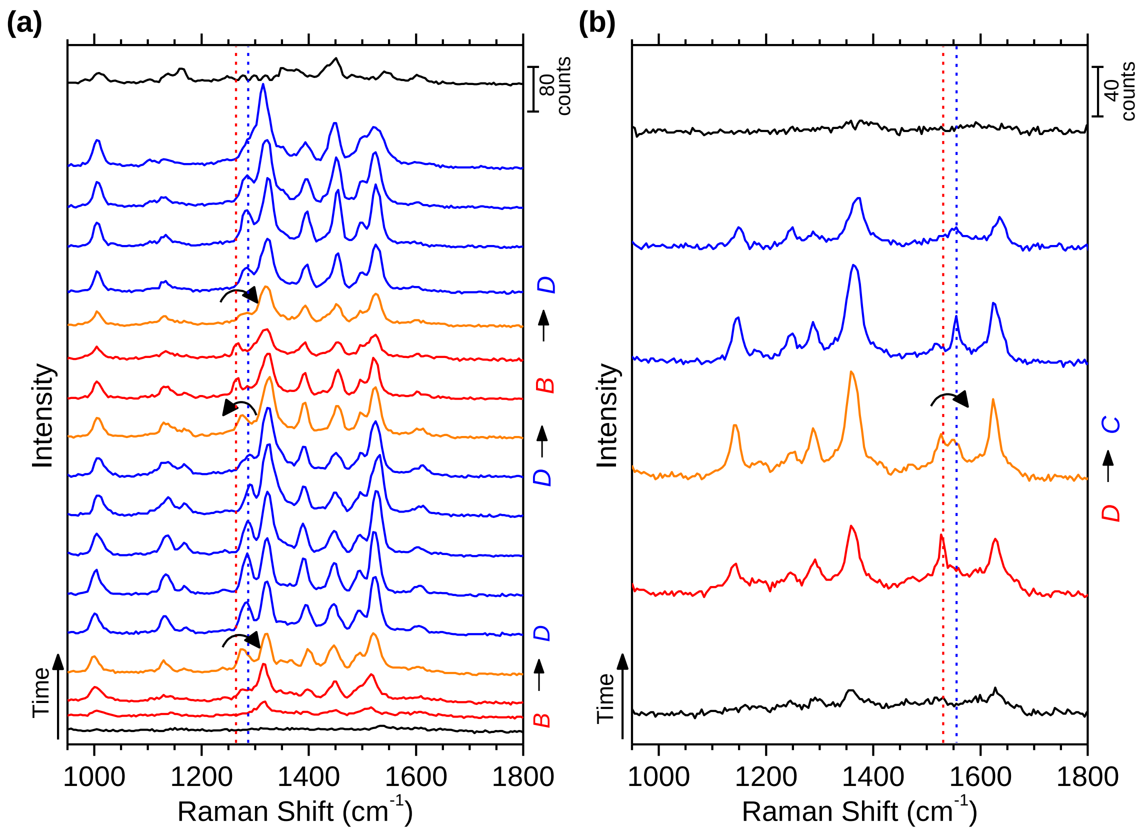

Figure 3.8. SM jumps capturing conformational transitions of the wt-GFP chromophore at 100 ms intervals and laser power of 100 µW: **(a)** repeated switching steps between *cis* and non-planar forms of deprotonated chromophore; **(b)** protonation at non-planar form. The vertical lines indicate the marker peaks for protonated, deprotonated, *cis*, and non-planar conformations, 1565, 1536, 1270, and 1287cm^{-1}, respectively. Red and blue plot lines distinguish two different conformations. Orange plot lines and arrows indicate transitions.

3.3.5. Multi-Analyte Approach

A common and most reliable method used to validate the single molecule nature of the captured signal is the bi-analyte method. The bi-analyte method consists of measuring the SERS signal from a mixture of two analytes of low concentration, which have distinguishable SERS signals and comparable SERS cross-sections under the same measurement conditions [127, 145, 152, 153]. Rare detection of both analytes simultaneously is considered as a direct proof of capturing SMs.

In the present study, instead of using two analytes, conformers of the same analyte with distinct SERS signatures captured on Ag NPs (i.e., GFP and AB) were realized for "multi-analyte" verification of SM detection. For example, a single AB molecule is captured in 6 states, i.e., *trans* and *cis* conformers, each at 3 distinct adsorption configurations, as discussed in *Chapter IV*. Similarly, wt-GFP molecule is captured in 4 different states with distinct vibrational markers; *cis*/protonated (A), *cis*/deprotonated (B), nonplanar/protonated (C), and nonplanar/deprotonated (D) states (Figure 3.9). Detecting different states of AB or wt-GFP exclusively during intervals with no-transition provides the multi-analyte verification of SM detection. Occasionally, markers of 2 different states are detected during a transition, which only lasts for one or two time interval (40 ms and 100 ms for AB and wt-GFP, respectively) as demonstrated in Figures 3.7 and 3.8 during the transitions of AB and wt-GFP, respectively (orange spectra). This is due to the existence of a molecule in two different conformer for the duration of the time interval used rather than the detection of multiple molecules.

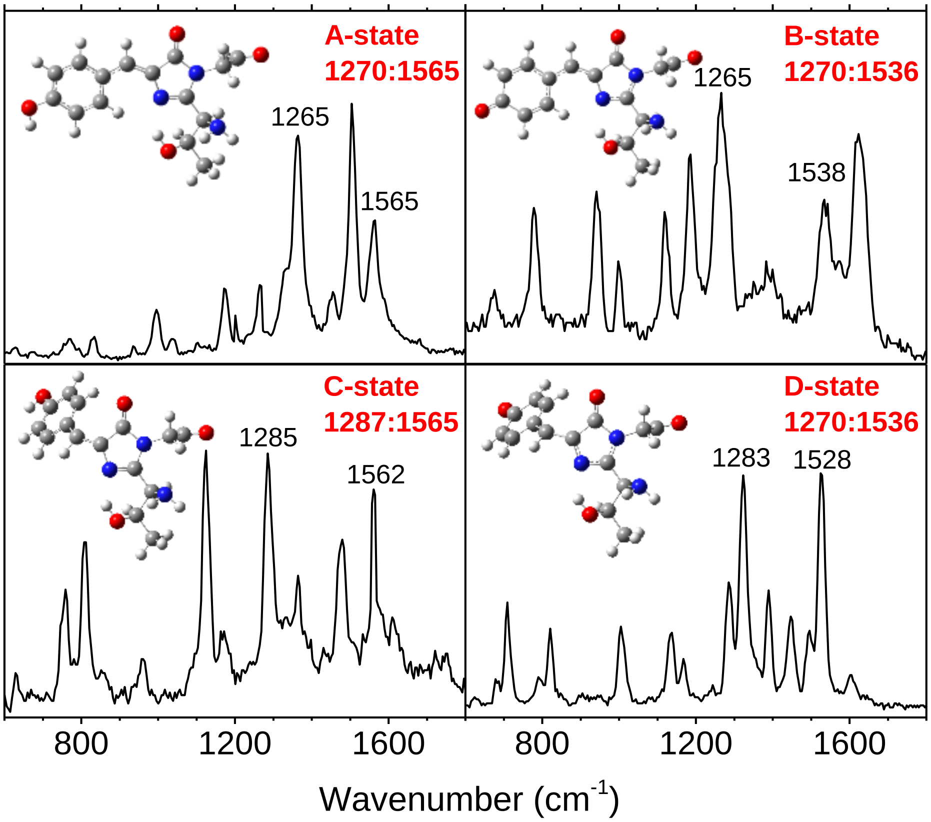

Figure 3.9. SM-SERS spectra of wtGFP, representative of different chromophore conformational states: *cis*/protonated (A); *cis*/deprotonated (B); nonplanar/protonated (C); nonplanar/deprotonated (D). Ball-stick models of the chromophore are also provided (grey: C; white: H; red: O; blue: N).

3.3.6. Flashes of Raman Scattering

The last evidence of capturing SMs using Ag NHS-on-Ge substrates is based on the imaging of Raman flashes in the laser-illuminated spot demonstrated for wt-GFP as shown in Figure 3.10. The flashes last for a fraction of a second to several seconds reminiscent of the SM spectral jumps. While no such flashes are observed for pure water, they occur more frequently when the GFP concentration is increased five times. Therefore, the observed flashes are attributed to the Raman images of single GFP molecules whose resolution is limited by diffraction as well as CCD image pixel size.

The Raman flashes in a laser (532 nm, 6 mW) spot of 15 µm were recorded using a 20X objective lens (NA: 0.4). 15.1 µm × 15.1 µm successive video frames (25 fps) of the laser spot were analyzed for a total time span of 12 s, but trimmed into 11 tracks (a total of 117 frames) capturing the SM activity. A weak background signal can be observed in all the frames. This is attributed to ensemble-averaged signal coming from the sites with low SERS enhancement factor, as well as the Rayleigh scattering leaking from the laser filter. The specific pixels where the flashes occur are represented with letters (i.e., A, B, C, …) while the flashes occurring at the same pixel were counted by numbers (i.e., A1, A2, A3, …).

The first flash starting in frame 21 and labeled as A1, lasts for about 0.8 s. Later, 5 additional flashes are recorded at the same pixel, A, which are labeled as A2 to A6. Flash B2 lasts for an outstandingly long duration of 7.4 s, during which other flashes are recorded at pixels A, C and D. Flashes B1 and B2 turn on with a gradual intensity increase, while A1 turns off with a gradual decrease resembling the gradual intensity changes which are attributed to the surface diffusion of the molecule in and out of a hotspot. In addition, intensity fluctuations can also be observed in some of the flashes (e.g., A1 and B2). To exemplify intensity fluctuations of the flashes, frames 95-99 show magnified images of flash-B2. These fluctuations in the intensity of the captured Raman flashes resembles the overall intensity fluctuations observed in SM-SERS spectra as discussed in *Section 3.3.3.* Interestingly, the flashes are observed to occur repeatedly at certain pixels. Hence, hotspots yielding detectable SM signals are inferred to be specific sites.

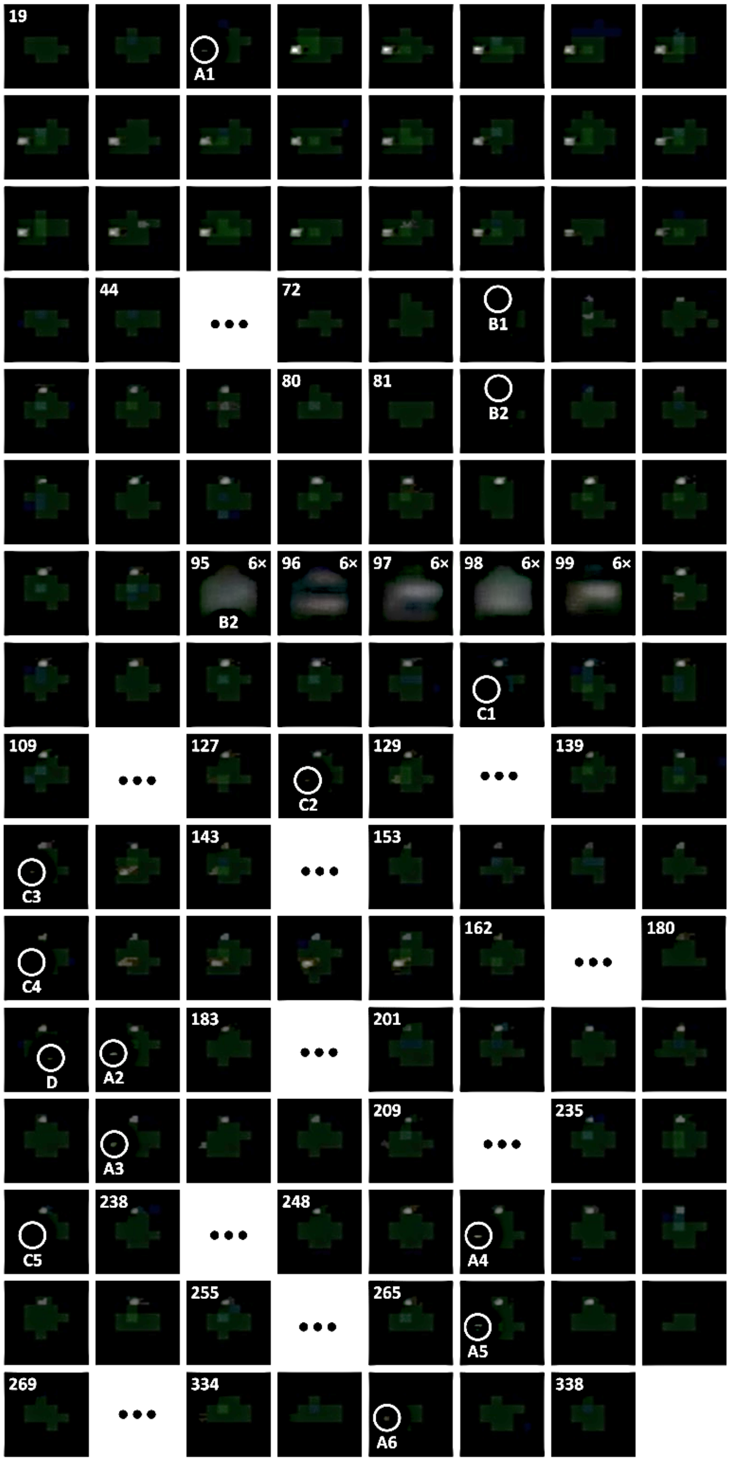

Figure 3.10. Flashes of Raman scattering from single GFP molecules**.** The CCD image pixel size is 0.5 µm. The frame numbers are given at the top-left corners to indicate the start and end of each sequence capturing a flash. The track for flash-B2 is shown in parts due to its long duration (frames 82-267).

3.4. Conclusions

The present study demonstrates the detection of single wt-GFP and AB on Ag-nanohemispheres-on-Ge-nanoposts substrates, whose unique plasmonic properties were investigated in *Chapter II*.

During the time-series SERS measurements of both analytes, we observe sudden appearance of Raman peaks (i.e., SM jumps) which are attributed to surface diffusion of a SM in and out of a hotspot, i.e., regions at NHS junctions with highly localized electromagnetic fields capable of producing detectible SM signals. Analysis of the observed SM jumps reveal intensity and frequency fluctuations which are attributed to statistical variations in the adsorption configuration due to surface diffusion, and supports the SM origin of the observed SERS jump, both for AB and wt-GFP.

The high time resolutions used in the present study (i.e., 40-100 ms) allows us to resolve dynamic events such as surface diffusion of single AB and wt-GFP molecules in and out of a hotspot, conformational transitions in wt-GFP and AB, and protonation/deprotonation events in wt-GFP. Such events can only be resolved at SM level, without the statistical averaging of ensemble-averaged studies, and hence constitutes a strong evidence for SM detection.

We also observe overall intensity fluctuations which indicate variations in both electrochemical and chemical enhancements experienced by the molecules during their visit to the hotspots. The observed selective frequency shifts coupled with the overall intensity fluctuations in SERS peaks of an AB molecule indicates a molecule-substrate charge transfer reaction. Further, they point to the desorption–re-adsorption nature of the surface diffusion of AB on Ag surface, which presents a concrete proof of SM detection in the present study.

Further, we use one of the well-established SM verification technique, i.e., bi-analyte, to further support the SM origin of the observed SERS signals of AB and wt-GFP. However, instead of using two analytes, as done in the bi-analyte technique, conformers of the same analyte (i.e., GFP and AB) with distinct SERS signatures captured on Ag NPs are realized for “multi-analyte” verification of SM detection in the present study.

Another technique we put forward as an evidence for SM detection is the imaging of the Raman flashes (i.e., Raman scattered light) of SMs, where Raman flashes in the illuminated spot during time-series SERS acquisition of wt-GFP are recorded. The analysis of the Raman flashes reveal similar intensity fluctuations observed in SM-SERS spectra. In addition, the flashes are observed to occur repeatedly at certain pixels. Hence, hotspots yielding detectable SM signals are inferred to be specific sites. Accordingly, the observed flashes are attributed to the Raman images of single wt-GFP molecules whose resolution is limited by diffraction as well as CCD image pixel size.

CHAPTER IV

SINGLE AZOBENZENE ADSORBATES ON NANO SILVER FACETS STUDIED BY SERS

4.1. Introduction

The surfaces of plasmonic NPs enabling SERS consist of facets of different crystal orientations, and defect sites (i.e., kinks, steps, and corners) [134, 164-166]. While this surface heterogeneity provides a rich platform to study physical and chemical events in molecules by SERS, it also complicates the interpretation of the observed trends in ensemble-averaged (EA) measurements. Recent SM-SERS and computational works by Van Duyne Lab suggested that the surface heterogeneities of NPs are the source of under-potential events observed in the reduction of single rhodamine 6G (R6G) molecules on Ag NPs [134, 140]. The present work unravels the differentiating effect of different surface crystal orientations in Ag NPs on the adsorption configuration of SMs, as distinguished from their distinct SERS spectra. We resolve six distinct adsorbate states of single azobenzene (AB) molecules on Ag NPs by SERS. By the help of DFT calculations, these six different AB adsorbates are associated with three different crystal orientations of the Ag surface and two different isomers of AB (i.e., *trans* and *cis*). Previous studies have already investigated the impact of surface crystal orientation on adsorption configuration and associated SERS spectrum of various molecules. Though, none of these studies have resolved such differences at the SM level [167-170].

While the present work underscores the potential of SM-SERS in resolving different adsorbate states due to NP surface heterogeneities, it also demonstrates a powerful tool to study the nature of the AB–metal interactions. AB is one of the most extensively studied photochromic molecules owing to its chemical simplicity, and its efficient and reversible photoswitching between a planar *trans* form (*t*-AB) and a non-planar *cis* form (*c*-AB) [18-22]. In recent years, there has been a growing interest in using AB as the active component of molecular devices which require its immobilization on solid surfaces. Although immobilization might be necessary for the localization and ordering of the molecules on surfaces, especially in solid state applications, it may also induce changes in the switching properties of AB due to structural and electronic interactions with the substrate. As discussed in *Chapter I*, an immense amount of research showed that photoswitching of AB on solid surfaces is completely lost. This emphasized the need for a better understanding of these interactions for the design of future molecular devices. In this manner, SM-SERS can be a powerful tool by providing direct information (through molecular vibrations) on conformational modifications induced by interaction of single molecules with their environment (e.g., bonding or charge transfer). SERS inherently involves the adsorption of molecules onto metal NPs (i.e., Ag), which provide a rich platform due to their multifaceted nature. The present SM-SERS study, with the help of DFT calculations, provides direct information about the conformation and the surface interaction of AB adsorbates on three distinct crystal facets of Ag (i.e., (111), (100), and (110)). Further, we demonstrate the reversible switching between three distinct adsorbates of *trans* and *cis* conformers of AB.

4.2. Methods

4.2.1. SERS Acquisitions

Azobenzene was purchased from Sigma Aldrich. A saturated solution of azobenzene ($\approx 1\times10^{-7}$ M) was prepared in de-ionized (DI) water and stored in the dark at room temperature. In a typical SERS acquisition, a 1.5 µL aliquot of 1×10^{-8} M azobenzene/water solution was spotted on a substrate. In order to prevent the aliquot from drying during acquisition, the substrate was sealed inside an optical cell (Starna Cell; $12.5\times3.5\times45.0$ mm^3) along with a small piece of wet tissue.

SM-SERS and EA-SERS spectra were collected using a WITec Alpha300M Raman Microscope with a 600 g/mm grating. A 532 nm Nd:YAG (neodymium-doped yttrium aluminium garnet; Nd:Y3Al5O12) laser was employed as the excitation source. The laser was focused on the aliquot-substrate interface (i.e., Ag nanoparticles) using a 20X objective lens with a numerical aperture of 0.4. A laser spot size of 2 µm and 650 µW incident power was used for SM-SERS acquisitions. Time-series SM–SERS spectra was collected using 650 µW incident laser power at 40 ms intervals. EA-SERS acquisitions were performed using 3 mW incident laser power and 30 µm spot size. The integration time for EA-SERS acquisitions were 200 s.

4.2.2. Computational Details

i.) DFT Calculation with ABINIT

All DFT calculations with ABINIT were performed using Perdew-Burke-Ernzerhof (PBE) [171] generalized gradient approximation (GGA) together with Grimme's D3 dispersion correction [172]. Pseudopotential plane-wave (PAW) method [173] as implemented in ABINIT was used with ultrasoft pseudopotentials [174]. The planewave and the PAW cutoff were kept at

13 Ha (350 eV) and 30 Ha (816 eV), respectively. For the calculation of bulk lattice constant of the Brillouin Zone was sampled using a 4x4x1 Monkhorst-Pack grid [175] and 4 shifted k-point grids. The Ag lattice constant was calculated to be 4.096 Å which is close to the experimental lattice constant of 4.086 Å.

All surfaces were modeled with a periodic slab of 3 atomic layers of Ag with 15 Å vacuum in the z-direction. In order to fit the AB molecule and also prevent any interaction with its periodic images, (7x3), (4x3) and (6x3) supercells were used for Ag (111), Ag (100) and Ag (110) surfaces, respectively, as seen in Figure 4.1. The adsorbate and the top layer of the slab were relaxed until the maximum force on the atoms was lower than $5.0\text{x}10^{-5}$ Ha/Bohr (2.6 meV/ Å). The bottom two layers were kept frozen. The Brillouin Zone was sampled using a 2x4x1 Monkhorst-Pack grid and 4 shifted k-point grids. Structural optimization was conducted using the Broyden-Fletcher-Goldfarb-Shanno minimization (BFGS) where the tolerance on the maximum force was $5.0\text{x}10^{-4}$ Ha/Bohr (26 meV/ Å).

The adsorption energy (E_{Ads}) was defined as

$$E_{Ads} = \left[E_{AB@Ag} - E_{Ag}\right] - E_{AB(isolated)} \qquad (5)$$

where, $E_{AB@Ag}$ is the total energy of AB (i.e., *t*-AB and *c*-AB) on Ag surface (i.e., Ag (111), Ag (100) and Ag (110)), E_{Ag} is the total energy of the Ag surface without AB, and E_{AB} is the total energy of the isolated AB.

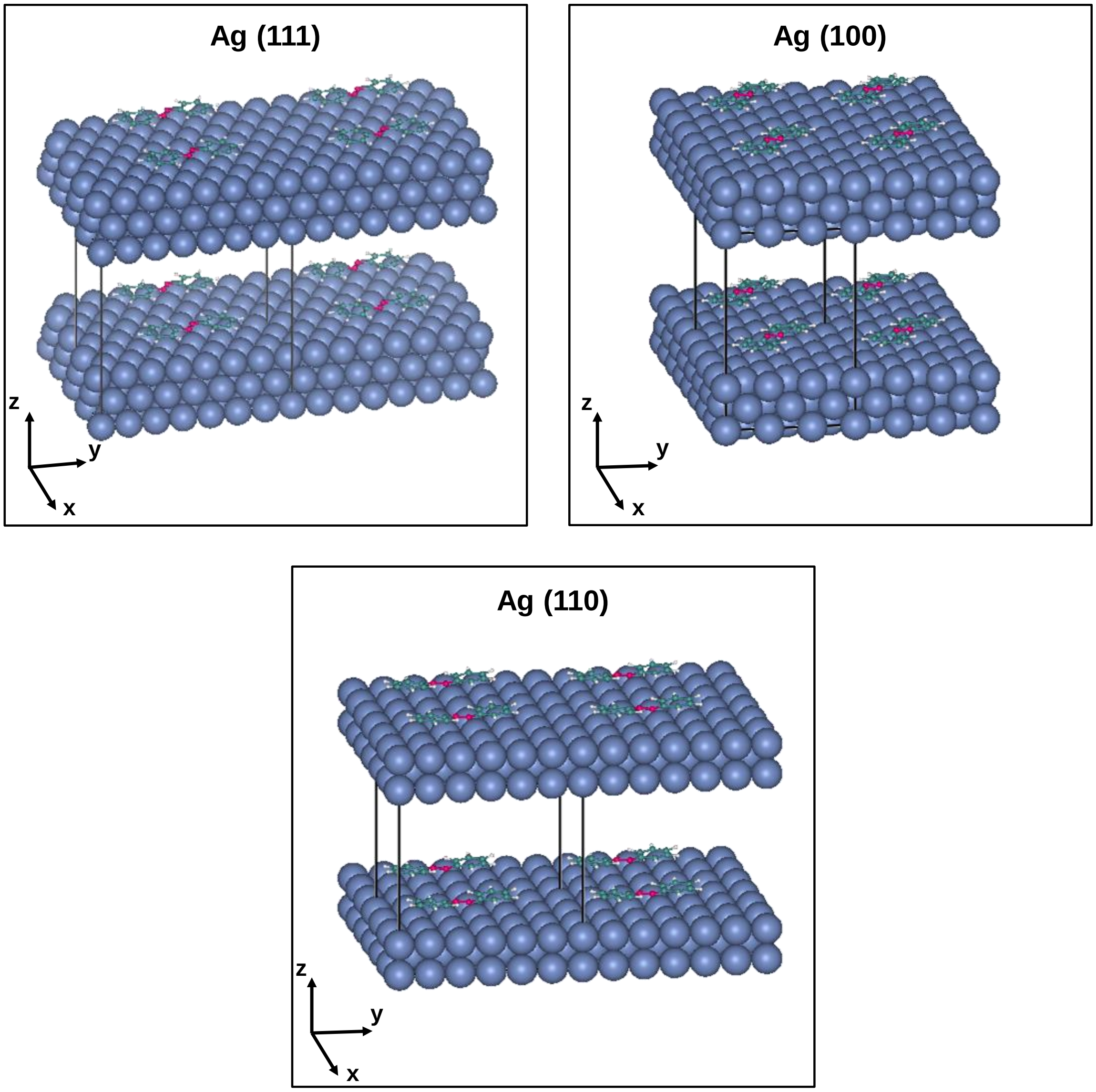

Figure 4.1. 2×2×2 supercells of three-layer Ag(111), Ag(100), and Ag(110) slabs showing the surface adsorbed AB molecules (Ag: grey, C: green, N: magenta, H: white).

ii.) DFT Calculations with Gaussian 09

The optimized structures of isolated *t*-AB and *c*-AB and the Raman spectra of isolated and adsorbed *t*-AB and *c*-AB were calculated with Gaussian 09 software using GGA-PBE 6-31G(d) basis set was used for the H, C and N atoms. No corrections were performed on the calculated spectra.

4.3. Results and Discussion

4.3.1. Vibrational markers of *trans* and *cis* azobenzene on Ag nanoparticles studied by Ensemble-averaged SERS

Before discussing the SM-SERS spectra of AB, *trans* and *cis* vibrational markers on Ag NPs will be established by studying the EA-SERS spectrum of AB kept in dark and under UV irradiation. As-prepared AB solution consists of a mixture of *t*-AB and *c*-AB. As elaborated by the absorption spectrum given in Figure 4.1, the majority of the molecules are in *trans* confirmation. Upon excitation of AB through π-π* ($S_2 \leftarrow S_1$) transition with UV light (Blak-Ray long-wave UV lamp at 365 nm), the absorption maximum shifted from 318 nm to 292 nm indicating that the majority of the population is now in *cis* confirmation.

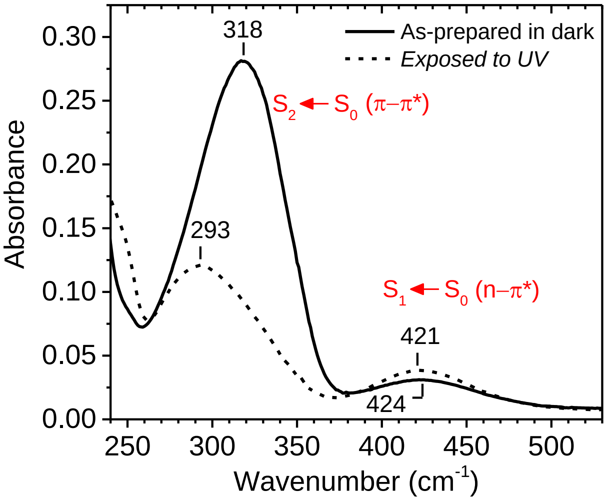

Figure 4.2. Absorption spectrum of 10^{-7} M AB in water: as prepared in dark (solid) and exposed to UV illumination (dashed).

Figures 4.3a-f show the EA-SERS spectra of AB. To resolve the Raman peaks, the spectra was fitted to Gaussians using MagicPlot software. While the SERS spectrum of as prepared AB (kept in dark) in Figures 4.2a-b shows similarities to the Raman spectrum of AB [176-179], significant differences are observed in the 1200−1300 cm^{-1} and 1600−1700 cm^{-1} region. When AB solution is exposed to UV irradiation prior to the SERS acquisitions, changes in the relative intensities of certain peaks were observed in the spectra as seen in Figures 4.3c-d. To confirm if similar changes in the EA-SERS spectra occur when AB is excited on Ag NP surface, the aliquot-substrate interface was illuminated with a 365 nm LED light (7mW focused to spot size of 1 mm) during acquisitions. As seen in Figure 4.3e-f, changes in spectra similar to those in Figure 4.3c-d are observed. The observed changes in the EA-SERS spectra in Figure 4.3c-f are attributed to the transformation of *t*-AB to *c*-AB on Ag NP surface. The observation of similar changes for AB adsorbed on Ag NPs (Figure 4.3e-f) indicates that *trans→cis* switching of AB is achievable on the surface of the Ag NPs. The changes in spectra in Figure 4.3e-f were observed to be more pronounce due to higher number of molecules transforming from *t*-AB to *c*-AB. Thus, *t*-AB and *c*-AB SERS markers were studied by comparing the spectra in Figure 4.3a-b and Figure 4.3e-f. To distinguish the markers clearly, a difference spectra was created (Figure 4.3g) by subtracting the spectrum in Figure 4.3e-f from the spectrum in Figure 4.3a-b where the positive and negative peaks represent the *trans* and *cis* markers, respectively. A detailed inspection of spectra in Figure 4.3 indicates that some of the marker peaks obtained in Figure 4.3g are not exclusive to either *trans* or *cis*. For example, although a decrease in the relative intensities of peaks at 807, 1304, 1392 and 1442 cm^{-1} are observed upon UV irradiation, these modes are prominent in Figure 4.3e and Figure 4.3.g as well. While the observed markers are useful for identifying the *trans* and *cis* conformers, they will be used with a great precaution in our SM-SERS study as they may not necessarily be exclusive SM markers.

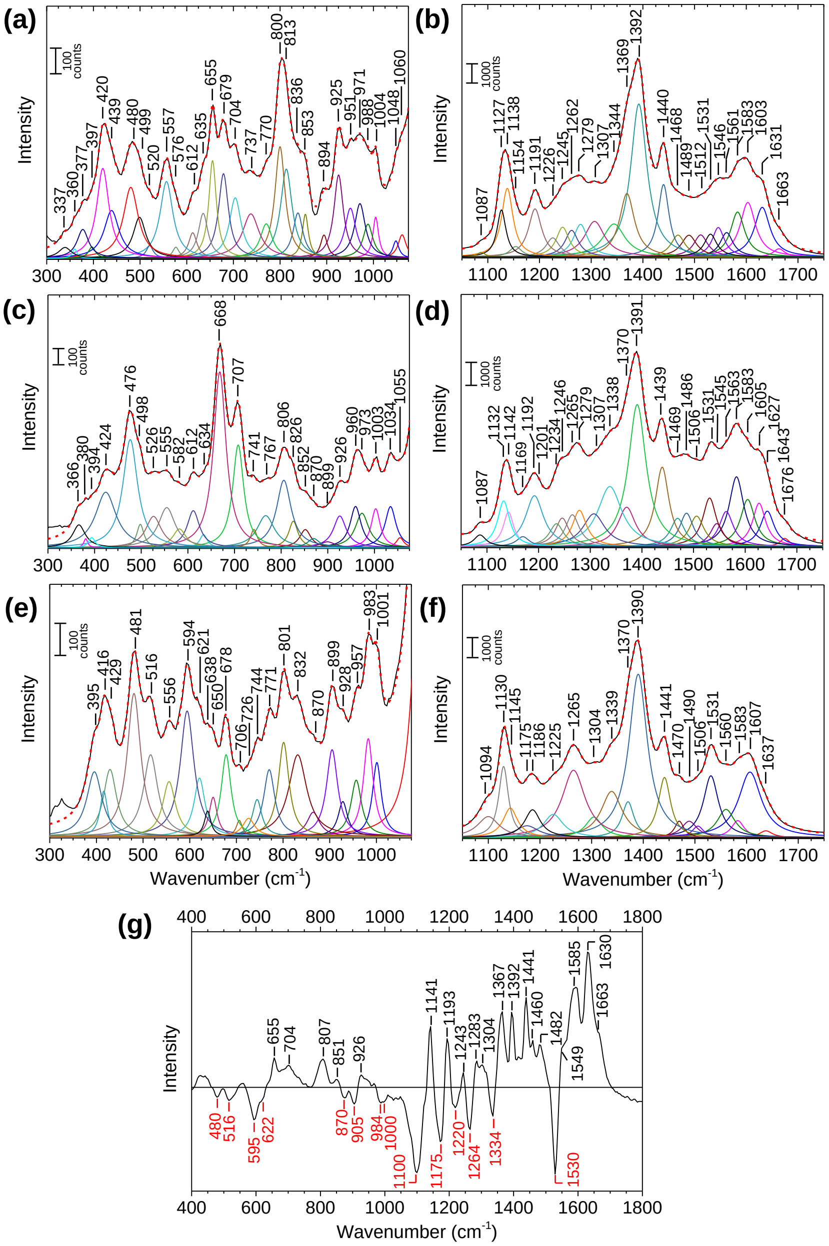

Figure 4.3. EA-SERS spectrum of azobenzene: **(a-b)** as prepared, **(c-d)** exposed to UV illumination and **(e-f)** under in-situ UV illumination. Black solid line: experimental spectrum; red dashed line: fitted spectrum. **(g)** Difference spectrum of (a-b) and (e-f). Marker peaks for *trans* and *cis* are in black and red color, respectively.

4.3.2. SERS Spectra of Single *Trans*- and *Cis*-Azobenzene on Ag Nanoparticles

Analysis of 270 SM-SERS data of AB revealed 6 distinct jumps. A representative spectrum of each jump is given in Figure 4.4. Additional jumps were provided in Appendices. The SM nature of the observed SERS spectra was validated in *Chapter III*. The SM jumps in Figures 4.4a-c were observed to occur more frequently for AB solution kept in dark (i.e., high *trans* population) while the jumps in Figures 4.4d-f occurred more frequently when AB was exposed to UV light prior to SERS acquisitions (i.e., high *cis* population). Indeed, the SERS markers deduced from EA-SERS in Figure 4.3 also suggests that the jumps in Figures 4.4a-c are associated with *trans* conformer while the jumps in Figure 4.4d-f are associated with *cis* conformers of AB. Accordingly, the jumps in Figures 4.4a-c and Figure 4.4d-f are attributed to distinct adsorbate states of *t*-AB and c-AB on Ag NPs, respectively. In the remaining of this work, the adsorption configurations associated with the SM jumps in Figure 4.4a-f will be referred as *t*-AB1, *t*-AB2, *t*-AB3, as *c*-AB1, *c*-AB2, and *c*-AB3, respectively. As observed in the additional SM-SERS jumps given in Appendices (Figure A1-36), variations (i.e., peak positions and relative intensities) are observed within the jumps associated with the same adsorbates. This is attributed to slight variations in the local geometric and electronic structure of the associated surfaces as well as to variations in the local electromagnetic field experienced by the molecules. Observation of such variations is in accordance with the SM nature of the observed spectra. In fact, ability to resolve such variations is a strong evidence of SM-SERS as discussed in *Chapter III*.

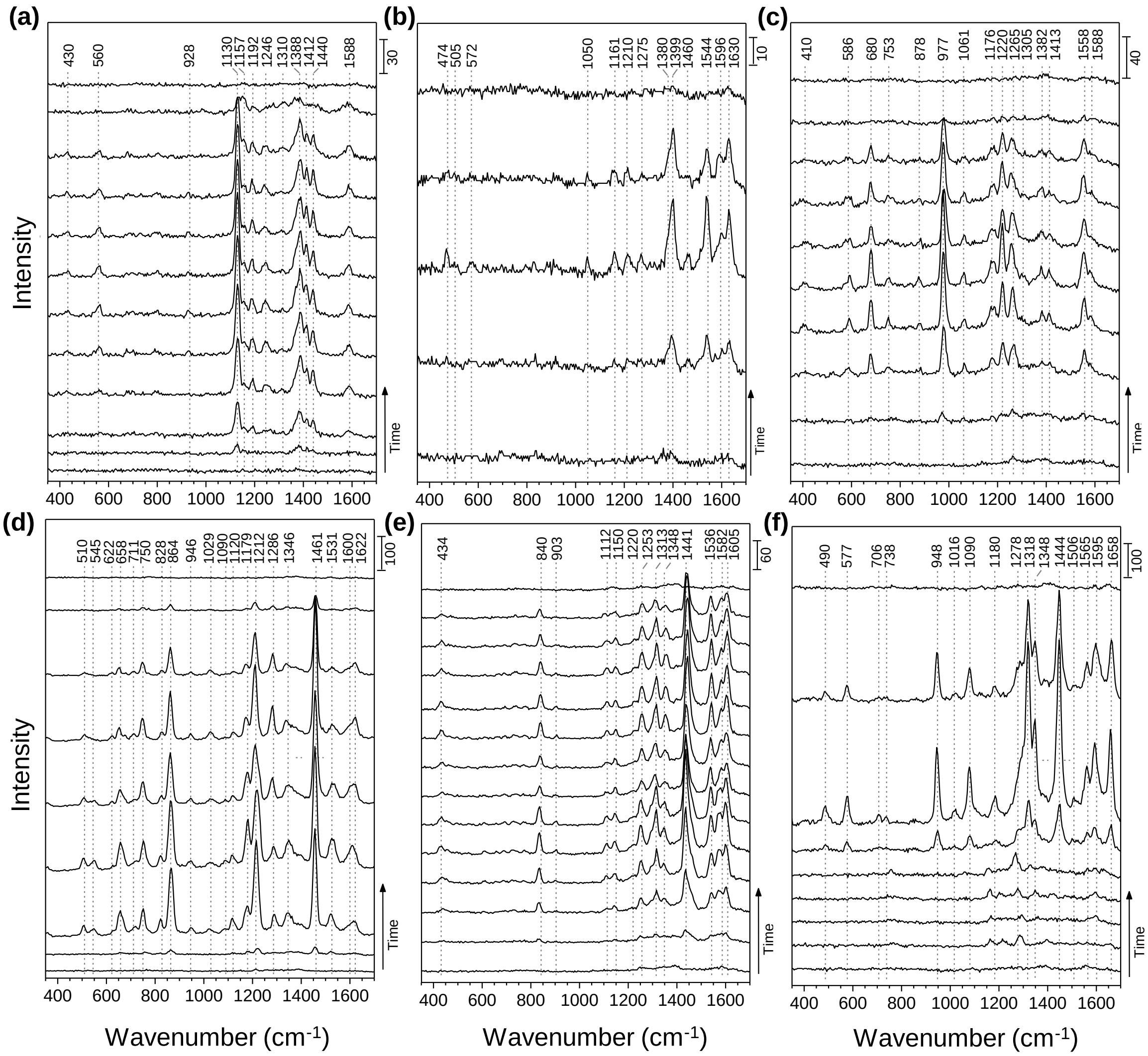

Figure 4.4. Time-series spectra representing characteristic SERS jumps of single AB molecules captured at 40 ms intervals. Jumps in **(a-c)** and **(d-f)** are associated with *trans* and *cis* conformers of AB, respectively. Scale bars show the CCD counts.

Adsorption of AB to a metal surface is determined by an interplay of four major factors: i) coordinative bond between the azo-bridge (N=N) and the metal, ii) the van der Walls (vdW) attraction and iii) the Pauli repulsion between the phenyl rings and the metal substrate, and iv) the energetic penalty due to the distortion of the gas phase molecular geometry. In *t*-AB, while the Ag–N bonding pulls the molecule close to the substrate, the repulsive Pauli interaction pushes the rings away from the surface, resulting in the distortion of the planar geometry. However, the vdW attraction between the rings and the metal substrate can compensate for this repulsive interaction, pulling the rings and the whole molecule towards the surface. On the other hand, for *c*-AB, the interaction with the substrate is dominated by the Ag–N coordinative bonding in an adsorption configuration where one or both of the phenyl rings are pointing upwards from the surface.

Regardless of AB being *trans* or *cis*, the resulting adsorption geometry is determined by the reactivity of the surface, which is related to both surface geometric and electronic structure. Because the atoms in the surface of a crystal have less neighbours (i.e., coordination) than they would in the bulk, the surface energy levels and the surface electronic band structure are inferred to be different than those in bulk. The surface energy of a metal is proportional to the number of broken bonds, or coordination; lower the coordination of the surface, higher the surface energy. It was shown by Galanakis et al. for several fcc metals, including Ag, that there is a linear relationship between the relative surface energy and the coordination number of the surface atoms [180, 181]. Thus, for the low-index facets of Ag NPs, the surface energy (γ) is expected to be in the following order: $\gamma_{(111)} < \gamma_{(100)} < \gamma_{(110)}$.

Further, on surfaces having atoms with valence states consisting of localized orbitals (i.e., d valence orbitals in transition metals), the average width of the partial density of states (PDOS) is reduced relative to the bulk state [182]. This “band narrowing” results in an energy shift of the narrowed band which can be approximated using the rectangular box model as,

$$\Delta s = E_f\left(1 - \sqrt{\frac{C_{surface}}{C_{bulk}}}\right) \tag{6}$$

where, $C_{surface}$ and C_{bulk} are the coordination number of the surface and the bulk, respectively, and E_f is the Fermi energy. As *Equation 6* indicates, with decreasing surface coordination number ($C_{surface}$), the change in the band energy (Δs) increases. Thus, the surface electronic structure is expected to be different for facets with different crystal orientations.

To demonstrate the effect of crystal orientation on the adsorption configuration of AB, and to validate the proposed hypothesis that, the three distinctly-observed adsorbates of each AB isomer originates from three different crystal facets available for adsorption, DFT calculations were performed. Using ABINIT software, *t*-AB and *c*-AB were optimized on low-index Ag surfaces of (111), (100), and (110). Indeed, these crystal facets frequently reported in the Ag NP literature [164-166]. To account for the dispersive interactions (e.g., Van der Waals forces), Grimme's DFT-D3 dispersion correction method were included in the calculations. The Raman spectra of optimized *t*-AB and *c*-AB in isolated and adsorbed states were calculated using Gaussian 09.

Before discussing the surface-adsorbed structures of AB, the optimized structures and the corresponding vibrational spectra of isolated (non-surface-adsorbed) *t*-AB and *c*-AB will be established in the next section. Further, the computational results will be compared to the experimental ones to validate the accuracy of GGA-PBE method for AB.

4.3.3. Structure and Vibrational Spectra of Isolated Azobenzene

Figure 4.5 shows the optimized structures of *t*-AB and *c*-AB. As seen in Table 4.1, calculated values of N═N and C─C bond lengths ($d_{N═N}$ and $d_{C─C}$, respectively), CNNC dihedral angle (∠CNNC), NNCC dihedral angle (∠NNCC), and CNN bond angle (∠CNN) have a good agreement with the experimentally found values [183, 184]. Further, the calculated structural parameters also match well to those calculated in the literature using various DFT functionals, including PBE [185, 186]. As also given in Table 4.1, *t*-AB is found to be 0.52 eV more stable than *c*-AB which is slightly lower than the experimental value of 0.6 eV [35]. As our calculations demonstrate and the above-cited literature supports, the GGA-PBE method can calculate the free *t*-AB and *c*-AB structures accurately.

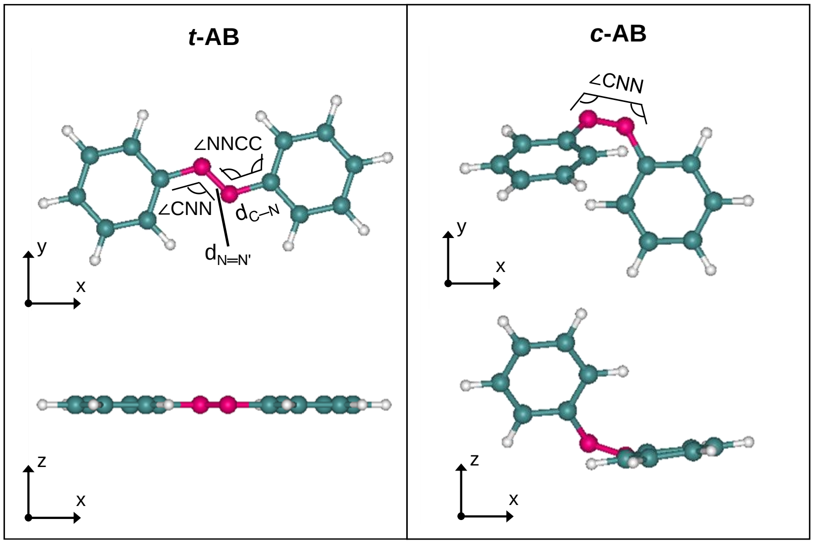

Figure 4.5. Ball-stick models showing *t*-AB and *c*-AB in xy and xz planes. N═N and C─C bond lengths $d_{N=N'}$ and $d_{C–N}$, CNNC dihedral angle ∠CNNC, NNCC dihedral angle ∠NNCC, and CNN bond angle ∠CNN are marked. White: H, green: C, magenta: N. Atoms and parameters belonging to the right side relative the azo-bridge are denoted with ' symbol.

Table 4.1. Calculated and experimental structural parameters of *t*-AB and *c*-AB and total energy difference between the isomers ($\Delta E_{c\text{-}t}$) at ground state. Parameters are defined in Figure 4.5.

	t-AB		*c*-AB	
	GGA-PBE	Exp. [183, 184]	GGA-BPE	Exp. [184]
$d_{N–N}$ (Å)	1.28	1.25	1.26	1.25
$d_{C–N}$ (Å)	1.42	1.43	1.44	1.45
∠CNNC (°)	180	180	12	8
∠NNCC (°)	0	7	48	53
∠CNN(°)	114	115	123	122
	GGA-BPE		Exp.[35]	
$\Delta E_{c\text{-}t}$	0.52		0.6	

The calculated vibrational spectra of optimized *t*-AB and *c*-AB structures in Figure 4.5 are given in Figure 4.6. Assignments of the vibrational modes are given in Table 4.2. A close agreement is found between the calculated and the experimental data both for *t*-AB and *c*-AB (Table 4.2). The N═N stretching for *t*-AB is calculated at 1426 cm^{-1}, showing a slight downward shift compared to the experimentally observed frequency at ≈1440 cm^{-1}. On the other hand, the calculated frequency of N═N stretching at 1517 $cm^{-1}$for *c*-AB matches to the experimentally observed frequency at ≈1520 cm^{-1}. Another characteristic mode both for *t*-AB and c-AB is the C─N stretching which is calculated at 1133 cm^{-1} and 1119 cm^{-1}, respectively. Further, the modes observed in 1450-1490 cm^{-1} and 1585-1610 cm^{-1} region are assigned to semicircular and the quadrant stretching vibrations of the rings, respectively. The N═N torsion of *c*-AB, which is one of the frequently used Raman markers of *c*-AB, is calculated at 586 cm^{-1}, and it is not Raman active for *t*-AB.

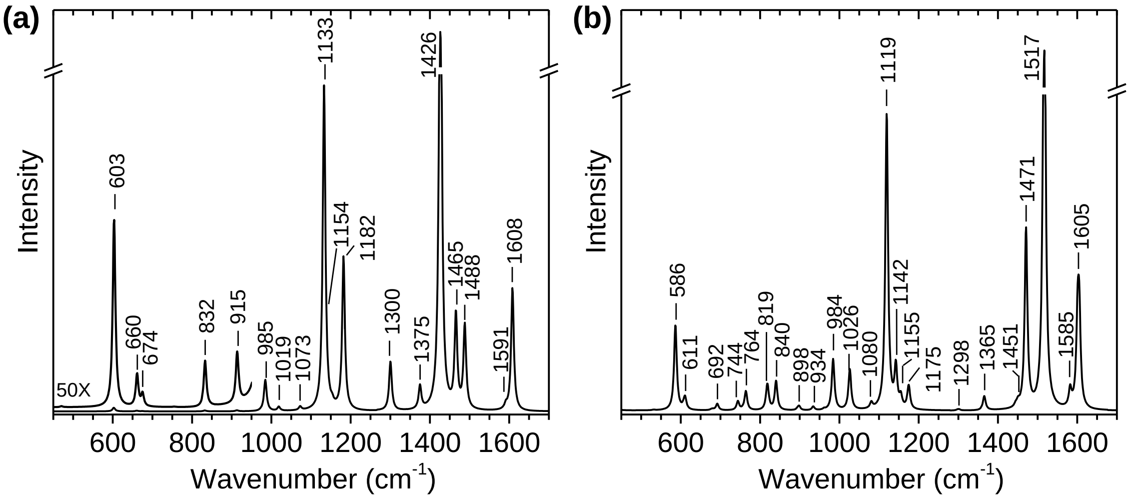

Figure 4.6. Calculated Raman spectrum of optimized structures in Figure 4.5: *t*-AB **(a)**; *c*-AB **(b)**.

Table 4.2. Calculated and experimentally observed frequencies (in cm^{-1}) of *t*-AB and *c*-AB obtained using BPE/6-31G functional.

***t*-AB**			***c*-AB**		
Calc.	Exp. [183, 184]	Assignment	Calc.	Exp. [184]	Assignment
1608		υ(C–C), δ(C–C)	1605		υ(C–C), δ(C–H)
1591	1595	υ(C–C), δ(C–N)	1585	1585	υ(C–C), δ(C–H)
1482	1493	υ(C–C)	1517	1511	υ(N=N)
1465	1473	υ(C–C), υ(N=N)	1471		δ(C–H), υ(C–C)
1426	1443	υ(N=N)	1451	1451	δ(C–H), υ(C–C)
1375	1379	υ(C–C), δ(C–N)	1365		υ(C–C) δ(C–H)
1300	1315	δ(C–H), δ(C–N)	1298	1309	δ(C–H)
1182	1184	υ(C–C), υ(C–N)	1175	1178	δ(C–H), υ(C–C)
1154	1158	δ(C–H)	1155	1152	δ(C–H), υ(C–C)
1133	1146	υ(C–N), υ(C–C)	1142		υ(C–N)$_{asymm}$
1073	1071	υ(C–C), δ(C–C)	1119		υ(C–N), υ(C–C)
1019	1023	υ(C–C), δ(C–C)	1080	1067	υ(C–C), δ(C–H)
985		δ(C–C), υ(C–C)	1026	1023	υ(C–C), δ(C–H)
915	913	δ(N=N), δ(C–C)	984	988	δ(C–C), υ(C–C)
832	836	γ(C–H)	934	968	γ(C–H)
754	755	γ(C–H), τ(C–C)	898		γ(C–H)
674		γ(C–H), τ(C–C)	840	834	γ(C–H), δ(N=N)
660	670	δ(C–C), δ(C–N)	819	807	γ(C–H)
603	614	δ(C–C)	764	756	γ(C–H), υ(C–N)
			744		γ(C–H), δ(C–C)
			692	688	γ(C–H), δ(N=N)
			586	596	τ(N=N)
			531	541	δ(C–N), δ(C–C)

υ; stretch, δ; in-plain bend, γ; out-of-plain bend, and τ; torsion.

4.3.4. Adsorption of Azobenzene on Ag Facets

In this section, adsorption of *t*-AB and *c*-AB on Ag facets will be discussed in the light of SM-SERS spectra and the DFT calculations. In the remaining of this dissertation, the adsorbates on Ag (111), Ag (100) and Ag (110) are referred as *t*-AB$_{\mathrm{Ag(111)}}$, *t*-AB$_{\mathrm{Ag(100)}}$, *t*-AB$_{\mathrm{Ag(110)}}$ for *t*-AB, respectively, and as *c*-AB$_{\mathrm{Ag(111)}}$, *c*-AB$_{\mathrm{Ag(100)}}$, *c*-AB$_{\mathrm{Ag(110)}}$ for *c*-AB, respectively. The important parameters used for describing the adsorbate geometries are defined in Figures 4.5 and 4.7.

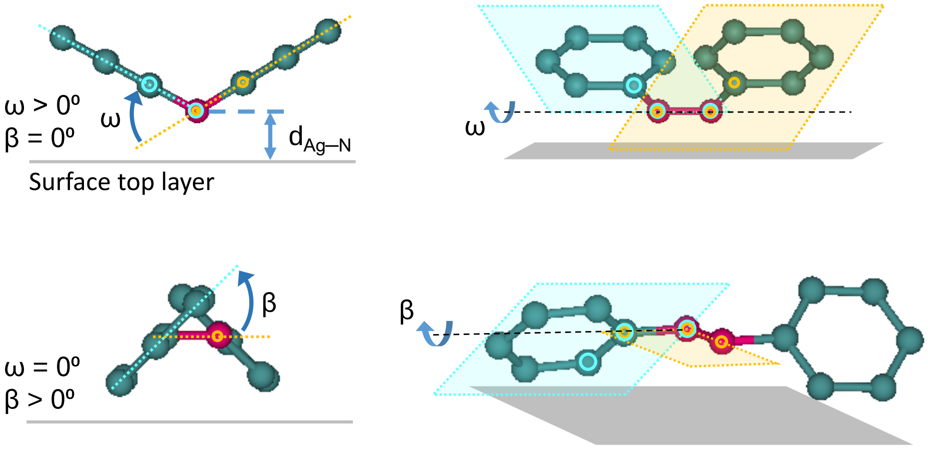

Figure 4.7. Ball-stick models of AB describing ring tilt angle ω and the twist angle β. Atoms defining the planes are indicated with circles marked with the same colors as the corresponding planes. H atoms are not shown.

i.) *t*-AB Adsorbate Geometries and Vibrational Spectra

Among all the SM-SERS jumps, that of *t*-AB1 (Figure 4.4a) exhibits the highest similarity with the isolated *t*-AB spectrum (Figure 4.6a). In Figure 4.4a, the modes at 1388 and 1413 cm^{-1} are attributed to N=N stretching of the azo-bridge which is observed at 1440 cm^{-1} for *t*-AB. On the other hand, the mode observed at 1440 cm^{-1} is attributed to be similar to 1465 cm^{-1} mode in *t*-AB which is assigned to the C–C stretching coupled with N=N stretching (Table 4.2.)

The observed downward shifts in the modes involving the N=N stretching indicate a decrease in the N=N bond order (i.e., decrease in sp^2 character) due to distortion of the planar configuration of the molecule. On the other hand, relatively smaller shifts observed in the modes related to the C–C and C–H vibrations of the phenyl rings suggest that the ring–substrate interaction is not strong. Thus, it is inferred that *t*-AB1 is associated with adsorption to a high coordinated surface (i.e., Ag–Ag), such as Ag (111).

Figures 4.8a-b show the optimized structures and the corresponding Raman spectra of *t*-AB$_{\mathrm{Ag\,(111)}}$, *t*-AB$_{\mathrm{Ag\,(100)}}$, *t*-AB$_{\mathrm{Ag\,(110)}}$ adsorbates, respectively. While the calculated Raman spectrum of *t*-AB $_{\mathrm{Ag\,(111)}}$ in Figure 4.8a shows similarities to that of *t*-AB1 (Figure 4.4), the two spectra have major differences, specifically in the vibrational modes related to the azo-bridge. The major N=N stretching for *t*-AB $_{\mathrm{Ag\,(111)}}$ is observed at 1330 cm^{-1}. Further, another N=N stretching mode is observed at 1295 cm^{-1} which is coupled with C-H in-plane bending. These two modes are thought to be similar to those at 1388 and 1413 cm^{-1} for *t*-AB1, respectively. The observed differences between the calculated and predicted values for *t*-AB on Ag (111) surface can be understood by examining the structural parameters of *t*-AB $_{\mathrm{Ag\,(111)}}$ given in Table 4.3. As seen in Figure 4.8, *t*-AB $_{\mathrm{Ag\,(111)}}$ structure is close to being planar with a ring tilt angle of ω=2°, and ring rotation angles of β=5.9º and β'=3.9º. The average adsorption height, $d_{\mathrm{Ag–N}}$ is calculated to be 2.77 Å which is significantly lower than the experimental value of ≈3.07 Å calculated by Mercurio et al.[187]. Further, our calculation estimates the adsorption energy (E_{Ads}) as being 2.4 eV whereas the experimental value was found to be ≈1.00 eV [187] .

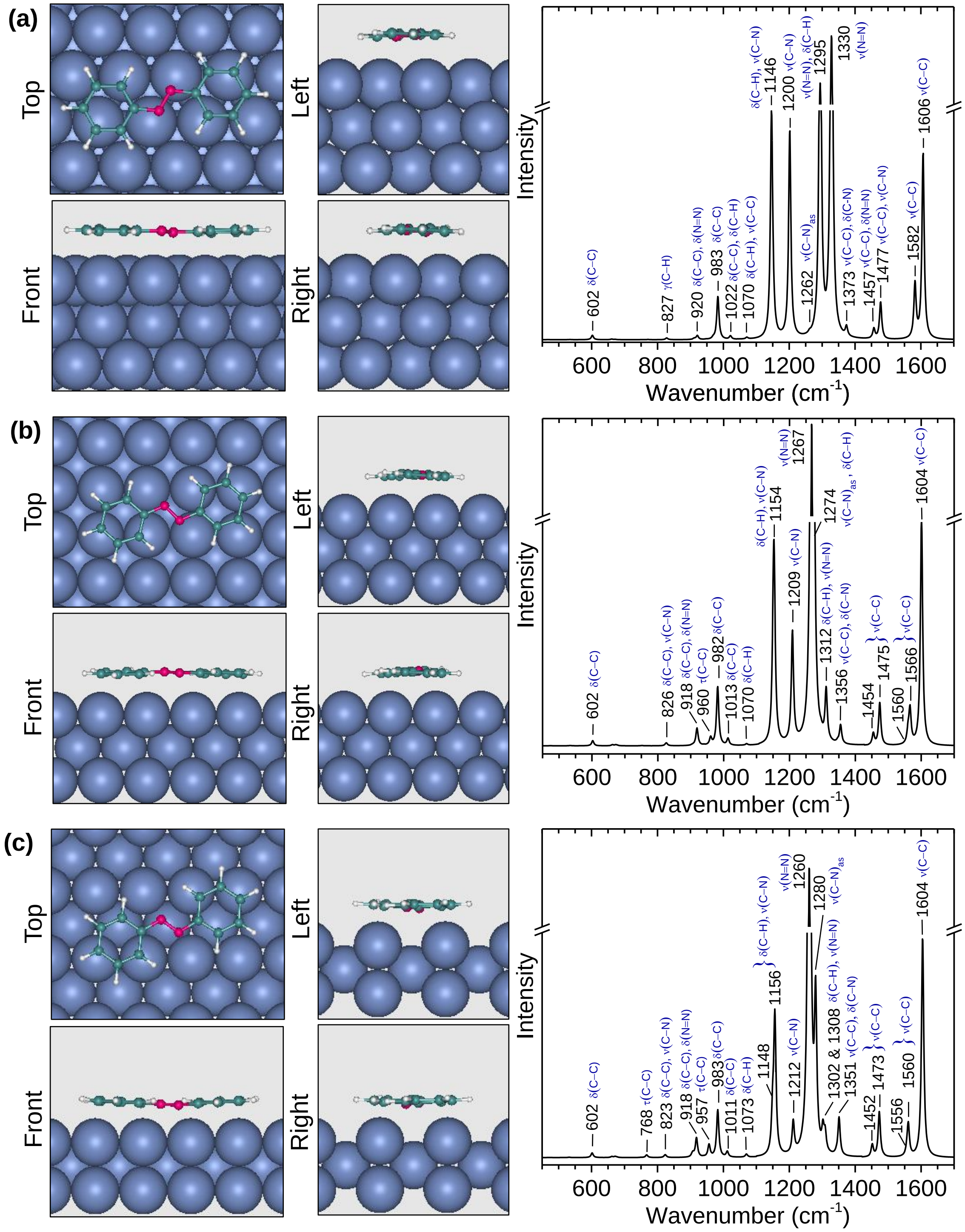

Figure 4.8. Optimized structures (left panel) and calculated Raman spectra (right panel) of: t-AB$_{\mathrm{Ag(111)}}$ **(a)**; t-AB$_{\mathrm{Ag(100)}}$ **(b)**; t-AB$_{\mathrm{Ag(110)}}$ **(c)**. The structures are viewed from top, front and sides where blue: Ag, green: C, white: H, and magenta: N. In the Raman spectra, υ: stretch, δ: in-plain bend, γ: out-of-plain bend, and τ: torsion.

Table 4.3. Adsorption energy (E_{Ads}) and structural parameters of free and surface adsorbed *t*-AB as obtained using GGA-PBE/D3. Parameters are as defined in Figures 4.5 and 4.7.

	$d_{Ag–N}$ (Å)	$d_{Ag–N'}$ (Å)	$d_{C–N}$ (Å)	$d_{C'–N'}$ (Å)	$d_{N–N'}$ (Å)	ω (deg)	β (deg)	β′ (deg)	E_{Ads} (eV)
t-AB	–	–	1.40	1.40	1.27	0	0	0	–
t-$AB_{Ag(111)}$	2.7	2.8	1.40	1.40	1.31	2	5.9	3.9	-2.4
t-$AB_{Ag(100)}$	2.6	2.7	1.40	1.40	1.32	0.4	0.4	7.3	-2.9
t-$AB_{Ag(110)}$	2.3	2.3	1.40	1.39	1.32	6.0	5.3	0.1	-2.1

The underestimation of the adsorption height accompanied by overestimation of the E_{Ads} of AB on Ag (111) surface was also observed in other studies using GGA-PBE with Grimme's DFT-D2 correction scheme [186-188] When another dispersion correction, Tkatchenko and Scheffler (TS), was used, the adsorption height was calculated accurately (2.98 Å), while the E_{Ads} was improved yet still overestimated (1.71 eV) [186-188]. TS method is essentially identical to DFT-D2. However, unlike in DFT-D2, the dispersion coefficients and damping function in TS method are charge-density dependent. To further improve the accuracy of the calculated adsorbate structures, Mercurio et al. investigated various factors in DFT-D2 and TS dispersion correction schemes [187]. Their results indicated that the error in the estimated adsorption height and energy is due to an inaccuracy in the screening of dispersive attractions between the adsorbate and distant substrate atoms. By adjusting the pairwise C_6R^{-1} term to reduce the number of substrate layer included in TS dispersion correction scheme, they were able to calculate the structural properties accurately. Unfortunately, the ABINIT software used in the present study does not offer such flexibility in adjusting the parameters of the dispersion correction scheme used. Further, the TS method is not provided in the ABINIT software. Hence, we are unable to do similar improvements in our calculations. However, we predict that with the above-mentioned improvements, the resulting vibrational spectra resembling that in *t*-AB1 could be obtained.

t-AB2 spectrum (Figure 4.4b), shows significant variations from that of isolated *t*-AB, particularly in the 1200-1300 cm^{-1} and 1500-1650 cm^{-1} regions. The modes observed at 1544, 1596 and 1630 cm^{-1} are associated with quadrant C–C ring vibrations which show substantial variations from those for *t*-AB at 1591 cm^{-1} (Quadrant I) and 1608 (Quadrant II). The separation (upward and downward shifts) of the quadrant stretching frequencies is attributed to the increased C–C bond length alternation which indicates the involvement of the rings in the chemisorption of AB onto the Ag surface. Thus, adsorption to the Ag surface is inferred to be much stronger for *t*-AB2. In such an adsorption configuration, a smaller distance between the azo-bridge and the metal surface, $d_{Ag–N}$, and the weakening of the N=N bond which would result in a substantial downshift in its stretching frequency is expected. Indeed, the new mode observed in Figure 4.4b at 1275 cm^{-1} lie in the region of the spectra where single N–N stretching vibrations are observed. Thus, this mode might be attributed to the N=N stretching in *t*-AB2.

In the spectrum of *t*-AB3, which is represented by Figure 4.4c, while the quadrant C–C ring vibrations don't show significant variation from those for isolated t-AB and *t*-AB1, the modes observed at 1200 and 1283 cm^{-1} resemble the modes at 1210 and 1275 cm^{-1} for *t*-AB2. Therefore, as in *t*-AB2, $d_{Ag–N}$ is expected to be shortened compared to that in *t*-AB1, but unlike in *t*-AB2, the rings are expected to have weaker interaction with the metal.

The calculated spectrum of AB on Ag (100) and Ag (110) surfaces (*t*-$AB_{Ag\,(100)}$ and *t*-$AB_{Ag(110)}$, respectively) in Figure 4.8 display striking similarities to that of *t*-AB3. In *t*-AB3 spectrum (Figure 4.4a) the modes observed at 1220 and 1265 cm^{-1} are calculated at 1209 and 1267 cm^{-1} for *t*-$AB_{Ag\,(100)}$, and 1212 and 1260 $cm^{-1}$for *t*-$AB_{Ag\,(110)}$ which are assigned to the C–N stretching and N=N stretching coupled with the C–N stretching, respectively. Further, the quadrant C–C ring vibrations are calculated at 1560, 1566 and 1601 cm^{-1} for *t*-$AB_{Ag\,(100)}$ and at

1556, 1560 and 1604 cm^{-1} for *t*-AB$_{\mathrm{Ag\ (110)}}$, which are identical to those observed for *t*-AB3 at 1558 and 1588 cm^{-1}.

The significant downward shift in the N=N stretching of *t*-AB on Ag (100) and Ag (110) indicates a considerable decrease in the bond order as is apparent from the increased N=N bond length from 1.28 to 1.32 Å on both surfaces (Table 4.3). Thus, the azo-bridge is expected to be closer to the surface, relative to that in t-AB$_{\mathrm{Ag\ (111)}}$. Indeed, computations confirm the average distance of the azo-bridge from the Ag surface, $d_{\mathrm{Ag-N}}$ =2.6 and 2.3 Å for *t*-AB$_{\mathrm{Ag\ (100)}}$ and *t*-AB$_{\mathrm{Ag\ (110)}}$, respectively (Table 4.3).

As given in Table 4.3 and also observed in Figure 4.8, *t*-AB$_{\mathrm{Ag\ (100)}}$ is close to being planar with ω= 0.4º. Further, the rings are twisted where β=0.4º and β'=7.3º. On the other hand, the distortion of the planar geometry in AB is more pronounced in *t*-AB$_{\mathrm{Ag\ (110)}}$ due to the low adsorption height which pulls the molecule into the repulsive regime of the potential surface. Consequently, the rings are pushed away from the surface where ω=6º. The rings are also twisted by β=5.3º and β'=0.1º. The asymmetric twisting of the rings in both adsorbate structures is attributed to asymmetric adsorption of AB on Ag (100) and Ag (110) surfaces. Interestingly, the calculated E_{Ads} of *t*-AB on Ag (100) is 2.9 eV which is higher than that on Ag (110) surface at 2.1 eV (Table 4.3). Due to its relatively low coordination, Ag (110) is a more reactive surface with respect to Ag (100) surface. In fact, among all surfaces studied, *t*-AB has the shortest adsorption height on Ag (110) (2.3 Å). Hence, E_{Ads} is expected to be the highest for *t*-AB$_{\mathrm{Ag\ (110)}}$. However, the lower adsorption height of *t*-AB$_{\mathrm{Ag\ (110)}}$ comes with an energetic cost arising from the significant distortion of the planar geometry (i.e., ω=6º, β=5.3º and β'=0.1º). It is inferred that this energetic cost is the reason behind the relatively low E_{Ads} for *t*-AB on Ag (110) surface.

In *t*-AB2 spectrum, the C–C stretching and N=N stretching vibrations are assigned to the modes at 1210 and 1275 cm^{-1}, respectively, matching both with those for *t*-AB$_{\mathrm{Ag\ (100)}}$ and *t*-AB$_{Ag(110)}$. However, the frequency shifts in quadrant stretches calculated for *t*-AB$_{Ag\ (100)}$ and *t*-AB$_{Ag\ (110)}$ are not as significant as those observed for *t*-AB2. The significant variation observed in the quadrant C–C stretches of *t*-AB2 is attributed to binding of the rings to the metal surface. As computationally shown by Chen at al., the adsorption of benzene onto Au (100) surface involves e^{-} donation/backdonation to/from the metal orbitals. Their calculation showed that benzene favours the adsorption to hollow sites which results in re-hybridization of two opposite carbon atoms from sp^{2} to sp^{3}. Further, the charge density of the two carbon atoms increased while the rest of the carbon atoms lost charge density. As a result, the C–C bond length increased from 1.385 Å to 1.42 and 1.40 Å. Their frontier molecular orbital analysis showed that highest occupied molecular orbital (HOMO) becomes smaller, indicating a charge transfer to the metal substrate. In addition, the lowest unoccupied molecular orbital LUMO showed the hybridization of benzene and metal orbital, which was attributed to the e^{-} back donation from dz$_{2}$ orbital to the LUMO of benzene. In *t*-AB2 a similar interaction of the rings with the Ag surface is anticipated. However, it is clear that the DFT-PBE method cannot produce such charge transfer interaction between AB and the Ag surface.

Intrudingly, our calculations on two-layer Ag clusters performed using Gaussian 09 software with GGA functional WB97XD, which uses a version of Grimme's D2 dispersion model, is able to produce the observed shift in the C–C stretches on Ag (100) surface. Figure 4.9a shows the optimized structure and the corresponding Raman spectra of t-AB on Ag (100) cluster. The vibrational spectra, given in Figure 4.9a, has a striking resemblance to that of *t*-AB2 (Figure 4.4b). Further, the vibrational spectra of *t*-AB calculated similarly on Ag (110) cluster is identical to that of *t*-AB$_{Ag\ (110)}$ as well as to that of *t*-AB3 (Figure 4.9b and 4.4c, respectively).

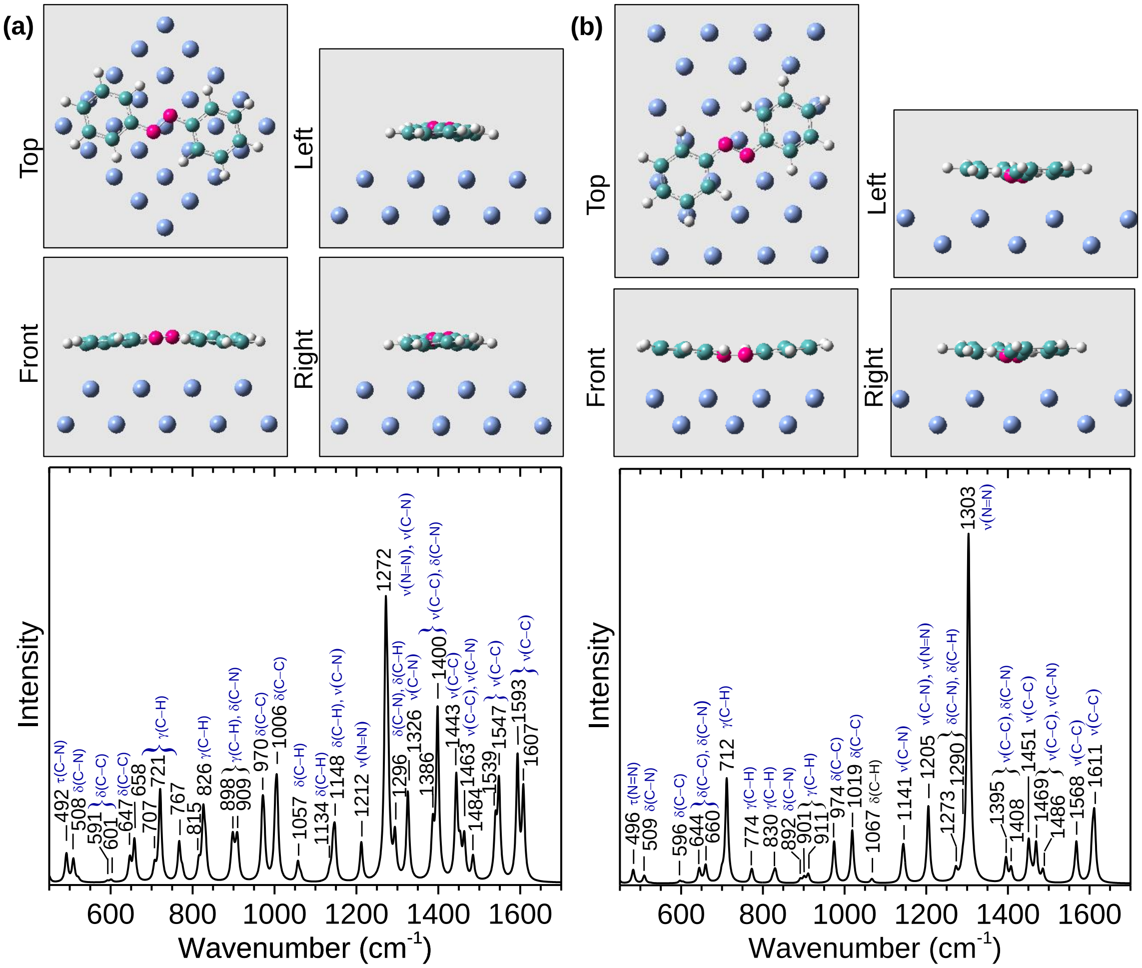

Figure 4.9. Optimized structures (top panel) and Raman spectra (bottom panel) of *t*-AB calculated using GGA-WB97XD functional on; Ag(100) surface cluster **(a)**; Ag(110) surface cluster **(b)**. The structures are viewed from top, front and sides. Blue: Ag; green: C; white: H; magenta; N.

The frontier orbitals HOMO, LUMO and LUMO+1 of *t*-AB on Ag (100) cluster are given in Figure 4.10. All three orbitals show hybridization of *t*-AB and metal orbitals, indicating charge transfer interactions. The interaction between the C atoms and Ag cluster seen in HOMO is attributed to σ-donation from C p_z molecular orbitals to metal d_{z^2} orbitals. On the other hand, in LUMO+1, the *t*-AB π* orbital accepts charge donation from metal d_{xy} orbitals (i.e., π-acceptor). Further, interaction between the azo-bridge and the metal surface is also observed as seen in LUMO which is attributed to σ-donation from N p_z molecular orbitals to metal d_{z^2} orbitals. Accordingly, it is inferred that *t*-AB2 is associated with a surface adsorbate similar to *t*-$AB_{Ag\,(100)}$. On the other hand, *t*-AB3 is associated with a surface adsorbate similar to *t*-$AB_{Ag\,(110)}$.

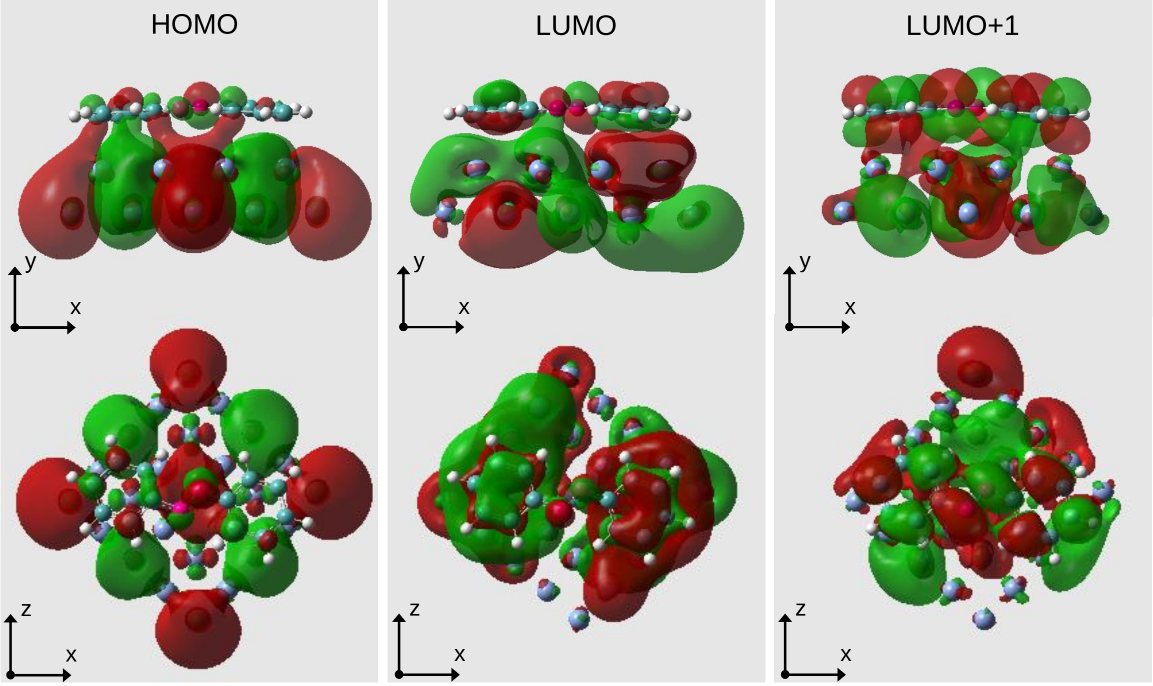

Figure 4.10. Frontier molecular orbitals of *t*-AB adsorbed onto Ag (100) surface cluster.

ii.) *c*-AB Adsorbate Geometries and Vibrational Spectra

The SM jumps associated with *cis*-AB in Figures 4.4d-f are observed to have strong resemblance to *t*-AB2 and *t*-AB3 jumps in Figure 4.4b and 4.4c, respectively. Both *c*-AB1 (Figure 4.4d) and *c*-AB2 (Figure 4.4e) jumps exhibit a peak at ~1530 cm^{-1} which is in the range where the N=N stretching of isolated *c*-AB is observed (Table 4.2). However, for *c*-AB adsorbed on Ag surface, the N=N stretch is expected to shift to a lower wavenumber due to bonding of azo-bridge with the substrate. In fact, this shift is expected to be greater than what is observed for *t*-AB since the uplifted rings of *c*-AB allow the azo-bridge to be closer to the metal surface due to minor interaction of the rings with the substrate. Thus, the mode observed at ~1530 cm^{-1} is rather assigned to the ring quadrant C–C vibrations (Quadrant I) similar to the mode observed at ~1540 cm^{-1} in Figure 4.4b. Thus, it is anticipated that in *c*-AB1 and *c*-AB2, one of the rings resides on the metal surface while the other ring is lifted away from the surface. A further decrease in the Quadrant I vibration from ~1540 cm^{-1} to ~1530 cm^{-1} indicates a reduced ring-metal distance which is expected since one of the rings is lifted away from the metal surface. Unlike in *c*-AB1 and *c*-AB2 spectra, Quadrant I vibration in c-AB3 jump shows a relatively small shift to ~1565 cm^{-1}. However, a significant shift in Quadrant II from 1605 cm^{-1} to 1660 cm^{-1} is observed. Further, all three *c*-AB spectra in Figure 4.4d-f exhibit a mode at ~1340 cm^{-1}. This mode is observed to be exclusive to *cis* conformer as also supported by the EA-SERS study in *Section 4.3.1*. Further, similar to *t*-AB jumps in Figure 4.4a-c, new modes are observed in 1200-13000 cm^{-1} region which are attributed to the vibrations associated with the azo-bridge.

Figure 4.11a-c show the optimized structures and the corresponding Raman spectra of *c*-$AB_{Ag\,(111)}$, *c*-$AB_{Ag\,(100)}$, *c*-$AB_{Ag\,(110)}$ adsorbates, respectively. In all three adsorbate structures, one of the rings is lifted away from the surface while the other ring resides close to the surface. As seen in Table 4.4, the adsorption height of the *c*-AB adsorbates are significantly reduced compared to *t*-AB adsorbates on the same surfaces. The N=N bond lengths, $d_{N-N'}$, are similar to those observed for *t*-AB adsorbates. This is also reflected in the calculated N=N stretching vibrations in Figure 4.11 which are observed in the same frequency range as for *t*-AB adsorbates in Figure 4.8. Further, the *c*-AB structure is significantly disturbed on all three surfaces as is apparent from significant increase in the ring tilt angles ω, and the decrease in the ring twist angles β and β' in Table 4.4.

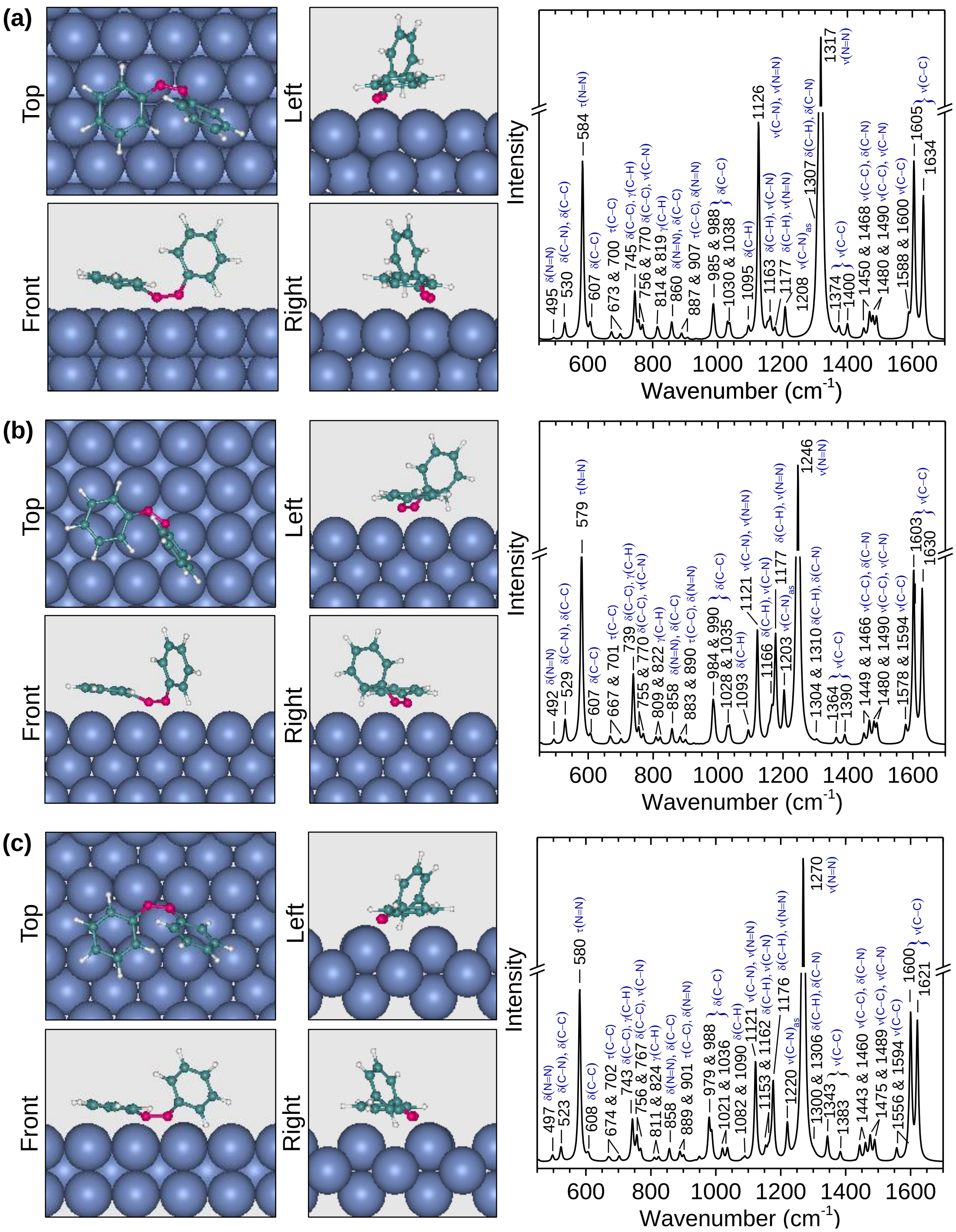

Figure 4.11. Optimized structures (left panel) and calculated Raman spectra (right panel) of: *c*-AB$_{\mathrm{Ag(111)}}$ **(a)**; *c*-AB$_{\mathrm{Ag(100)}}$ **(b)**; *c*-AB$_{\mathrm{Ag(110)}}$ **(c)**. The structures are viewed from top, front and sides where blue: Ag, green: C, white: H, and magenta: N. In the Raman spectra, υ: stretch, δ: in-plain bend, γ: out-of-plain bend, and τ: torsion.

Table 4.4. Adsorption energy (E_{Ads}) and structural parameters of free and surface adsorbed *c*-AB as obtained using GGA-PBE/D3. Parameters are as defined in Figures 4.5 and 4.7.

	$d_{Ag–N}$ (Å)	$d_{Ag–N'}$ (Å)	$d_{C–N}$ (Å)	$d_{C'–N'}$ (Å)	$d_{N–N'}$ (Å)	ω (deg)	β (deg)	β′ (deg)	E_{Ads} (eV)
c-AB	–	–	1.44	1.44	1.26	12	48	48	–
c-$AB_{Ag(111)}$	2.1	2.2	1.42	1.40	1.31	26	42	24	-2.0
c-$AB_{Ag(100)}$	2.0	2.1	1.42	1.41	1.33	34	31	29	-2.3
c-$AB_{Ag(110)}$	1.9	1.9	1.40	1.40	1.33	28	24	28	-1.9

Using the vibrations related to N=N and C–N bonds, we infer that that *c*-AB1, *c*-AB2, and *c*-AB3 are associated with adsorption to Ag (111), Ag (100), and Ag (110) surfaces, respectively. The N=N stretching frequency in c-$AB_{Ag(111)}$ spectra is observed at 1317 cm^{-1}. This is slightly higher than the range in which N=N stretching is observed for *c*-AB1 (1285-1300 cm^{-1}) in Figure 4.4d and in Figures A19-24 in Appendices. On the other hand, the N=N stretching frequency calculated for *c*-$AB_{Ag(100)}$ at 1246 cm^{-1} and for *c*-$AB_{Ag(100)}$ at 1270 cm^{-1} matches those observed for *c*-AB2 and *c*-AB3, respectively (Figures 4.4e-f and Figure A25-36). However, the C–C stretching frequencies calculated for *c*-AB do not match well to the experimentally observed values for single *c*-AB adsorbates. This is attributed to the inability of DFT to effectively simulate the interactions (i.e., charge transfer) between aromatic rings and the Ag surface as also shown for *t*-AB on Ag (100) surface. It is inferred that, in all three adsorbates, the ring residing close to the substrate have charge transfer interactions with the metal surface.

The adsorption energies of *c*-AB adsorbates are given in Table 4.4. The energetic cost of the significant distortion of the free c-AB structure on all three surfaces is reflected in the adsorption energies (Table 4.4). Although the *c*-AB adsorbates have a shorter adsorption height compared to their *t*-AB counterparts, their E_{ads} are lower. The lowest E_{Ads} is observed for c-

$AB_{Ag(110)}$ (1.9 eV) for which the most significant distortion of the free c-AB geometry is observed (Table 4.4).

According to the above-discussed experimental and computational results, *t*-AB1, *t*-AB2, and *t*-AB3 are attributed to *t*-AB adsorbates having the same conformation and surface interaction as those on Ag (111), Ag (100), and Ag (110) surfaces, respectively. Similarly, *c*-AB1, *c*-AB2, and *c*-AB3 are attributed to *c*-AB adsorbates having the same conformation and surface interaction as those on Ag (111), Ag (100), and Ag (110) surfaces, respectively.

4.3.5. Photoswitching of Single Azobenzene Molecules on Nanosilver Facets

The switching from *t*-AB to *c*-AB is demonstrated in EA-SERS measurements with in-situ excitation at 365 nm in *Section 4.3.1*. Similarly, we performed SM-SERS acquisitions under in-situ UV excitation (365 nm LED). While they are rare, transitions between *t*-AB and *c*-AB were captured as shown in Figure 4.12-4.17. Interestingly, switching events occur only between *t*-AB and *c*-AB adsorbates which are attributed to the same crystal facets (i.e., Ag(111), Ag(100), and Ag(110)). Figures 4.12-4.14 show *t*-AB1→*c*-AB1, *t*-AB2→*c*-AB2, and *t*-AB3→*c*-AB3 transitions of AB, respectively. Reverse transitions of *c*-AB1→*t*-AB1, *c*-AB2→*t*-AB2, and *c*-AB3→*t*-AB3 are also observed as shown in Figures 4.15-4.17, respectively. In addition, some SM jumps, as in Figure 4.15, show multiple transitions between *t*-AB and *c*-AB. No switching event between AB adsorbates associated with different crystal facet are observed. Further, transition events between the different adsorbates of the same isomer (i.e., *trans* and *cis*) are also not observed. This support the hypothesis that distinct adsorbates observed for *t*-AB and *c*-AB originates from distinct crystal facets of Ag NPs, rather than being different adsorption configurations on the same crystal facet.

Many studies have shown that AB loses its photoswitching capability even on the least reactive coinage metal surfaces (e.g., Au (111) and Ag (111)). On Ag (111), the bistability (i.e., existence of two stable conformation) of AB was found to be lost due to lowering of the ground state barrier along the rotational pathway resulting from the strong coupling of the barrier geometries to the surface. Curiously, we observe both *t*-AB and *c*-AB in SM-SERS measurements which indicates that surface adsorbates of both isomers are stable on Ag NPs. Further, our SM-SERS measurements and DFT study suggest that reversible switching of AB takes place on the Ag (111), Ag (100), and Ag (110) facets of Ag NPs. As our discussion on the SM-SERS detection technique used in the present study suggest (*Chapter III*), the diffusion of a molecule on Ag NP surface occurs as subsequent desorption−re-adsorption events. Thus, the observed switching events might be occurring upon desorption of the molecules during its surface diffusion. In fact, in some of the captured switching events (as in Figure 4.12 and 4.13), the overall SERS intensity decreases dramatically just before a switching event (orange spectra). This might be attributed to desorption and subsequent switching of the molecule before its re-adsorption to the surface, suggesting that observed switching events may not necessarily be happening in the adsorbed states of AB on Ag surface. Nevertheless, this observation is significant since it indicates that surface decoupling of AB is required for switching.

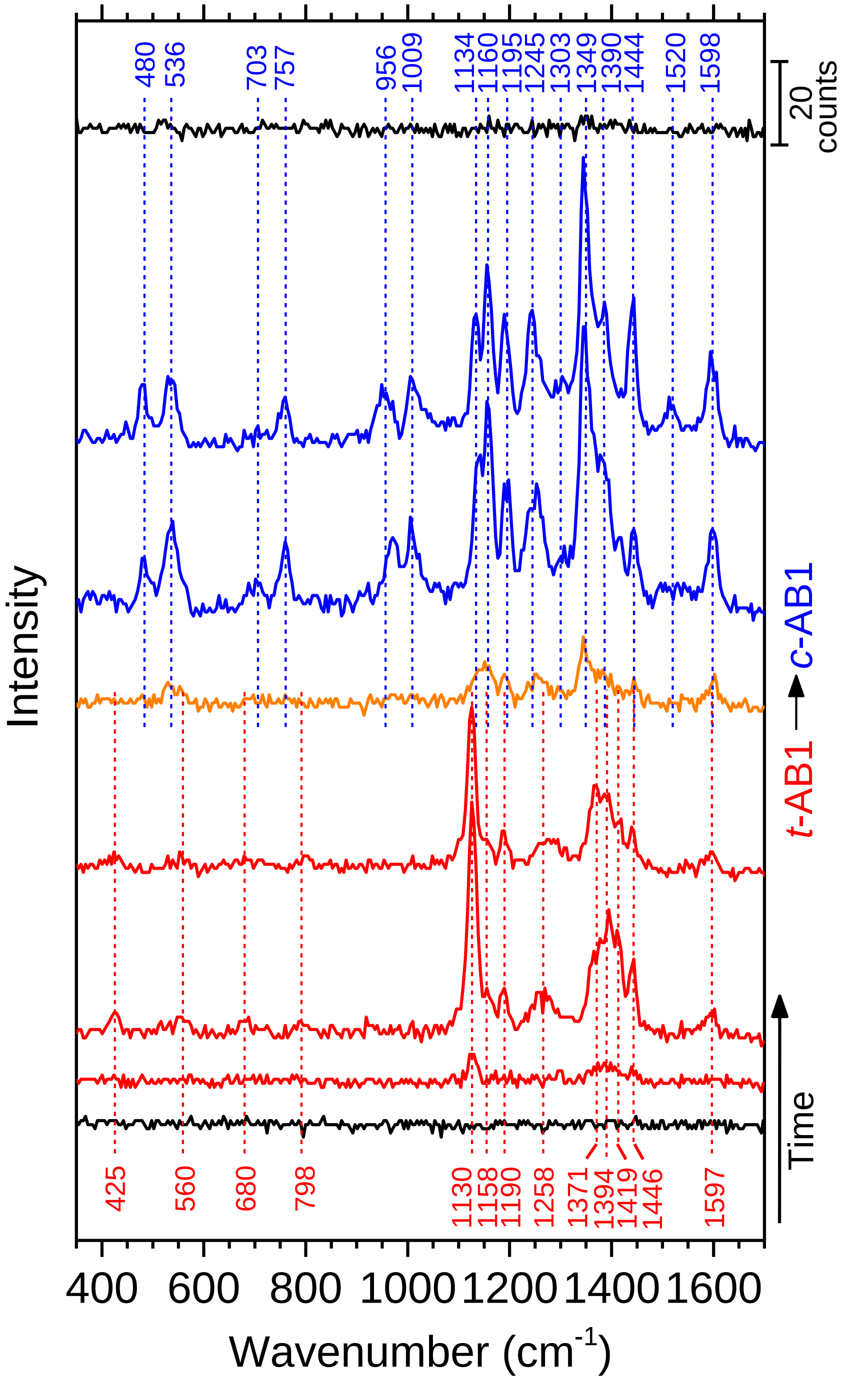

Figure 4.12. Time-series spectra showing *t*-AB1 → *c*-AB1 switching on Ag NPs at 40 ms intervals. The red and blue colors represent *trans* and *cis* isomers, respectively. The orange spectra containing the markers of both isomers is transitioning between *trans* and *cis*.

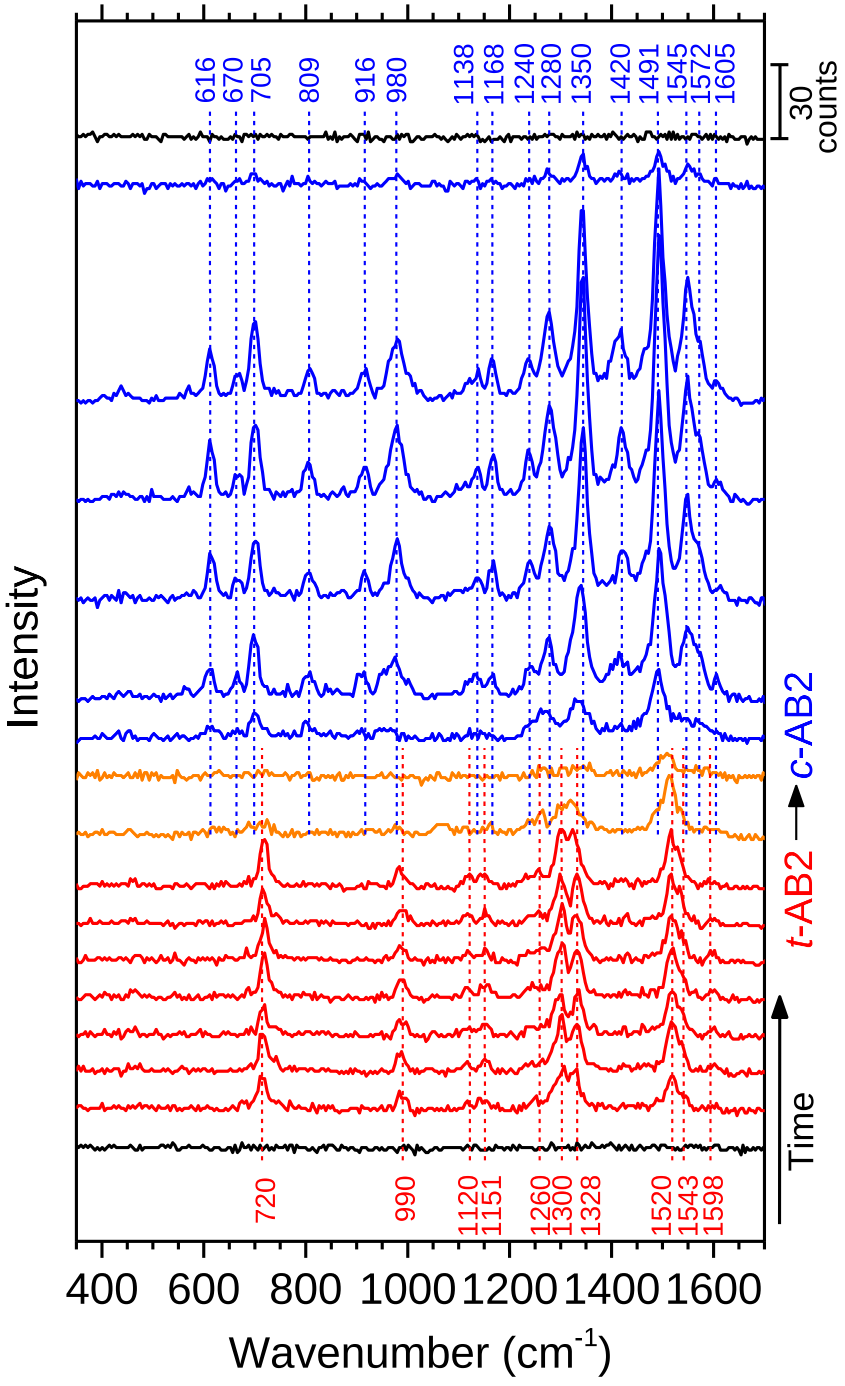

Figure 4.13. Time-series spectra showing *t*-AB2 → *c*-AB2 switching on Ag NPs at 40 ms intervals. The red and blue colors represent *trans* and *cis* isomers, respectively. The orange spectra containing the markers of both isomers is transitioning between *trans* and *cis*.

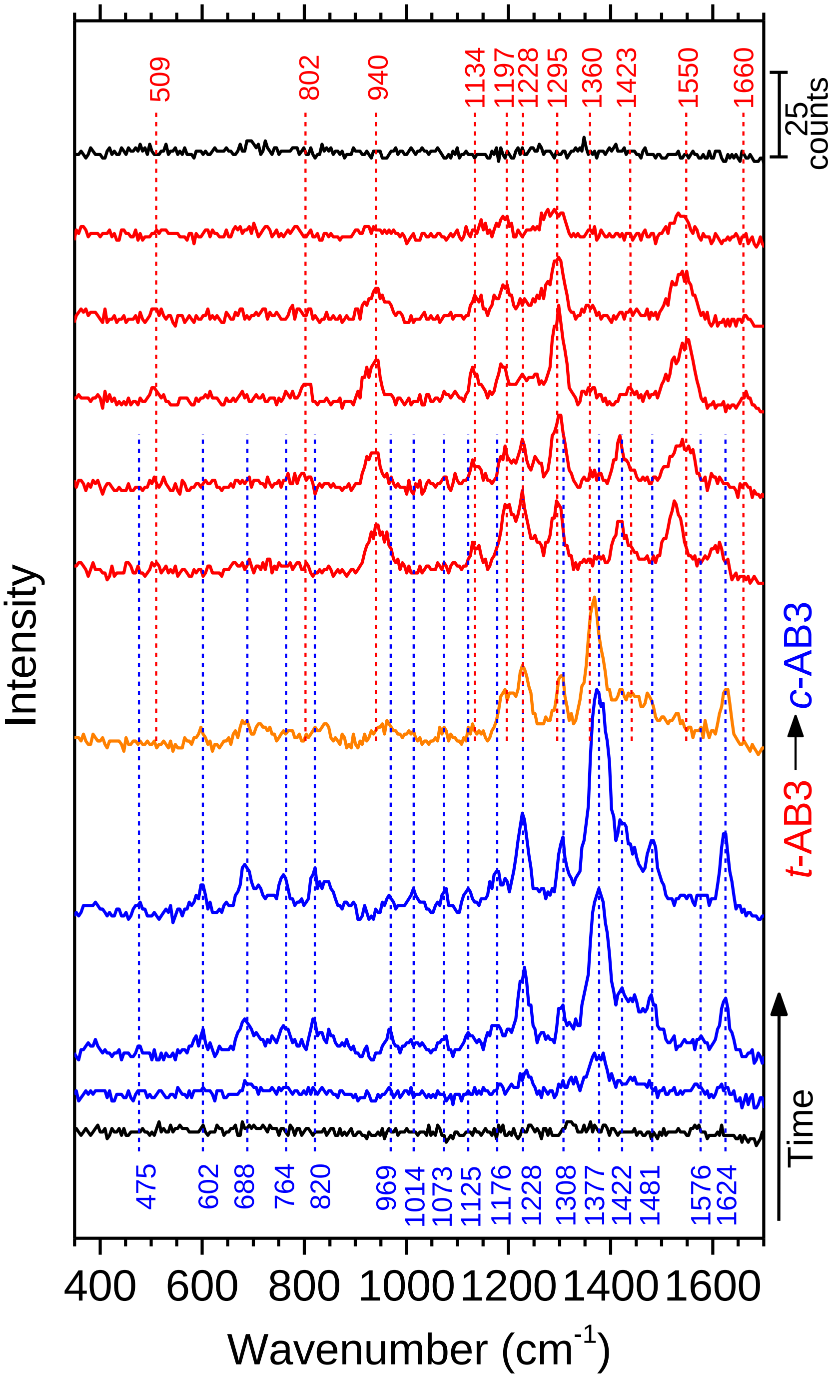

Figure 4.14. Time-series spectra showing *t*-AB3 → *c*-AB3 switching on Ag NPs at 40 ms intervals. The red and blue colors represent *trans* and *cis* isomers, respectively. The orange spectra containing the markers of both isomers is transitioning between *trans* and *cis*.

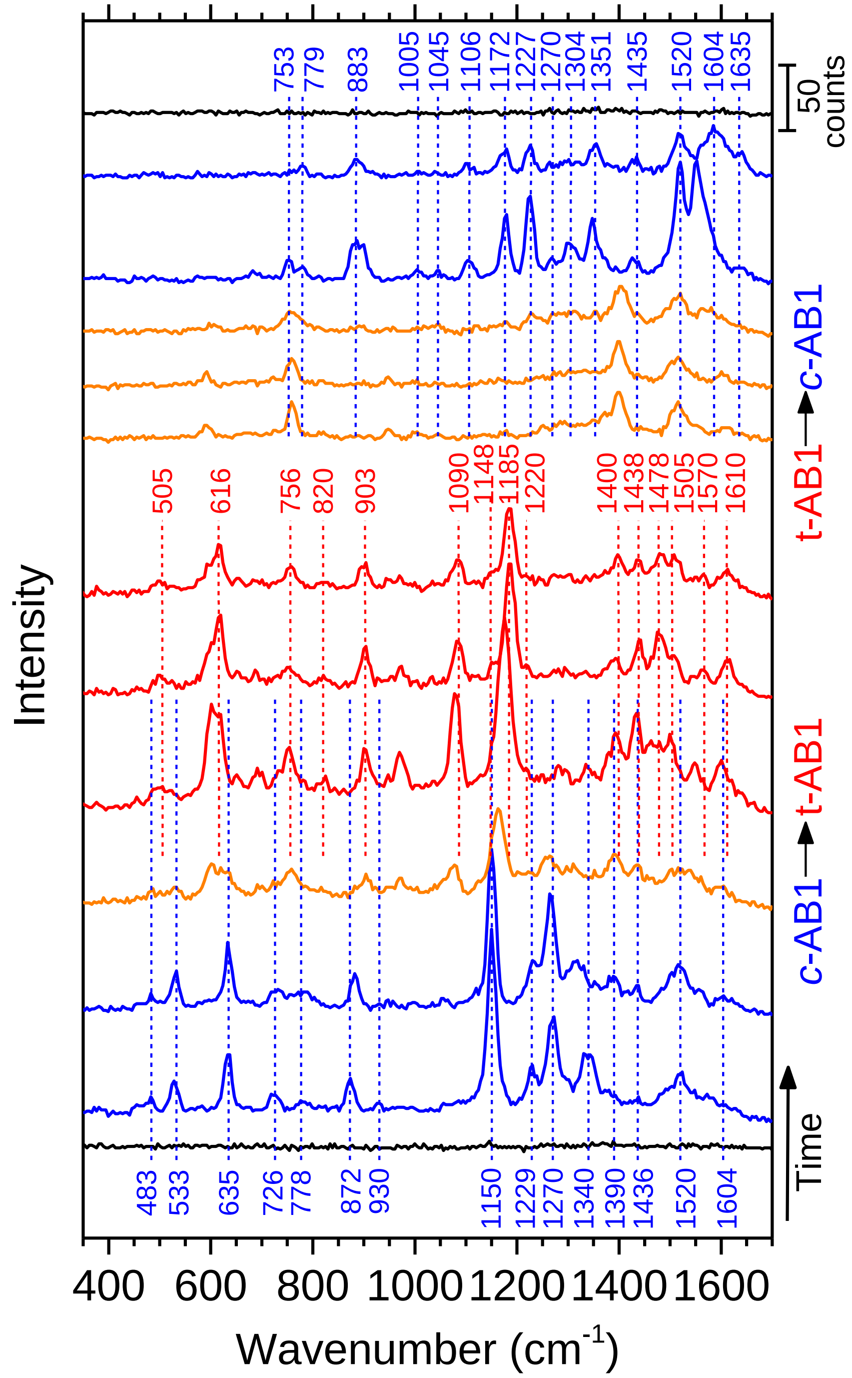

Figure 4.15. Time-series spectra showing *c*-AB1 → *t*-AB1 → c-AB1 switching on Ag NPs at 40 ms intervals. The red and blue colors represent *trans* and *cis* isomers, respectively. The orange spectra containing the markers of both isomers is transitioning between *trans* and *cis*.

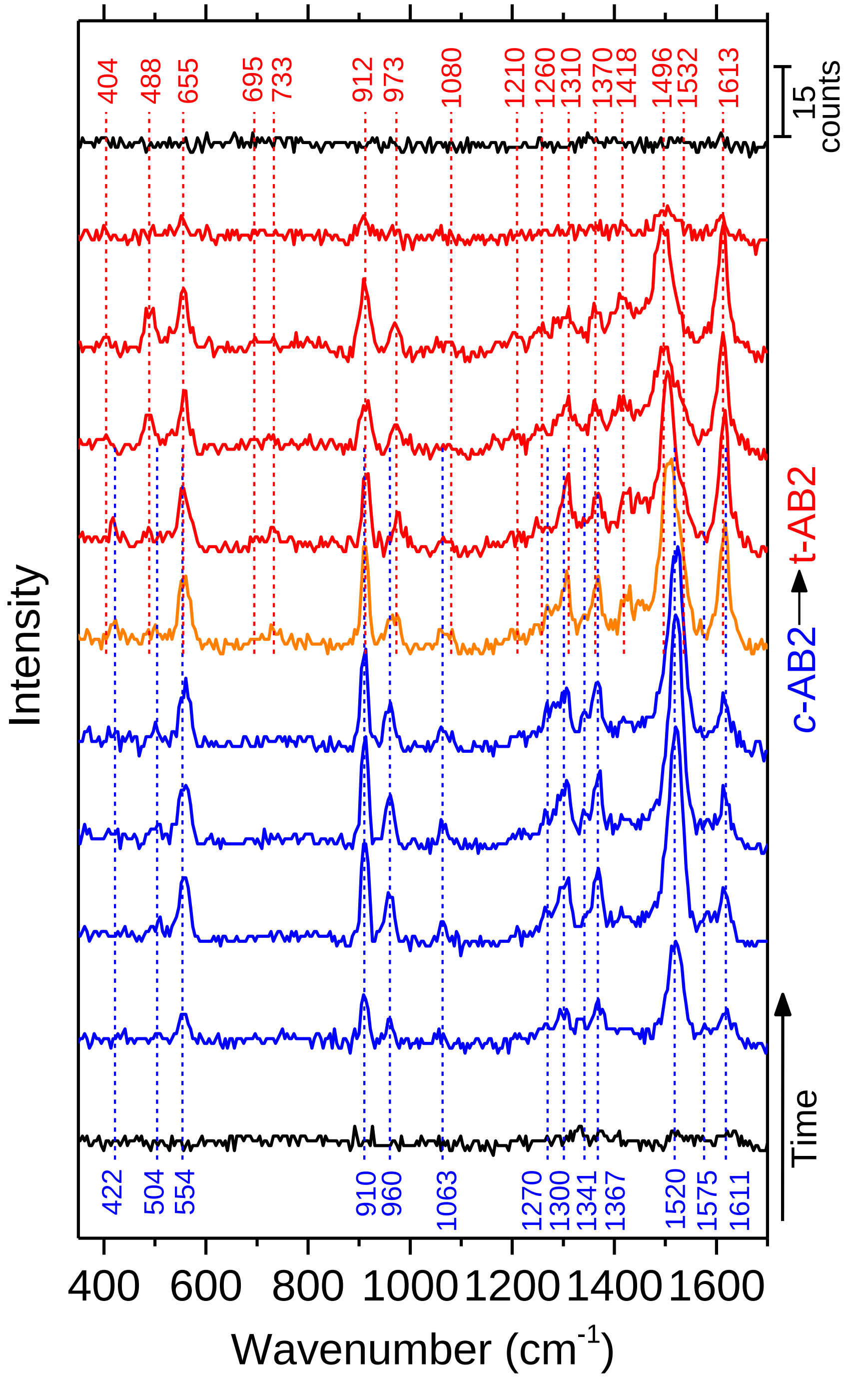

Figure 4.16. Time-series spectra showing *c*-AB2 → *t*-AB2 switching on Ag NPs at 40 ms intervals. The red and blue colors represent *trans* and *cis* isomers, respectively. The orange spectra containing the markers of both isomers is transitioning between *trans* and *cis*.

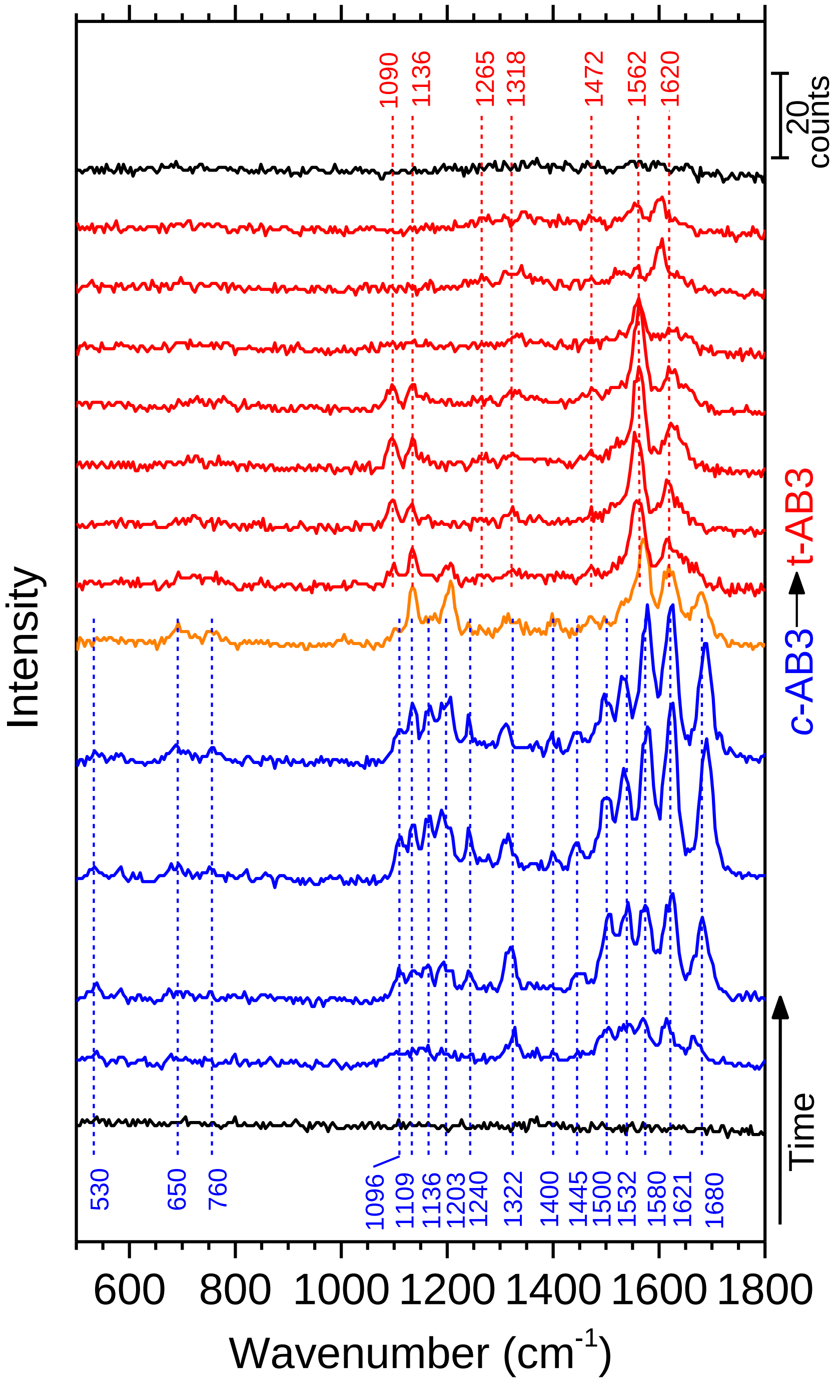

Figure 4.17. Time-series spectra showing *c*-AB3 → *t*-AB3 switching on Ag NPs at 40 ms intervals. The red and blue colors represent *trans* and *cis* isomers, respectively. The orange spectra containing the markers of both isomers is transitioning between *trans* and *cis*.

4.4. Conclusions

In the present work we demonstrate the effect of surface geometry (i.e., crystal orientation) on the surface adsorption of single AB molecules by studying their vibrational spectra using SERS. The SM-SERS measurements revealed three distinct species of both *t*-AB and *c*-AB based on our SERS jumps. With the help of DFT calculations we show that this three-fold multiplicity originates from the heterogeneity of the adsorption sites on the Ag NPs. In particular, we hypothesize three facets of different crystal orientation available for adsorption. In particular, we assign the observed SM-SERS jumps to surface adsorbates of *t*-AB and *c*-AB on Ag (111), Ag (100) and Ag (110) surfaces.

Our DFT computations and SM-SERS spectra shows that adsorption mechanism and the resulting adsorbate geometry varies significantly on surfaces of different crystal orientation. In *t*-AB adsorbates attributed to Ag (100) and Ag (110) surfaces, vibrational modes related to the azo-bridge exhibits significant downward frequency shifts indicating a strong interaction between the azo-bridge and the metal surface. Further, in *t*-AB associated with Ag (100) surface, the vibrational modes related to the aromatic rings exhibit significant frequency shift with respect to the isolated AB (non-adsorbed). The calculated frontier molecular orbitals of *t*-AB on Ag (100) surface show hybridization of AB molecular orbitals with d orbitals of Ag. In particular, HOMO and LUMO orbital point to a σ-donation from C atoms of the phenyl ring and N atoms of azo-bridge to the orbitals to metal d_{z^2} orbitals, respectively. In addition, the hybridization of the AB π* orbital with metal d_{xy} orbitals indicates charge donation from Ag to AB. Similar charge transfer interactions are also inferred between metal and *c*-AB based on the similar changes observed in the SM-SERS of *c*-AB adsorbates on Ag NPs.

We also observe switching of single AB molecules in SERS spectra collected under in-situ UV excitation. The switching events are found to occur only between *t*-AB and *c*-AB adsorbates which are attributed to the same crystal facets (i.e., Ag(111), Ag(100), and Ag(110)). No switching events between AB adsorbates associated with different crystal facet are observed. Further, transition events between the different adsorbates of the same isomer (i.e., *trans* and *cis*) are also not observed. This support the hypothesis that distinct adsorbates observed for *t*-AB and *c*-AB originates from distinct crystal facets of Ag NPs, rather than being different adsorption configurations on the same crystal facet. In some SERS spectra, the overall SERS intensity is observed to decrease dramatically just before an switching event, which is attributed to desorption of the molecule followed by an switching event. This suggests that observed switching events may not necessarily be happening in the adsorbed states of AB on Ag surface. Nevertheless, this observation is significant since it indicates that surface decoupling of AB is required for switching to occur.

While single molecule spectroscopy opens up a window into the private world of molecules, single molecules themselves can be reporters for the local environment. In the present work, such value of single molecule spectroscopy is demonstrated where the differentiating effect of surface crystal orientations in Ag NPs on the adsorption configuration of AB SMs, as distinguished from their distinct SERS spectra, is observed.

CHAPTER V

CONCLUSIONS

In the two decades since its first demonstration, SERS has proven itself as a viable SM detection technique by resolving various chemical and physical phenomena which are specific to SMs. Today, developments in technologies for fabrication as well as evaluation (i.e., experimental and computational) of plasmonic SERS substrates points to future milestones in SM-SERS research. However, the road to the current consensus that SM detection by SERS is possible has not been without its challenges. An immense amount of research has shown that the SM-SERS phenomenon is a complex one which requires precise knowledge of the dynamic factors governing both the molecules under study and the plasmonic substrates used. Nevertheless, with careful analysis of SM spectra along with the investigation of the underlying electromagnetic and chemical SERS phenomena, the SM nature of a SERS spectra can be determined, as demonstrated in the present study.

In the present study, we first set out to investigate the plasmonic properties of our Ag-nanohemispheres-on-Ge-nanoposts SERS substrates. As experimentally demonstrated and computationally elucidated, NHSs exhibit remarkably different plasmonic characteristics as compared to nanospheres. The broken symmetry by asymmetric particle shape leads to dipolar modes parallel (in-plane) and normal to the base (out-of-plane), which are significantly different in terms of energy, excitation dependence on polarization, and electromagnetic coupling. The unique characteristics of both parallel and perpendicular plasmon modes discovered in the present study point to potential applications of Ag-on-Ge substrates in various plamonic applications, including plasmonic photovoltaics, photocatalysis, UV plasmonics, and chemical detection (i.e., LSPR and SERS).

Just like molecules, plasmonic NPs have rich and complex physical and chemical properties. Other than just providing the giant SERS enhancements required to detect SMs, they actively interact with the molecules under study. Further, plasmonic NPs are nanocrystals with multiple facets at different crystal orientations. Hence, they provide a rich platform to molecules for surface adsorption. While this may be not be desired both in SM and ensemble-averaged studies as it complicates the interpretation of the data, we recognize this as a powerful tool to study the surface adsorption of a molecular switch, azobenzene (AB).

In the present work, the SM-SERS measurements reveal three distinct species of *trans*-AB (*t*-AB) and *cis*-AB (*c*-AB) on the surface of Ag NHSs. With the help of DFT calculations we show that there are three facets of different crystal orientation available for adsorption on our Ag NHSs. In particular, we assign the observed SM-SERS jumps to surface adsorbates of *t*-AB and *c*-AB on Ag (111), Ag (100) and Ag (110) surfaces. Our experimental and computational results indicate that adsorption mechanism and the resulting adsorbate geometry of AB varies significantly on surfaces of different crystal orientation. By studying the variations in vibrational frequencies of single AB molecules, we are able to resolve molecule-surface interactions, such as bonding and charge transfer, for different units of AB (i.e., azo-bridge and phenyl rings).

The reversible photoswitching of AB molecules is also observed at single molecule level under in-situ UV excitation. It is found that switching occurs only between *t*-AB and *c*-AB adsorbates which are attributed to the same crystal facets (i.e., Ag (111), Ag (100), and Ag (110)). This support the hypothesis that distinct adsorbates observed for *t*-AB and *c*-AB originates from distinct crystal facets of Ag NPs, rather than being different adsorption configurations on the same crystal facet.

While the observation of photoswitching of a single AB molecule is unique, the analysis of the SM-SERS spectra showing transitions between *t*-AB and *c*-AB suggest that the switching events may not necessarily be happening in the adsorbed states of AB on Ag surface. Nevertheless, this observation is significant since it indicates that surface decoupling of AB is required for switching to occur. However, a further study is required for a solid conclusion on the surface origin of the switching of AB on Ag NPs.

In the present work, the SM origin of the observed SERS signal is supported by the observation of various phenomenon. In agreement with the current SM-SERS literature, these observations are attributed to SM detection as discussed in *Chapter III*. However, an in-depth statistical analysis of these observations is needed for a concrete proof of the SM detection in the present work. Particularly in the multi-analyte method, which is considered as the most reliable proof of SM-SERS detection, a systematic concentration study determining the cross-over regime between multi-molecule detection and SM detection would provide the concentration range in which the SM detection is possible. Such an information might allow for improvement of the measurement parameters, such as laser power, laser spot size, analyte concentration, and integration time for a higher signal intensity and a better time resolution.

While the experimental and computational results indicate that the distinct SM-SERS spectra of *t*-AB and *c*-AB originates from different crystal facets available for adsorption, the existence of various adsorbate configurations on a single facet or on defect sites (i.e., kinks, steps, and corners) cannot be eliminated in the present study. One approach to further elucidate the origin of the observed heterogeneity of the SM-SERS signal is to carry out SERS measurements on well-defined single crystal surfaces of various orientations (i.e., Ag (111), Ag (100), and Ag (110)) using, such as, gap-mode SERS or tip-enhanced Raman spectroscopy (TERS) techniques. Future computational studies using where different adsorption configurations on a single crystal surface with a well-defined orientation, as well as with defects may also give clues about the origin of the signal heterogeneity. Unfortunately, such studies are computationally expensive and could not be performed with the resources available to us.

While single molecule spectroscopy opens up a window into the private world of molecules, single molecules themselves can be reporters for their local environment. The present work demonstrates such value of SM-SERS where the differentiating effect of surface crystal orientations in Ag NPs on the adsorption configuration of AB SMs leads to the realization of the multifaceted nature of our NPs.

REFERENCES

1. Kwan, C.S., et al., *Higher-generation type III-B rotaxane dendrimers with controlling particle size in three-dimensional molecular switching.* Nature Communications, 2018. **9**.

2. Hell, S.W. and M. Kroug, *Ground-state-depletion fluorescence microscopy - a concept for breaking the diffraction resolution limit.* Applied Physics B-Lasers and Optics, 1995. **60**(5): p. 495-497.

3. Hell, S.W. and J. Wichmann, *Breaking the diffraction resolution limit by stimulated-emission - stimulated-emission-depletion fluorescence microscopy.* Optics Letters, 1994. **19**(11): p. 780-782.

4. Betzig, E., *Proposed method for molecular optical imaging.* Optics Letters, 1995. **20**(3): p. 237-239.

5. Betzig, E., et al., *Imaging intracellular fluorescent proteins at nanometer resolution.* Science, 2006. **313**(5793): p. 1642-1645.

6. Klar, T.A., et al., *Fluorescence microscopy with diffraction resolution barrier broken by stimulated emission.* Proceedings of the National Academy of Sciences of the United States of America, 2000. **97**(15): p. 8206-8210.

7. Moerner, W.E. and L. Kador, *Finding a single molecule in a haystack - optical-detection and spectroscopy of single absorbers in solids.* Analytical Chemistry, 1989. **61**(21): p. A1217-A1223.

8. Moerner, W.E. and L. Kador, *Optical-detection and spectroscopy of single molecules in a solid.* Physical Review Letters, 1989. **62**(21): p. 2535-2538.

9. De Bo, G., et al., *Sequence-specific beta-homo peptide synthesis by an artificial small-molecule machine.* Abstracts of Papers of the American Chemical Society, 2017. **254**.

10. De Bo, G., et al., *Sequence-specific peptides synthesis by an artificial small-molecule machine.* Abstracts of Papers of the American Chemical Society, 2013. **246**.

11. Kassem, S., et al., *Pick-up, transport and release of a molecular cargo using a small-molecule robotic arm.* Nature Chemistry, 2016. **8**(2): p. 138-143.

12. Lewandowski, B., et al., *Sequence-specific peptide synthesis by an artificial small-molecule machine.* Science, 2013. **339**(6116): p. 189-193.

13. Kassem, S., et al., *Stereodivergent synthesis with a programmable molecular machine.* Nature, 2017. **549**(7672): p. 374-378.

14. Kudernac, T., et al., *Electrically driven directional motion of a four-wheeled molecule on a metal surface.* Nature, 2011. **479**(7372): p. 208-211.

15. Badjic, J.D., et al., *A molecular elevator.* Science, 2004. **303**(5665): p. 1845-1849.

16. Chang, J.C., et al., *Mechanically interlocked daisy-chain-like structures as multidimensional molecular muscles.* Nature Chemistry, 2017. **9**(2): p. 128-134.

17. Green, J.E., et al., *A 160-kilobit molecular electronic memory patterned at 10(11) bits per square centimetre.* Nature, 2007. **445**(7126): p. 414-417.

18. Ichimura, K., et al., *Reversible change in alignment mode of nematic liquid-crystals regulated photochemically by command surfaces modified with an azobenzene monolayer.* Langmuir, 1988. **4**(5): p. 1214-1216.

19. Ikeda, T. and O. Tsutsumi, *Optical switching and image storage by means of azobenzene liquid-crystal films.* Science, 1995. **268**(5219): p. 1873-1875.

20. Mativetsky, J.M., et al., *Azobenzenes as light-controlled molecular electronic switches in nanoscale metal-molecule-metal junctions.* Journal of the American Chemical Society, 2008. **130**(29): p. 9192-9193.

21. Morgenstern, K., *Switching individual molecules by light and electrons: From isomerisation to chirality flip.* Progress in Surface Science, 2011. **86**(5-8): p. 115-161.

22. Zhang, C., et al., *Coherent electron transport through an azobenzene molecule: A light-driven molecular switch.* Physical Review Letters, 2004. **92**(15).

23. Alemani, M., et al., *Adsorption and switching properties of azobenzene derivatives on different noble metal surfaces: Au(111), Cu(111), and Au(100).* The Journal of Physical Chemistry C, 2008. **112**(28): p. 10509-10514.

24. Comstock, M.J., et al., *Measuring reversible photomechanical switching rates for a molecule at a surface.* Applied Physics Letters, 2008. **92**(12): p. 123107 (1-3).

25. Comstock, M.J., et al., *Reversible photomechanical switching of individual engineered molecules at a metallic surface.* Physical Review Letters, 2007. **99**(3): p. 038301 (1-4).

26. Hagen, S., et al., *Excitation mechanism in the photoisomerization of a surface-bound azobenzene derivative: Role of the metallic substrate.* The Journal of Chemical Physics, 2008. **129**(16): p. 164102.

27. Henningsen, N., et al., *Trans to cis isomerization of an azobenzene derivative on a Cu(100) surface.* Applied Physics A, 2008. **93**(2): p. 241-246.

28. Henzl, J., et al., *Photoisomerization for a molecular switch in contact with a surface.* Physical Review B, 2012. **85**(3): p. 035410 (1-5).

29. Reuter, R.J.M.a.K., *Bistability loss as a key feature in azobenzene (non-)switching on metal surfaces.* Angewandte Chemie International Edition, 2012. **51**: p. 12009-12011.

30. Singhal, K. and A.K. Kalkan, *Surface-enhanced Raman scattering captures conformational changes of single photoactive yellow protein molecules under photoexcitation.* Journal of the American Chemical Society, 2010. **132**(2): p. 429-431.

31. Topal, C.O.K., Md. Shfayet; Kalkan, A. Kaan, *Conformational transitions in single GFP molecules near equilibrium.* 2018.

32. Kalkan, A.K. and S.J. Fonash, *Laser-activated surface-enhanced Raman scattering substrates capable of single molecule detection.* Applied Physics Letters, 2006. **89**(23): p. 233103.

33. Topal, Ç.Ö., et al., *Plasmon resonances in nanohemisphere monolayers.* The Journal of Physical Chemistry C, 2017. **121**(42): p. 23599-23608.

34. Bandara, H.M.D. and S.C. Burdette, *Photoisomerization in different classes of azobenzene.* Chemical Society Reviews, 2012. **41**(5): p. 1809-1825.

35. Schulze, F.W., et al., *Thermodynamic properties of the structural analogues benzo[c]cinnoline, trans-azobenzene, and cis-azobenzene.* Zeitschrift für Physikalische Chemie, 1977. **107**(1): p. 1-9.

36. Bortolus, P. and S. Monti, *Cis-trans photoisomerization of azobenzene. Solvent and triplet donors effects.* The Journal of Physical Chemistry, 1979. **83**(6): p. 648-652.

37. Siampiringue, N., et al., *The cis → trans photoisomerization of azobenzene: an experimental re-examination.* Journal of Photochemistry, 1987. **37**(1): p. 185-188.

38. Bortolus, P. and S. Monti, *cis↔trans Photoisomerization of azobenzene*-cyclodextrin *inclusion complexes.* The Journal of Physical Chemistry, 1987. **91**(19): p. 5046-5050.

39. Rau, H. and E. Lueddecke, *On the rotation-inversion controversy on photoisomerization of azobenzenes. Experimental proof of inversion.* Journal of the American Chemical Society, 1982. **104**(6): p. 1616-1620.

40. Rau, H., *Further evidence for rotation in the π,π* and inversion in the n,π* photoisomerization of azobenzenes.* Journal of Photochemistry, 1984. **26**(2): p. 221-225.

41. Fujino, T. and T. Tahara, *Picosecond time-resolved Raman study of trans-azobenzene.* The Journal of Physical Chemistry A, 2000. **104**(18): p. 4203-4210.

42. Fujino, T., S.Y. Arzhantsev, and T. Tahara, *Femtosecond time-resolved fluorescence study of photoisomerization of trans-azobenzene.* The Journal of Physical Chemistry A, 2001. **105**(35): p. 8123-8129.

43. Ishikawa, T., T. Noro, and T. Shoda, *Theoretical study on the photoisomerization of azobenzene.* The Journal of Chemical Physics, 2001. **115**(16): p. 7503-7512.

44. Biswas, N. and S. Umapathy, *Early time dynamics of trans-azobenzene isomerization in solution from resonance Raman intensity analysis.* The Journal of Chemical Physics, 1997. **107**(19): p. 7849-7858.

45. Wei-Guang Diau, E., *A new trans-to-cis photoisomerization mechanism of azobenzene on the S1(n,π*) surface.* The Journal of Physical Chemistry A, 2004. **108**(6): p. 950-956.

46. Bandara, H.M.D., et al., *Proof for the concerted inversion mechanism in the trans→cis isomerization of azobenzene using hydrogen Bbonding to induce isomer locking.* The Journal of Organic Chemistry, 2010. **75**(14): p. 4817-4827.

47. Tan, E.M.M., et al., *Fast photodynamics of azobenzene probed by scanning excited-state potential energy surfaces using slow spectroscopy.* Nature Communications, 2015. **6**: p. 5860.

48. Zhou, X.L., X.Y. Zhu, and J.M. White, *Photochemistry at adsorbate/metal interfaces.* Surface Science Reports, 1991. **13**(3): p. 73-220.

49. Hagen, S., et al., *Reversible switching of tetra-tert-butyl-azobenzene on a Au(111) surface induced by light and thermal activation.* Chemical Physics Letters, 2007. **444**(1): p. 85-90.

50. Óvári, L., M. Wolf, and P. Tegeder, *Reversible changes in the vibrational structure of tetra-tert-butylazobenzene on a Au(111) surface induced by light and thermal activation.* The Journal of Physical Chemistry C, 2007. **111**(42): p. 15370-15374.

51. Alemani, M., et al., *Electric field-induced isomerization of azobenzene by STM.* Journal of the American Chemical Society, 2006. **128**(45): p. 14446-14447.

52. Choi, B.-Y., et al., *Conformational molecular switch of the azobenzene molecule: A scanning tunneling microscopy study.* Physical Review Letters, 2006. **96**(15): p. 156106 (1-4).

53. Henzl, J., et al., *Reversible cis–trans isomerization of a single azobenzene molecule.* Angewandte Chemie International Edition, 2006. **45**(4): p. 603-606.

54. Henzl, J., T. Bredow, and K. Morgenstern, *Irreversible isomerization of the azobenzene derivate Methyl Orange on Au(111).* Chemical Physics Letters, 2007. **435**(4): p. 278-282.

55. Henningsen, N., et al., *Inducing the rotation of a single phenyl ring with tunneling electrons.* The Journal of Physical Chemistry C, 2007. **111**(40): p. 14843-14848.

56. Anker, J.N., et al., *Biosensing with plasmonic nanosensors.* Nature Materials, 2008. **7**(6): p. 442-453.

57. Gish, D.A., et al., *Localized surface plasmon resonance biosensor using silver nanostructures fabricated by glancing angle deposition.* Analytical Chemistry, 2007. **79**(11): p. 4228-4232.

58. Hicks, E.M., et al., *Plasmonic properties of film over nanowell surfaces fabricated by nanosphere lithography.* Journal of Physical Chemistry B, 2005. **109**(47): p. 22351-22358.

59. Irit, N., et al., *Silica-stabilized gold island films for transmission localized surface plasmon sensing.* Journal of the American Chemical Society, 2007. **129**(1): p. 84-92.

60. Kedem, O., et al., *Sensitivity and optimization of localized surface plasmon resonance transducers.* ACS Nano, 2011. **5**(2): p. 748-760.

61. Theiss, J., et al., *Plasmonic nanoparticle arrays with nanometer separation for high-performance SERS substrates.* Nano Letters, 2010. **10**(8): p. 2749-2754.

62. Alvarez-Puebla, R., et al., *Nanoimprinted SERS-active substrates with tunable surface plasmon resonances.* Journal of Physical Chemistry C, 2007. **111**(18): p. 6720-6723.

63. He, L.B., et al., *Systematic investigation of the SERS efficiency and SERS hotspots in gas-phase deposited Ag nanoparticle assemblies (Vol 19, pg 5091, 2017).* Physical Chemistry Chemical Physics, 2017. **19**(26): p. 17469-17469.

64. Stuart, H.R. and D.G. Hall, *Absorption enhancement in silicon-on-insulator waveguides using metal island films.* Applied Physics Letters, 1996. **69**(16): p. 2327-2329.

65. Atwater, H.A. and A. Polman, *Plasmonics for improved photovoltaic devices.* Nature Materials, 2010. **9**(3): p. 205-213.

66. Mirin, N.A. and N.J. Halas, *Light-Bending Nanoparticles.* Nano Letters, 2009. **9**(3): p. 1255-1259.

67. Nomura, W., M. Ohtsu, and T. Yatsui, *Nanodot coupler with a surface plasmon polariton condenser for optical far/near-field conversion.* Applied Physics Letters, 2005. **86**(18): p. 181108 (1-3).

68. Nakayama, K., K. Tanabe, and H.A. Atwater, *Plasmonic nanoparticle enhanced light absorption in GaAs solar cells.* Applied Physics Letters, 2008. **93**(12): p. 121904 (1-3).

69. Sil, D., et al., *Seeing is believing: hot electron based gold nanoplasmonic optical hydrogen sensor.* ACS Nano, 2014. **8**(8): p. 7755-7762.

70. Qiu, J., et al., *Plasmon-enhanced water splitting on* TiO_2*-passivated GaP photocatalysts* Physical Chemistry Chemical Physics, 2014. **16**(48): p. 27134-27134.

71. Li, H.X., et al., *Surface-plasmon-resonance-enhanced photoelectrochemical water splitting from Au-nanoparticle-decorated 3D* TiO_2 *nanorod architectures.* Journal of Physical Chemistry C, 2017. **121**(22): p. 12071-12079.

72. Catchpole, K.R. and A. Polman, *Plasmonic solar cells.* Optics Express, 2008. **16**(26): p. 21793-21800.

73. Bhatt, K., et al., *Charge-selective Raman scattering and fluorescence quenching by "nanometal on semiconductor" substrates.* Nano Letters, 2010. **10**(10): p. 3880-3887.

74. Yang, Y., et al., *Ultraviolet nanoplasmonics: A demonstration of surface-enhanced Raman spectroscopy, fluorescence, and photodegradation using gallium nanoparticles.* Nano Letters, 2013. **13**(6): p. 2837-2841.

75. Attanayake, T., M. Premaratne, and G. Agrawal, *Characterizing the optical response of symmetric hemispherical nano-dimers.* Plasmonics, 2015. **10**(6): p. 1453-1466.

76. Schneider, C.A., W.S. Rasband, and K.W. Eliceiri, *NIH Image to ImageJ: 25 years of image analysis.* Nature Methods, 2012. **9**(7): p. 671-675.

77. Kreibig, U., B. Schmitz, and H.D. Breuer, *Separation of plasmon-polariton modes of small metal particles.* Physical Review B, 1987. **36**(9): p. 5027-5030.

78. Millstone, J.E., et al., *Observation of a quadrupole plasmon mode for a colloidal solution of gold nanoprisms.* Journal of the American Chemical Society, 2005. **127**(15): p. 5312-5313.

79. Payne, E.K., et al., *Multipole plasmon resonances in gold nanorods.* Journal of Physical Chemistry B, 2006. **110**(5): p. 2150-2154.

80. Bastus, N.G., J. Piella, and V. Puntes, *Quantifying the sensitivity of multipolar (dipolar, quadrupolar, and octapolar) surface plasmon resonances in silver nanoparticles: The effect of size, composition, and surface coating.* Langmuir, 2016. **32**(1): p. 290-300.

81. Zhang, C., et al., *Fitting-determined formulation of effective medium approximation for 3D trench structures in model-based infrared reflectrometry.* Journal of the Optical Society of America A, 2011. **28**(2): p. 263-271.

82. Donovan, T.M., et al., *Optical properties of amorphous germanium films.* Physical Review B, 1970. **2**(2): p. 397-413.

83. Gao, T.C., et al., *Designing metal hemispheres on silicon ultrathin film solar cells for plasmonic light trapping.* Optics Letters, 2014. **39**(16): p. 4647-4650.

84. Christopher, P., H. Xin, and S. Linic, *Visible-light-enhanced catalytic oxidation reactions on plasmonic silver nanostructures.* Nature Chemistry, 2011. **3**: p. 467-472.

85. Xu, P., et al., *Mechanistic understanding of surface plasmon assisted catalysis on a single particle: Cyclic redox of 4-aminothiophenol.* Scientific Reports, 2013. **3**: p. 2997.

86. Mubeen, S., et al., *An autonomous photosynthetic device in which all charge carriers derive from surface plasmons.* Nature Nanotechnology, 2013. **8**: p. 247-251.

87. Thomann, I., et al., *Plasmon enhanced solar-to-fuel energy conversion.* Nano Letters, 2011. **11**(8): p. 3440-3446.

88. Lee, S.W., et al., *The surface plasmon-induced hot carrier effect on the catalytic activity of CO oxidation on a* Cu_2O*/hexoctahedral Au inverse catalyst.* Nanoscale, 2018. **10**(23): p. 10835-10843.

89. Murdoch, M., et al., *The effect of gold loading and particle size on photocatalytic hydrogen production from ethanol over Au/TiO_2 nanoparticles.* Nature Chemistry, 2011. **3**: p. 489-492.

90. Zhang, P., M. Fujitsuka, and T. Majima, *Hot electron-driven hydrogen evolution using anisotropic gold nanostructure assembled monolayer MoS_2.* Nanoscale, 2017. **9**(4): p. 1520-1526.

91. Sanz, J.M., et al., *UV plasmonic behavior of various metal nanoparticles in the near- and far-field regimes: Geometry and substrate effects.* Journal of Physical Chemistry C, 2013. **117**(38): p. 19606-19615.

92. Albella, P., et al., *Shape matters: Plasmonic manoparticle shape enhances interaction with dielectric substrate.* Nano Letters, 2011. **11**(9): p. 3531-3537.

93. Knight, M.W., et al., *Substrates matter: Influence of an adjacent dielectric on an individual plasmonic nanoparticle.* Nano Letters, 2009. **9**(5): p. 2188-2192.

94. Prodan, E., et al., *A hybridization model for the plasmon response of complex nanostructures.* Science, 2003. **302**(5644): p. 419-422.

95. Lynch, D.W. and W.R. Hunter, *Comments on the Optical Constants of Metals and an Introduction to the Data for Several Metals*, in *Handbook of Optical Constants of Solids*, E.D. Palik, Editor. 1985, Academic Press: Boston. p. 275-367.

96. Zhou, W. and T.W. Odom, *Tunable subradiant lattice plasmons by out-of-plane dipolar interactions.* Nature Nanotechnology, 2011. **6**: p. 423-427.

97. Le Ru, E.C., et al., *Surface enhanced Raman scattering enhancement factors: A comprehensive study.* The Journal of Physical Chemistry C, 2007. **111**(37): p. 13794-13803.

98. Le Ru, E.C. and P.G. Etchegoin, *Single-molecule surface-enhanced Raman spectroscopy.* Annual Review of Physical Chemistry, 2012. **63**(1): p. 65-87.

99. Hao, E. and G.C. Schatz, *Electromagnetic fields around silver nanoparticles and dimers.* Journal of Chemical Physics, 2004. **120**(1): p. 357-366.

100. Doering, W.E. and S.M. Nie, *Single-molecule and single-nanoparticle SERS: Examining the roles of surface active sites and chemical enhancement.* Journal of Physical Chemistry B, 2002. **106**(2): p. 311-317.

101. Haran, G., *Single molecule Raman spectroscopy and local work function fluctuations.* Israel Journal of Chemistry, 2004. **44**(4): p. 385-390.

102. Yu, X.X., et al., *Tuning chemical enhancement of SERS by controlling the chemical reduction of graphene oxide nanosheets.* ACS Nano, 2011. **5**(2): p. 952-958.

103. Zhao, L.L., L. Jensen, and G.C. Schatz, *Pyridine-Ag-20 cluster: A model system for studying surface-enhanced Raman scattering.* Journal of the American Chemical Society, 2006. **128**(9): p. 2911-2919.

104. Lombardi, J.R. and R.L. Birke, *A unified view of surface-enhanced Raman scattering.* Accounts of Chemical Research, 2009. **42**(6): p. 734-742.

105. Lombardi, J.R., et al., *Charge-transfer theory of surface enhanced Raman-spectroscopy - Herzberg-Teller contributions.* Journal of Chemical Physics, 1986. **84**(8): p. 4174-4180.

106. Maier, S.A., et al., *Observation of near-field coupling in metal nanoparticle chains using far-field polarization spectroscopy.* Physical Review B, 2002. **65**(19): p. 193408.

107. Willingham, B. and S. Link, *Energy transport in metal nanoparticle chains via sub-radiant plasmon modes.* Optics Express, 2011. **19**(7): p. 6450-6461.

108. McQuillan, A.J., *The Discovery of surface-enhanced Raman scattering.* Notes and Records of the Royal Society, 2009. **63**(1): p. 105-109.

109. Le Ru, E.C. and P.G. Etchegoin, *Chapter 4 - SERS enhancement factors and related topics*, in *Principles of Surface-Enhanced Raman Spectroscopy*, E.C. Le Ru and P.G. Etchegoin, Editors. 2009, Elsevier: Amsterdam. p. 185-264.

110. Blackie, E.J., E.C. Le Ru, and P.G. Etchegoin, *Single-molecule surface-enhanced Raman spectroscopy of nonresonant molecules.* Journal of the American Chemical Society, 2009. **131**(40): p. 14466-14472.

111. Kalkan, A.K. and S.J. Fonash, *Laser-activated surface-enhanced Raman scattering substrates capable of single molecule detection.* Applied Physics Letters, 2006. **89**(23).

112. Singhal, K. and A.K. Kalkan, *Surface-enhanced Raman scattering captures conformational changes of single photoactive yellow protein molecules under photoexcitation.* Journal of the American Chemical Society, 2010. **132**(2): p. 429-31.

113. Ç. Ö, T. and A.K. Kalkan. *Isomerization in single molecules of azobenzene probed by surface-enhanced Raman scattering*. in *2011 11th IEEE International Conference on Nanotechnology*. 2011.

114. Shafayet, K.M., *Conformational states and transitions in green fluorescent protein chromophore studied by single molecule SERS*, in *Mechanical and Aerospace Engineering*. 2011, Oklahoma State University: Stillwater, OK.

115. Craggs, T.D., *Green fluorescent protein: structure, folding and chromophore maturation.* Chemical Society Reviews, 2009. **38**(10): p. 2865-2875.

116. Maddalo, S.L. and M. Zimmer, *The Role of the protein matrix in green fluorescent protein fluorescence.* Photochemistry and Photobiology, 2006. **82**(2): p. 367-372.

117. Meech, S.R., *Excited state reactions in fluorescent proteins.* Chemical Society Reviews, 2009. **38**(10): p. 2922-2934.

118. Nifosi, R., et al., *Photoreversible dark state in a tristable green fluorescent protein variant.* Journal of Physical Chemistry B, 2003. **107**(7): p. 1679-1684.

119. Seward, H.E. and C.R. Bagshaw, *The photochemistry of fluorescent proteins: Implications for their biological applications.* Chemical Society Reviews, 2009. **38**(10): p. 2842-2851.

120. van Thor, J.J., *Photoreactions and dynamics of the green fluorescent protein.* Chemical Society Reviews, 2009. **38**(10): p. 2935-2950.

121. Weber, W., et al., *Shedding light on the dark and weakly fluorescent states of green fluorescent proteins.* Proceedings of the National Academy of Sciences of the United States of America, 1999. **96**(11): p. 6177-6182.

122. Chattoraj, M., et al., *Ultra-fast excited state dynamics in green fluorescent protein: Multiple states and proton transfer.* Proceedings of the National Academy of Sciences of the United States of America, 1996. **93**(16): p. 8362-8367.

123. Lossau, H., et al., *Time-resolved spectroscopy of wild-type and mutant green fluorescent proteins reveals excited state deprotonation consistent with fluorophore-protein interactions.* Chemical Physics, 1996. **213**(1-3): p. 1-16.

124. Nie, S. and S.R. Emory, *Probing single molecules and single nanoparticles by surface-enhanced Raman scattering.* Science, 1997. **275**(5303): p. 1102-6.

125. Kneipp, K., et al., *Single molecule detection using surface-enhanced Raman scattering (SERS).* Physical Review Letters, 1997. **78**(9): p. 1667-1670.

126. Bjerneld, E.J., et al., *Single-molecule surface-enhanced Raman and fluorescence correlation spectroscopy of horseradish peroxidase.* The Journal of Physical Chemistry B, 2002. **106**(6): p. 1213-1218.

127. Dieringer, J.A., et al., *A frequency domain existence proof of single-molecule surface-enhanced Raman Spectroscopy.* Journal of the American Chemical Society, 2007. **129**(51): p. 16249-16256.

128. Ishikawa, M., et al., *Single-molecule imaging and spectroscopy of adenine and an analog of adenine using surface-enhanced Raman scattering and fluorescence.* Journal of Luminescence, 2002. **98**(1-4): p. 81-89.

129. Michaels, A.M., J. Jiang, and L. Brus, *Ag nanocrystal junctions as the site for surface-enhanced Raman scattering of single Rhodamine 6G molecules.* Journal of Physical Chemistry B, 2000. **104**(50): p. 11965-11971.

130. Vosgrone, T. and A.J. Meixner, *Surface and resonance enhanced micro-Raman spectroscopy of xanthene dyes at the single-molecule level.* Journal of Luminescence, 2004. **107**(1-4): p. 13-20.

131. Xu, H., et al., *Spectroscopy of single hemoglobin molecules by surface enhanced Raman scattering.* Physical Review Letters, 1999. **83**(21): p. 4357-4360.

132. Habuchi, S., et al., *Single-molecule surface enhanced resonance Raman spectroscopy of the enhanced green fluorescent protein.* Journal of the American Chemical Society, 2003. **125**(28): p. 8446-8447.

133. Cortés, E., et al., *Monitoring the electrochemistry of single molecules by surface-enhanced Raman spectroscopy.* Journal of the American Chemical Society, 2010. **132**(51): p. 18034-18037.

134. Fu, B., et al., *Single molecule electrochemistry: impact of surface site heterogeneity.* The Journal of Physical Chemistry C, 2016. **120**(48): p. 27241-27249.

135. Santos, D.P.d., et al., *Electrochemical control of the time-dependent intensity fluctuations in surface-enhanced Raman scattering (SERS).* The Journal of Physical Chemistry C, 2009. **113**(41): p. 17737-17744.

136. Shegai, T., et al., *Raman spectroelectrochemistry of molecules within individual electromagnetic hot spots.* Journal of the American Chemical Society, 2009. **131**(40): p. 14390-14398.

137. Wang, Y., et al., *Probing ground-state single-electron self-exchange across a molecule−metal interface.* Journal of the American Chemical Society, 2011. **133**(18): p. 6989-6996.

138. Weber, M.L., A.J. Wilson, and K.A. Willets, *Characterizing the spatial dependence of redox chemistry on plasmonic nanoparticle electrodes using correlated super-resolution surface-enhanced Raman scattering imaging and electron microscopy.* The Journal of Physical Chemistry C, 2015. **119**(32): p. 18591-18601.

139. Wilson, A.J. and K.A. Willets, *Visualizing site-specific redox potentials on the surface of plasmonic nanoparticle aggregates with superlocalization SERS microscopy.* Nano Letters, 2014. **14**(2): p. 939-945.

140. Zaleski, S., et al., *Observing single, heterogeneous, one-electron transfer reactions.* The Journal of Physical Chemistry C, 2015. **119**(50): p. 28226-28234.

141. Choi, H.-K., et al., *Metal-catalyzed chemical reaction of single molecules directly probed by vibrational spectroscopy.* Journal of the American Chemical Society, 2016. **138**(13): p. 4673-4684.

142. Zhang, Z., et al., *Single molecule level plasmonic catalysis - a dilution study of p-nitrothiophenol on gold dimers.* Chemical Communications, 2015. **51**(15): p. 3069-3072.

143. *Single-Molecule Raman Spectroscopy - Fact or Fiction?* CHIMIA International Journal for Chemistry, 1999. **53**(1-2): p. 35-37.

144. Le Ru, E.C. and P.G. Etchegoin, *Chapter 8 - Recent developments*, in *Principles of Surface-Enhanced Raman Spectroscopy*, E.C. Le Ru and P.G. Etchegoin, Editors. 2009, Elsevier: Amsterdam. p. 415-464.

145. Le Ru, E.C., M. Meyer, and P.G. Etchegoin, *Proof of single-molecule sensitivity in surface enhanced Raman scattering (SERS) by means of a two-analyte technique.* The Journal of Physical Chemistry B, 2006. **110**(4): p. 1944-8.

146. Habuchi, S., et al., *Single-molecule surface enhanced resonance Raman spectroscopy of the enhanced green fluorescent protein.* Journal of the American Chemical Society, 2003. **125**(28): p. 8446-7.

147. Le Ru, E.C.E.P.G., *Principles of surface-enhanced Raman spectroscopy : and related plasmonic effects*. 1st ed. 2009: Boston.

148. Nie, S.M. and S.R. Emery, *Probing single molecules and single nanoparticles by surface-enhanced Raman scattering.* Science, 1997. **275**(5303): p. 1102-1106.

149. Weiss, A. and G. Haran, *Time-dependent single-molecule Raman scattering as a probe of surface dynamics.* Journal of Physical Chemistry B, 2001. **105**(49): p. 12348-12354.

150. Jiang, et al., *Single molecule Raman spectroscopy at the junctions of large Ag nanocrystals.* The Journal of Physical Chemistry B, 2003. **107**(37): p. 9964-9972.

151. Shegai, T.O. and G. Haran, *Probing the Raman scattering tensors of individual molecules.* The Journal of Physical Chemistry B, 2006. **110**(6): p. 2459-2461.

152. Sawai, Y., et al., *Observation of a small number of molecules at a metal nanogap arrayed on a solid surface using surface-enhanced Raman scattering.* Journal of the American Chemical Society, 2007. **129**(6): p. 1658-1662.

153. Goulet, P.J.G. and R.F. Aroca, *Distinguishing individual vibrational fingerprints: Single-molecule surface-enhanced resonance Raman scattering from one-to-one binary mixtures in Langmuir−Blodgett monolayers.* Analytical Chemistry, 2007. **79**(7): p. 2728-2734.

154. Etchegoin, P.G. and E.C. Le Ru, *Resolving single molecules in surface-enhanced Raman scattering within the inhomogeneous broadening of Raman peaks.* Analytical Chemistry, 2010. **82**(7): p. 2888-2892.

155. Bosnick, K.A., Jiang, and L.E. Brus, *Fluctuations and local symmetry in single-molecule rhodamine 6G Raman scattering on silver nanocrystal aggregates.* The Journal of Physical Chemistry B, 2002. **106**(33): p. 8096-8099.

156. Emory, S.R., et al., *Re-examining the origins of spectral blinking in single-molecule and single-nanoparticle SERS.* Faraday Discussions, 2006. **132**(0): p. 249-259.

157. Futamata, M., Y. Maruyama, and M. Ishikawa, *Adsorbed sites of individual molecules on Ag nanoparticles in single molecule sensitivity surface-enhanced Raman scattering.* The Journal of Physical Chemistry B, 2004. **108**(35): p. 13119-13127.

158. Chen, C., et al., *Direct evidence of high spatial localization of hot spots in surface-enhanced Raman scattering.* Angewandte Chemie International Edition, 2009. **48**(52): p. 9932-9935.

159. Le Ru, E.C. and P.G. Etchegoin, *Sub-wavelength localization of hot-spots in SERS.* Chemical Physics Letters, 2004. **396**(4): p. 393-397.

160. Tsai, D.P., et al., *Photon scanning tunneling microscopy images of optical excitations of fractal metal colloid clusters.* Physical Review Letters, 1994. **72**(26): p. 4149-4152.

161. Zhang, P., et al., *Mode localization in self-affine fractal interfaces observed by near-field microscopy*. Physical Review B, 1998. **57**(24): p. 15513-15518.

162. Kudelski, A. and B. Pettinger, *SERS on carbon chain segments: monitoring locally surface chemistry.* Chemical Physics Letters, 2000. **321**(5): p. 356-362.

163. Sharaabi, Y., T. Shegai, and G. Haran, *Two-state analysis of single-molecule Raman spectra of crystal violet.* Chemical Physics, 2005. **318**(1-2): p. 44-49.

164. Barmparis, G.D.L., Z.; Lopez, N.; Remediakis, I. N., *Nanoparticle shapes by using Wulff constructions and first-principles calculations.* Beilstein Journal of Nanotechnology, 2015. **6**: p. 361-368.

165. Hansen, T.W., et al., *Atomic-resolution in situ transmission electron microscopy of a promoter of a heterogeneous catalyst.* Science, 2001. **294**(5546): p. 1508-1510.

166. Sun, Y. and Y. Xia, *Shape-controlled synthesis of gold and silver nanoparticles.* Science, 2002. **298**(5601): p. 2176.

167. Hu, J., et al., *Effects of atomic geometry and electronic structure of platinum surfaces on molecular adsorbates studied by gap-mode SERS.* Journal of the American Chemical Society, 2014. **136**(29): p. 10299-10307.

168. Ikeda, K., et al., *Plasmonic enhancement of Raman scattering on non-SERS-active platinum substrates.* Journal of Physical Chemistry C, 2009. **113**(27): p. 11816-11821.

169. Ikeda, K., J. Sato, and K. Uosaki, *Surface-enhanced Raman scattering at well-defined single crystalline faces of platinum-group metals induced by gap-mode plasmon excitation.* Journal of Photochemistry and Photobiology A: Chemistry, 2011. **221**(2-3): p. 175-180.

170. Ikeda, K., S. Suzuki, and K. Uosaki, *Crystal face dependent chemical effects in surface-enhanced Raman scattering at atomically defined gold facets.* Nano Letters, 2011. **11**(4): p. 1716-1722.

171. Perdew, J.P., K. Burke, and M. Ernzerhof, *Generalized gradient approximation made simple.* Physical Review Letters, 1996. **77**(18): p. 3865-3868.

172. Grimme, S., et al., *A consistent and accurate ab initio parametrization of density functional dispersion correction (DFT-D) for the 94 elements H-Pu.* The Journal of Chemical Physics, 2010. **132**(15): p. 154104.

173. Blöchl, P.E., *Projector augmented-wave method.* Physical Review B, 1994. **50**(24): p. 17953-17979.

174. Vanderbilt, D., *Soft self-consistent pseudopotentials in a generalized eigenvalue formalism.* Physical Review B, 1990. **41**(11): p. 7892-7895.

175. Monkhorst, H.J. and J.D. Pack, *Special points for Brillouin-zone integrations.* Physical Review B, 1976. **13**(12): p. 5188-5192.

176. Armstrong, D.R., J. Clarkson, and W.E. Smith, *Vibrational analysis of trans-azobenzene.* Journal of Physical Chemistry, 1995. **99**(51): p. 17825-17831.

177. Biswas, N. and S. Umapathy, *Early time dynamics of trans-azobenzene isomerization in solution from resonance Raman intensity analysis.* Journal of Chemical Physics, 1997. **107**(19): p. 7849-7858.

178. Stuart, C.M., R.R. Frontiera, and R.A. Mathies, *Excited-state structure and dynamics of cis- and trans-azobenzene from resonance Raman intensity analysis.* Journal of Physical Chemistry A, 2007. **111**(48): p. 12072-12080.

179. Tecklenburg, M.M.J., et al., *Vibrational characterization of azobenzenes, azoxybenzenes and azoaromatic and azoxyaromatic polyethers.* Journal of Raman Spectroscopy, 1997. **28**(10): p. 755-763.

180. Galanakis, I., et al., *Broken-bond rule for the surface energies of noble metals.* Europhysics Letters, 2002. **58**(5): p. 751-757.

181. Galanakis, I., N. Papanikolaou, and P.H. Dederichs, *Applicability of the broken-bond rule to the surface energy of the FCC metals.* Surface Science, 2002. **511**(1-3): p. 1-12.

182. Michaelides, A. and M. Scheffler, *An Introduction to the Theory of Crystalline Elemental Solids and their Surfaces.* Surface and Interface Science, 2013.

183. Kellerer, B., J. Brandmuller, and H.H. Hacker, *Structure of azobenzene and tolane in solution - Raman spectra of azobenzene, azobenzene-D10, para-,para'-azobenzene-D2, azobenzene-N-15=N-15 and tolane.* Indian Journal of Pure & Applied Physics, 1971. **9**(11): p. 903.

184. Kubler, R., W. Luttke, and S. Weckherlin, *Infrarotspektroskopische untersuchungen an isotopen stickstoffverbindungen .1. Die lokalisierung der valenzfrequenz der N=N-doppelbindung.* Zeitschrift Fur Elektrochemie, 1960. **64**(5): p. 650-658.

185. Fliegl, H., et al., *Ab initio calculation of the vibrational and electronic spectra of trans- and cis-azobenzene.* Journal of the American Chemical Society, 2003. **125**(32): p. 9821-9827.

186. McNellis, E., et al., *Stabilizing a molecular switch at solid surfaces: A density functional theory study of azobenzene on Cu(111), Ag(111), and Au(111).* Physical Review B, 2009. **80**(3): p. 035414.

187. Mercurio, G., et al., *Structure and energetics of azobenzene on Ag(111): benchmarking semiempirical dispersion correction approaches.* Physical Review Letters 2010. **104**(3): p. 036102.

188. McNellis, E.R., J. Meyer, and K. Reuter, *Azobenzene at coinage metal surfaces: Role of dispersive van der Waals interactions.* Physical Review B, 2009. **80**(20): p. 205414.

APPENDICES

Additional SM-SERS Jumps

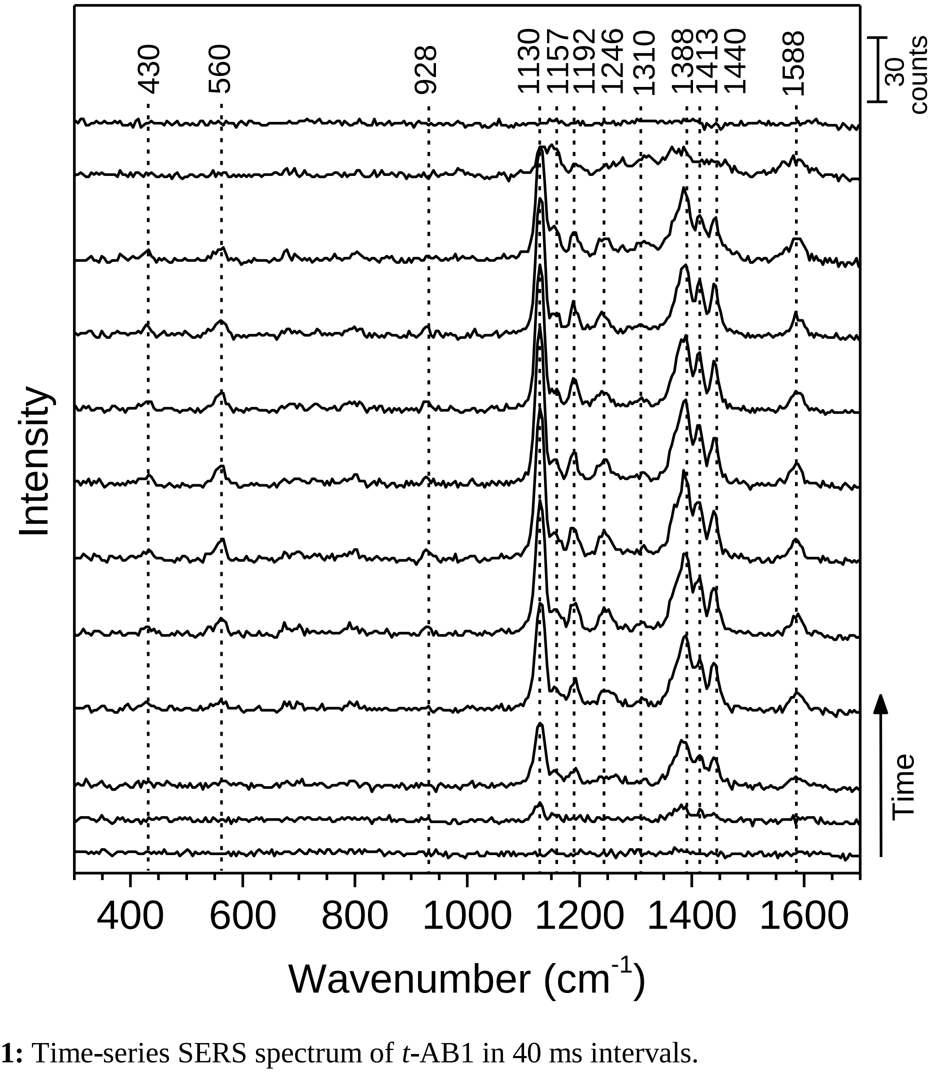

Figure A1: Time-series SERS spectrum of *t*-AB1 in 40 ms intervals.

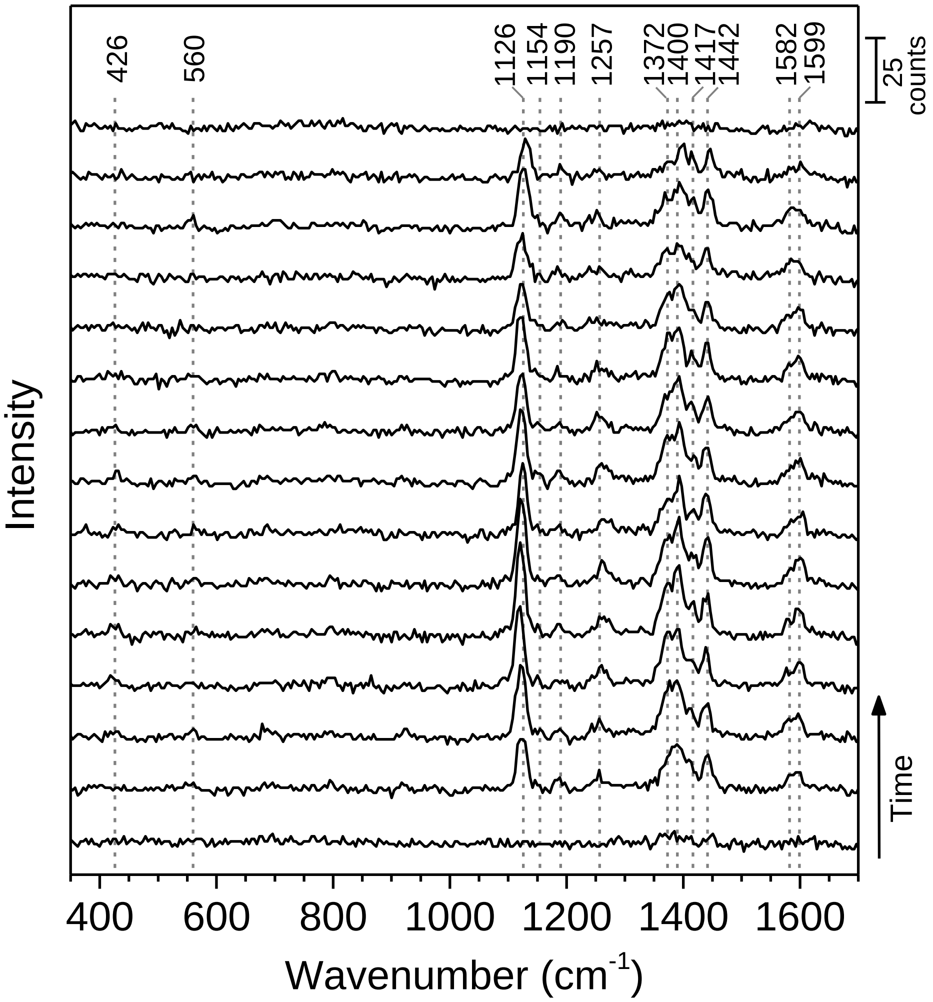

Figure A2: Time-series SERS spectrum of *t*-AB1 in 40 ms intervals.

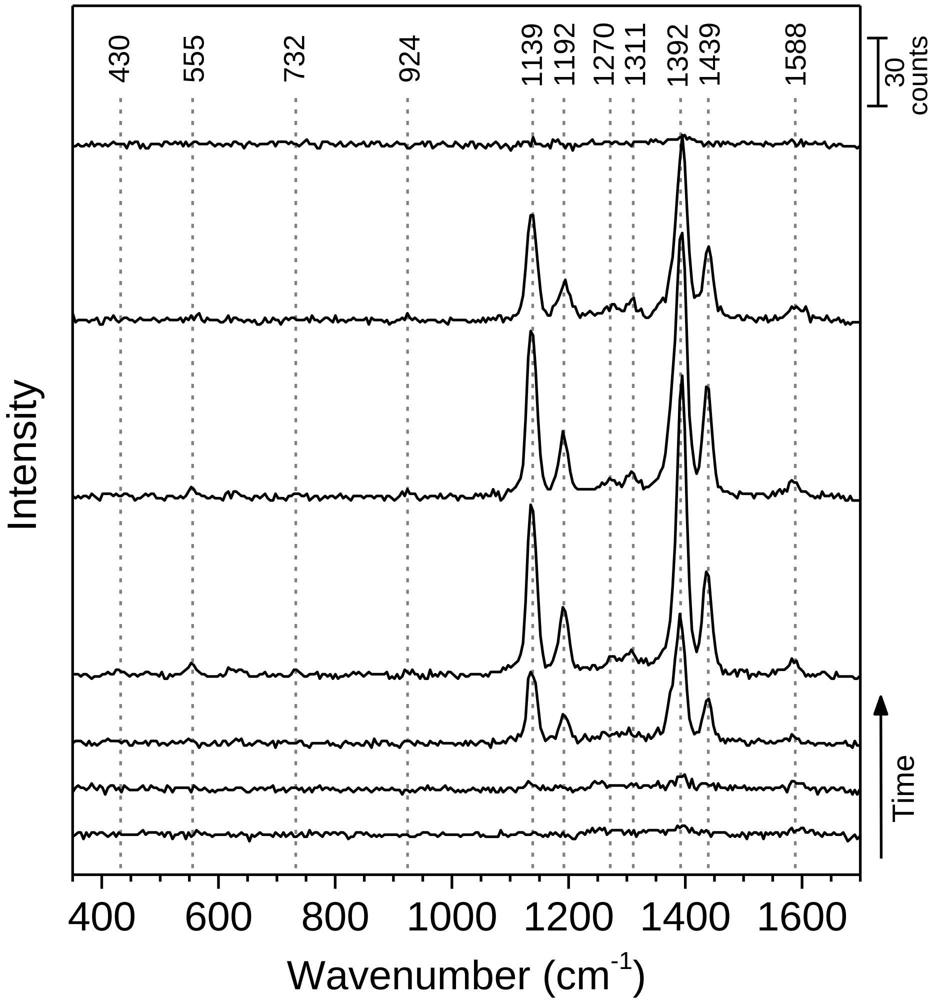

Figure A3: Time-series SERS spectrum of *t*-AB1 in 40 ms intervals.

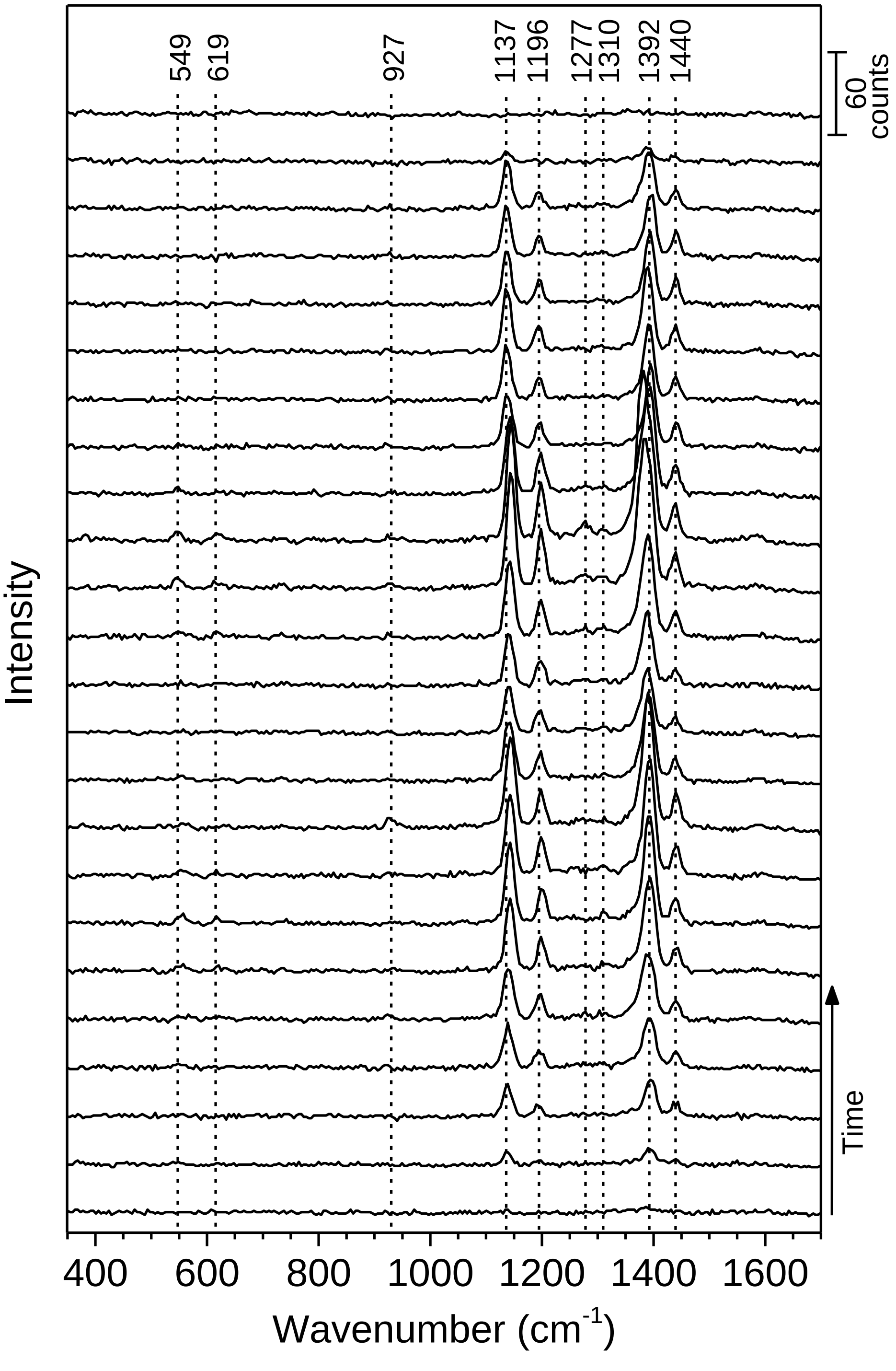

Figure A4: Time-series SERS spectrum of *t*-AB1 in 40 ms intervals.

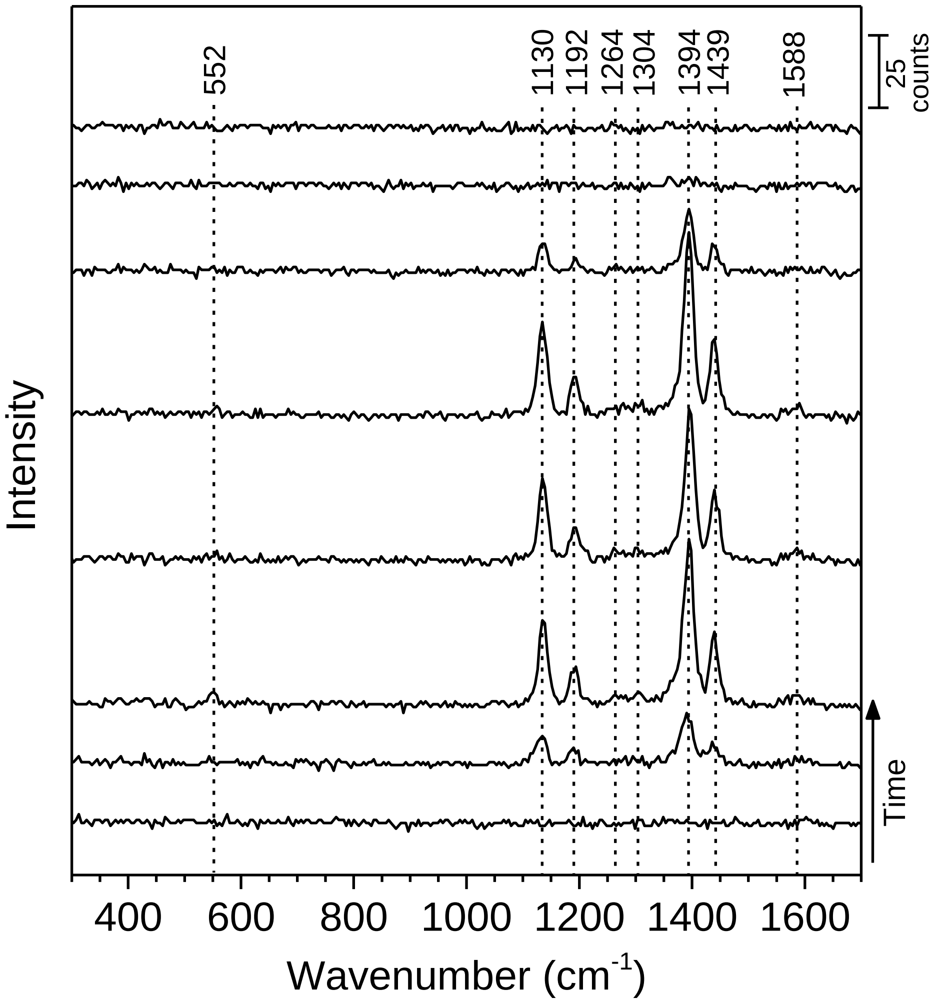

Figure A5: Time-series SERS spectrum of *t*-AB1 in 40 ms intervals.

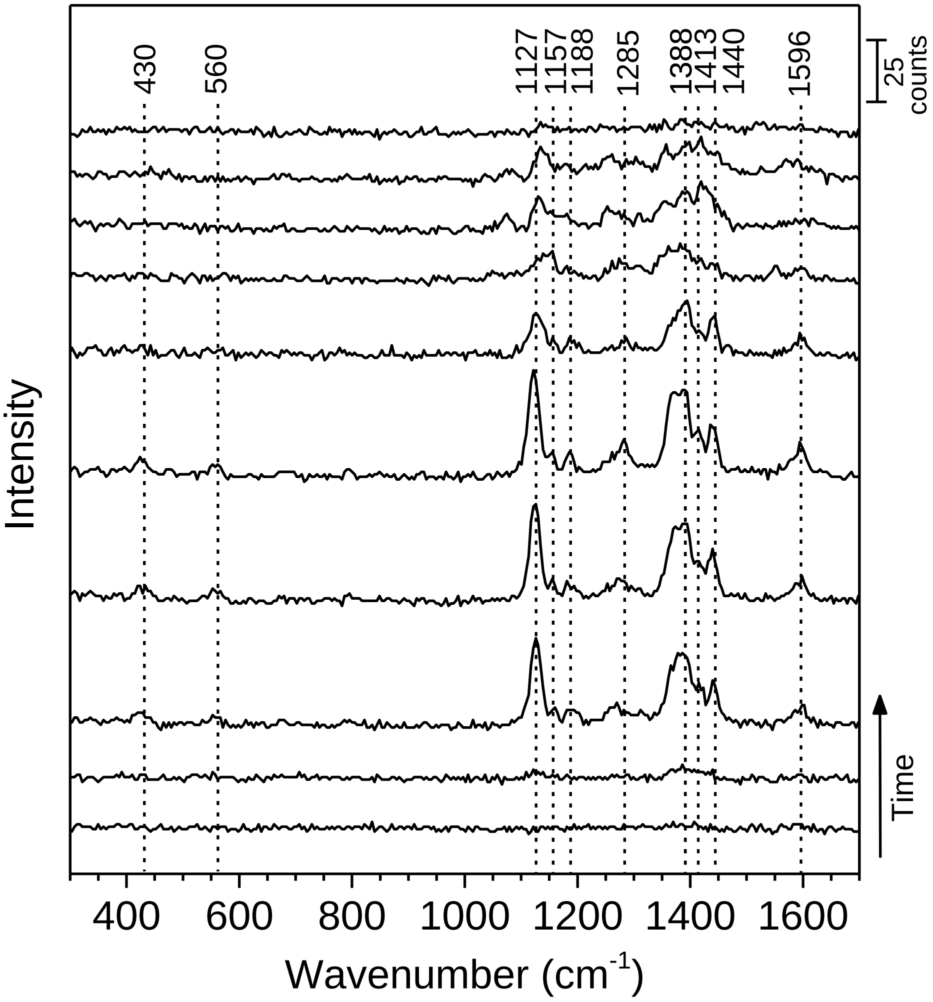

Figure A6: Time-series SERS spectrum of *t*-AB1 in 40 ms intervals.

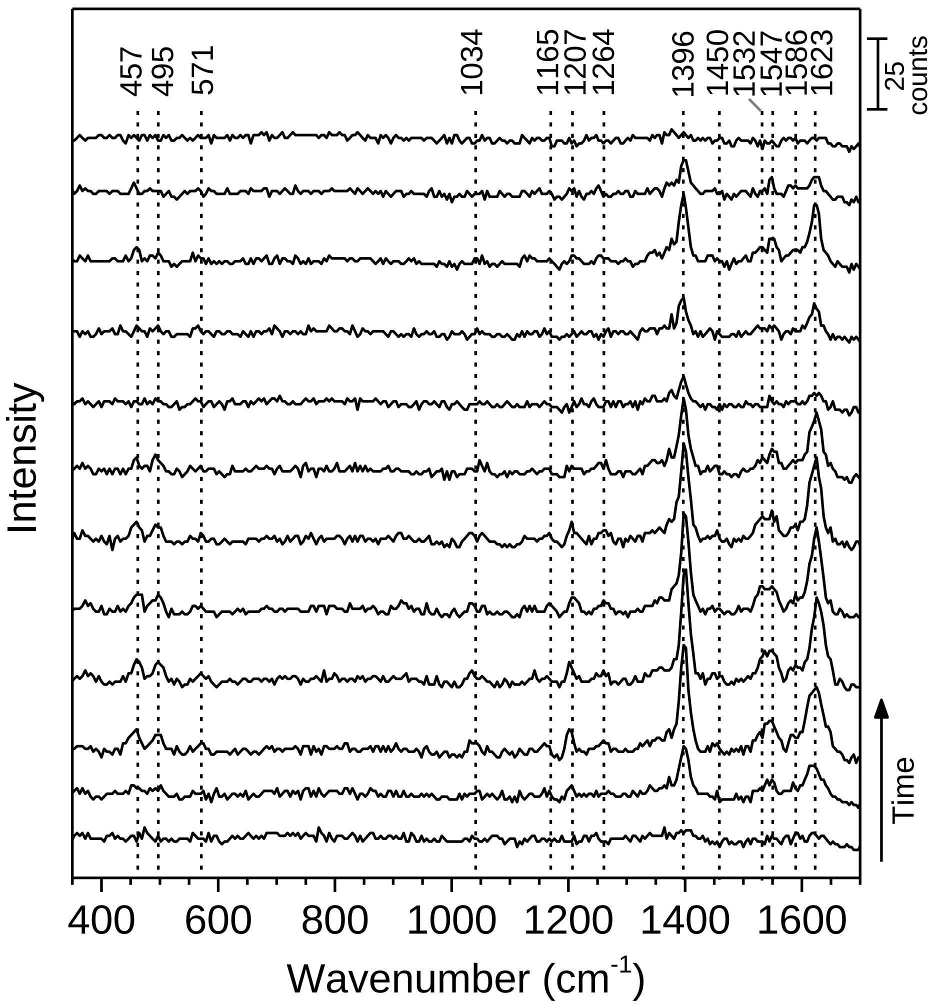

Figure A7: Time-series SERS spectrum of *t*-AB2 in 40 ms intervals.

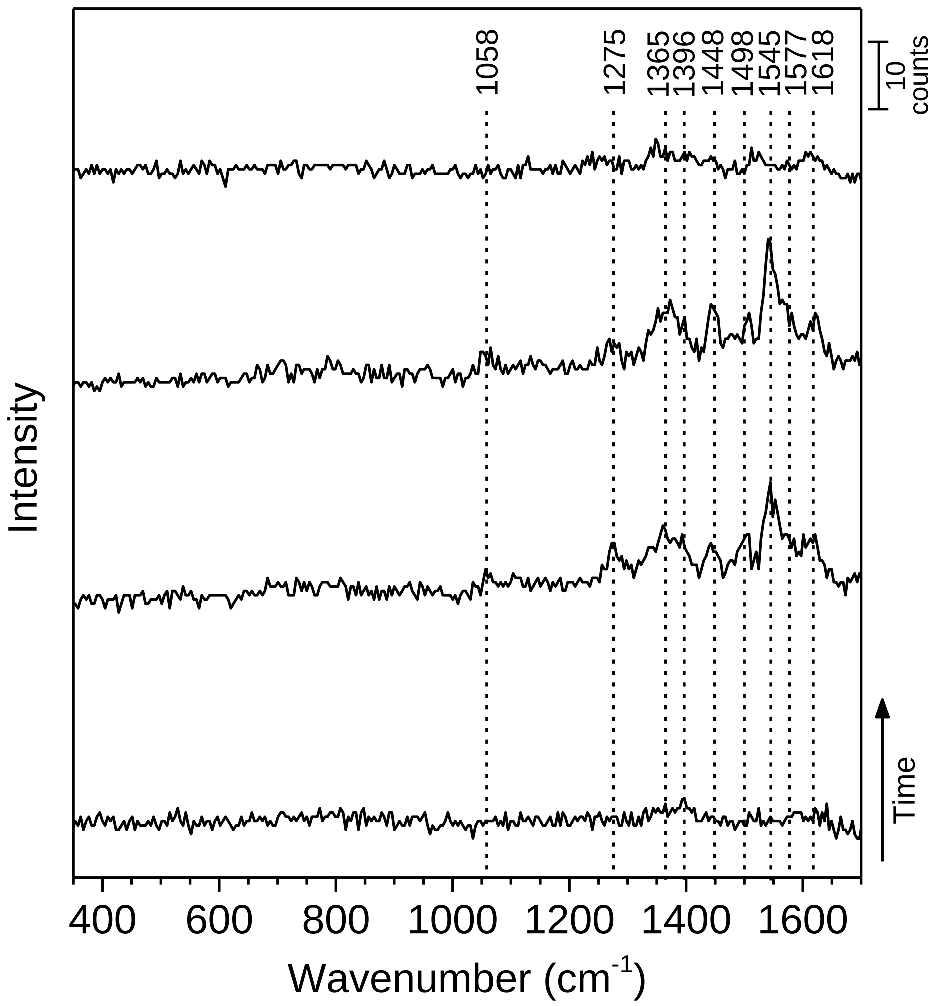

Figure A8: Time-series SERS spectrum of *t*-AB2 in 40 ms intervals.

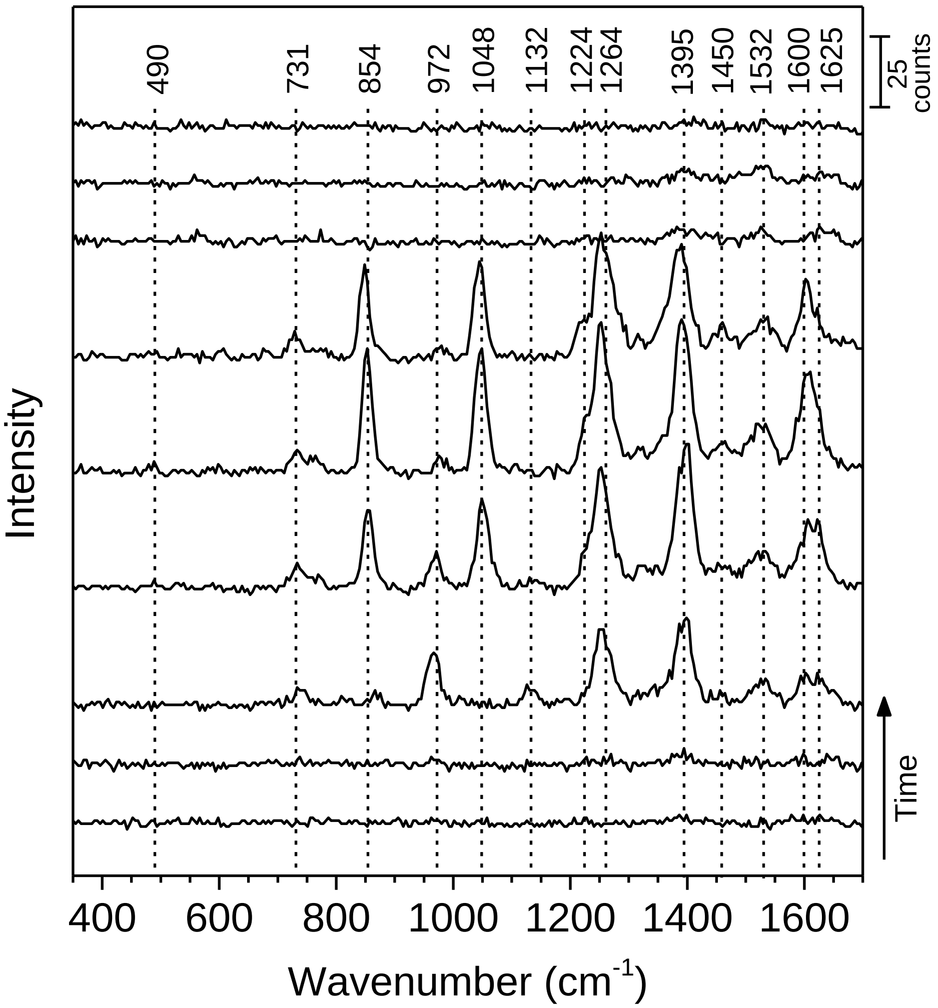

Figure A9: Time-series SERS spectrum of *t*-AB2 in 40 ms intervals.

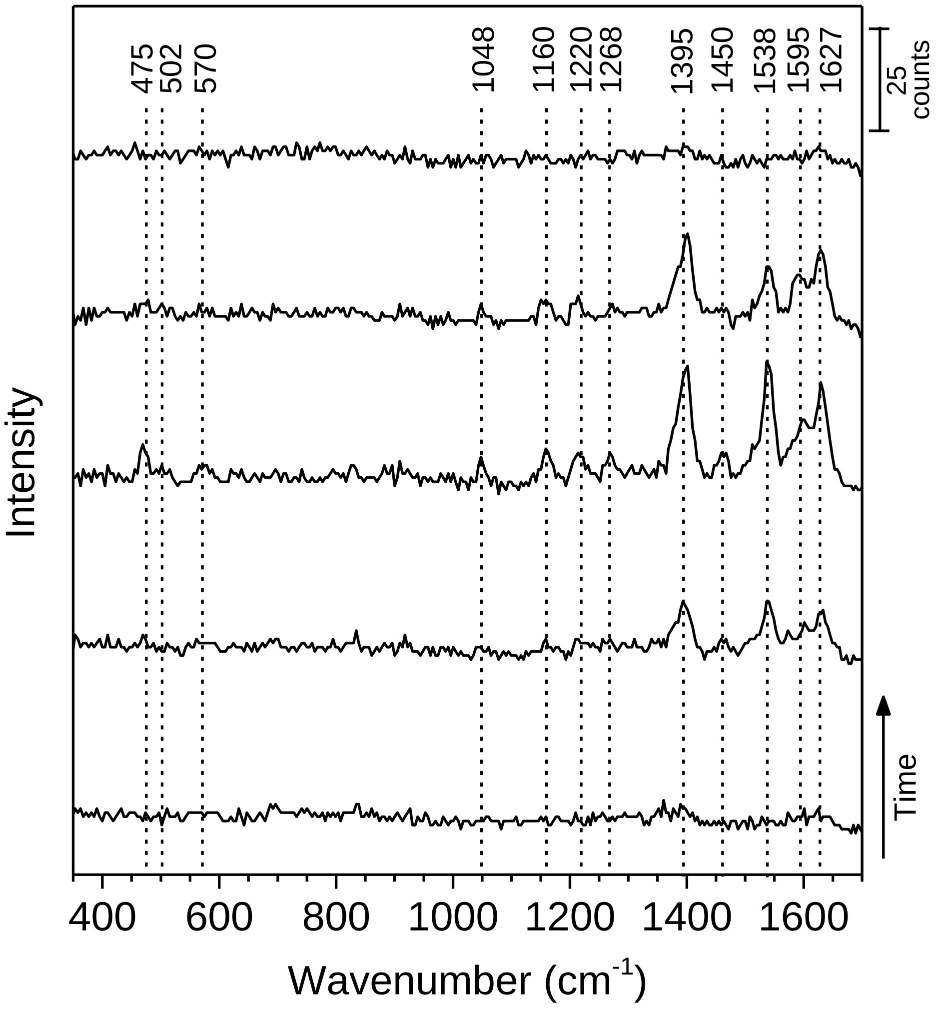

Figure A10: Time-series SERS spectrum of *t*-AB2 in 40 ms intervals.

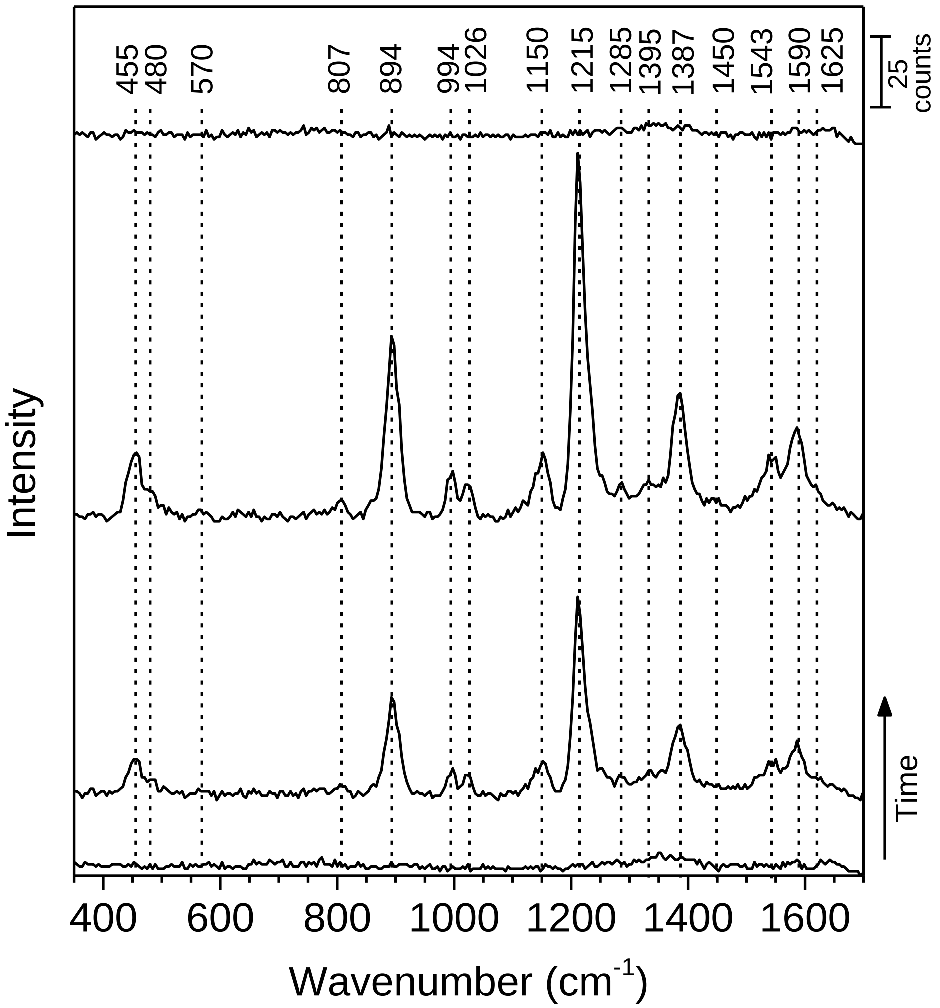

Figure A11: Time-series SERS spectrum of *t*-AB2 in 40 ms intervals.

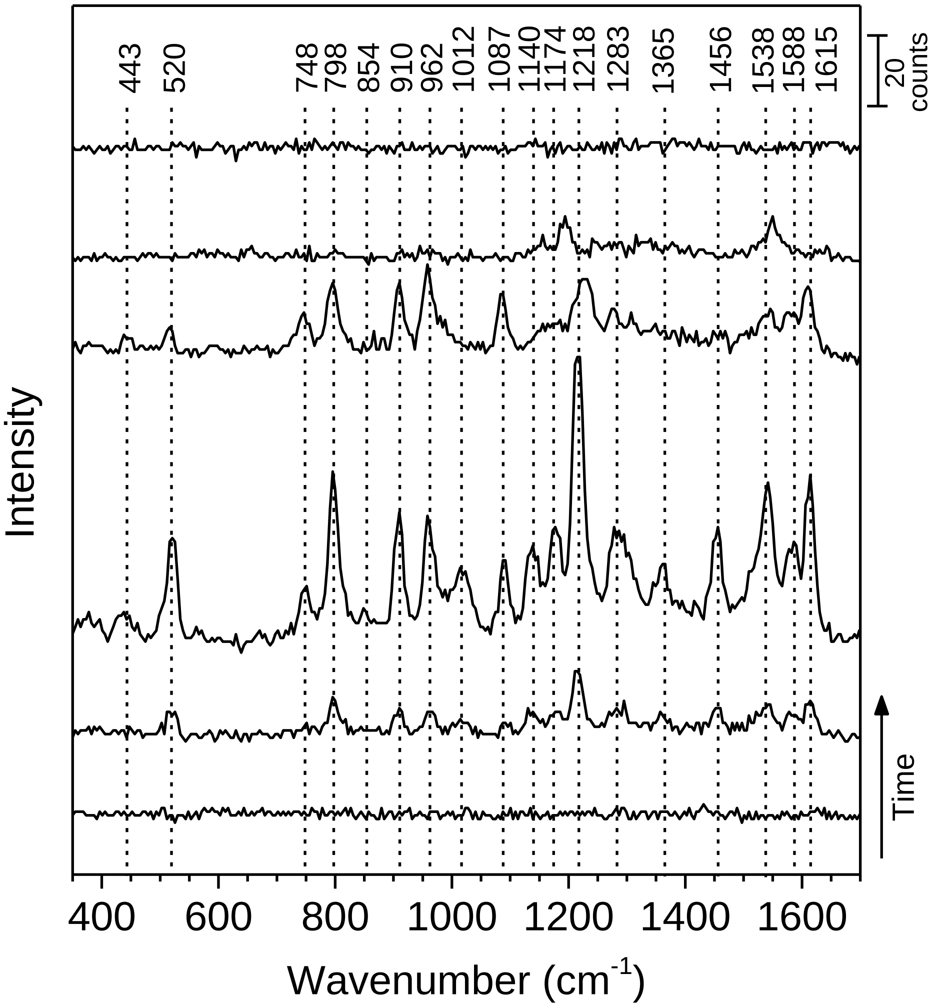

Figure A12: Time-series SERS spectrum of *t*-AB2 in 40 ms intervals.

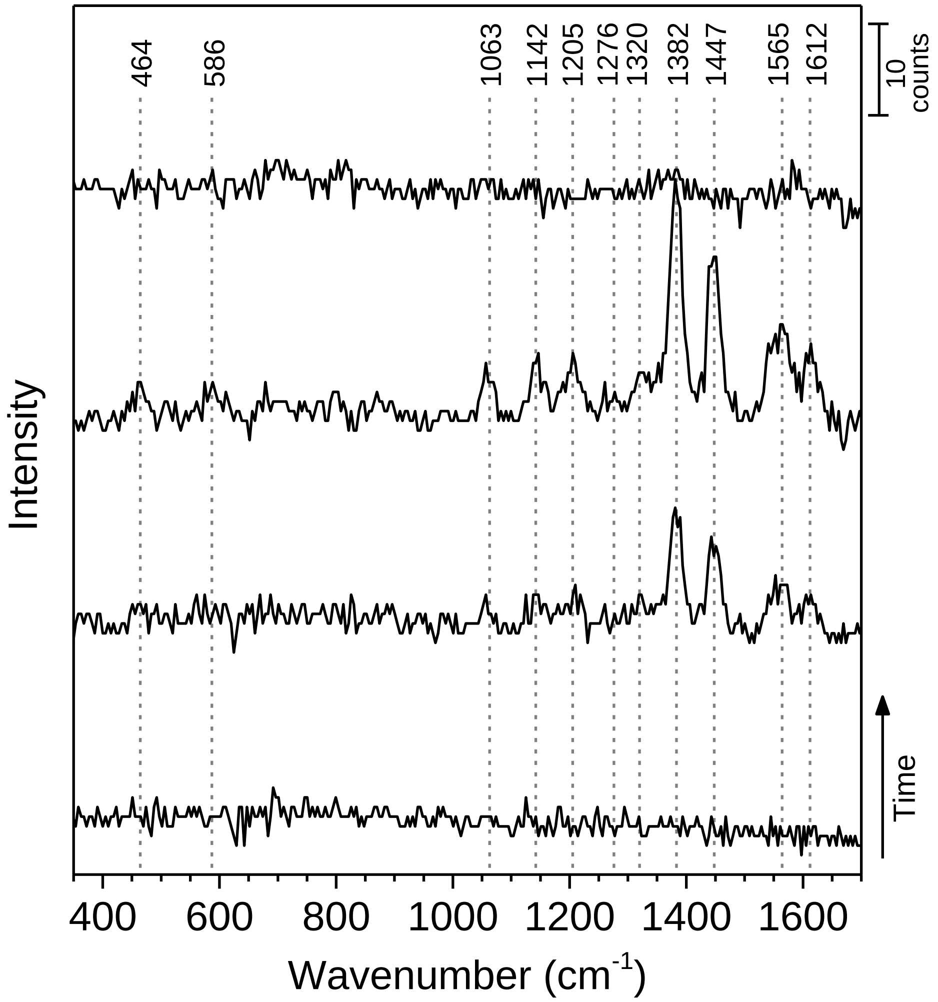

Figure A13: Time-series SERS spectrum of *t*-AB3 in 40 ms intervals.

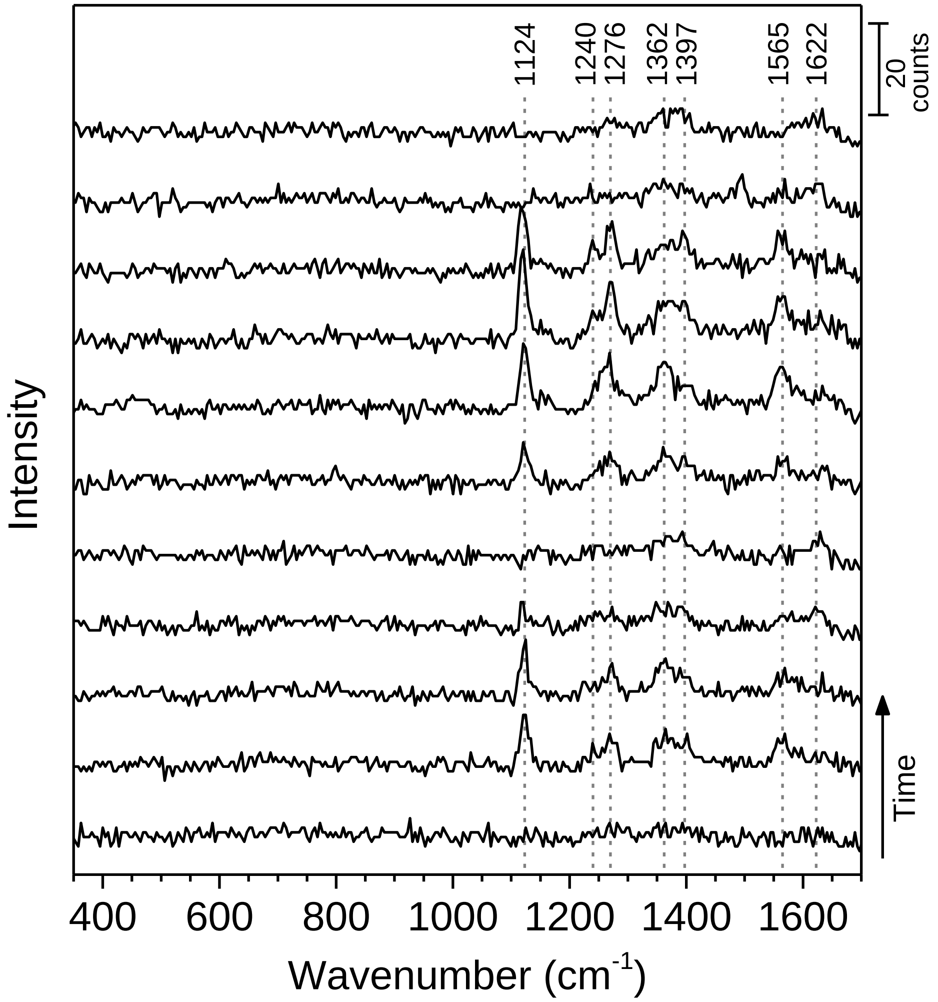

Figure A14: Time-series SERS spectrum of *t*-AB3 in 40 ms intervals.

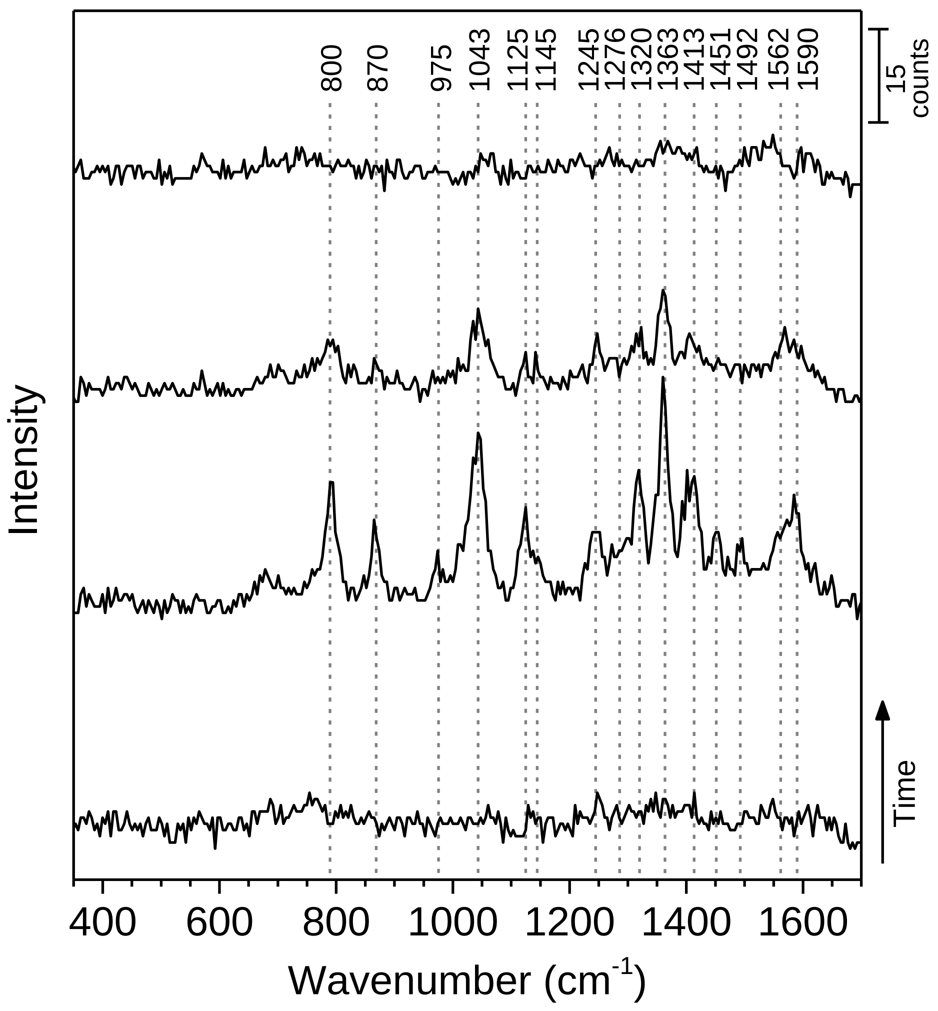

Figure A15: Time-series SERS spectrum of *t*-AB3 in 40 ms intervals.

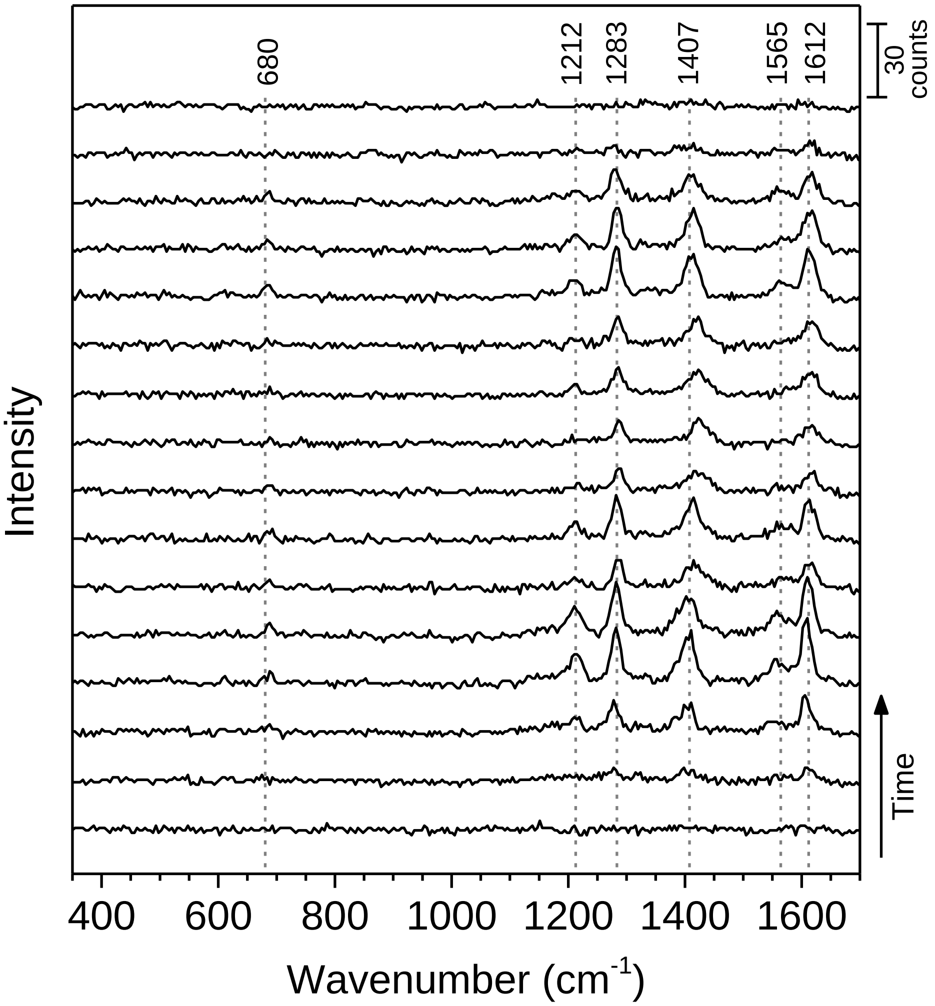

Figure A16: Time-series SERS spectrum of *t*-AB3 in 40 ms intervals.

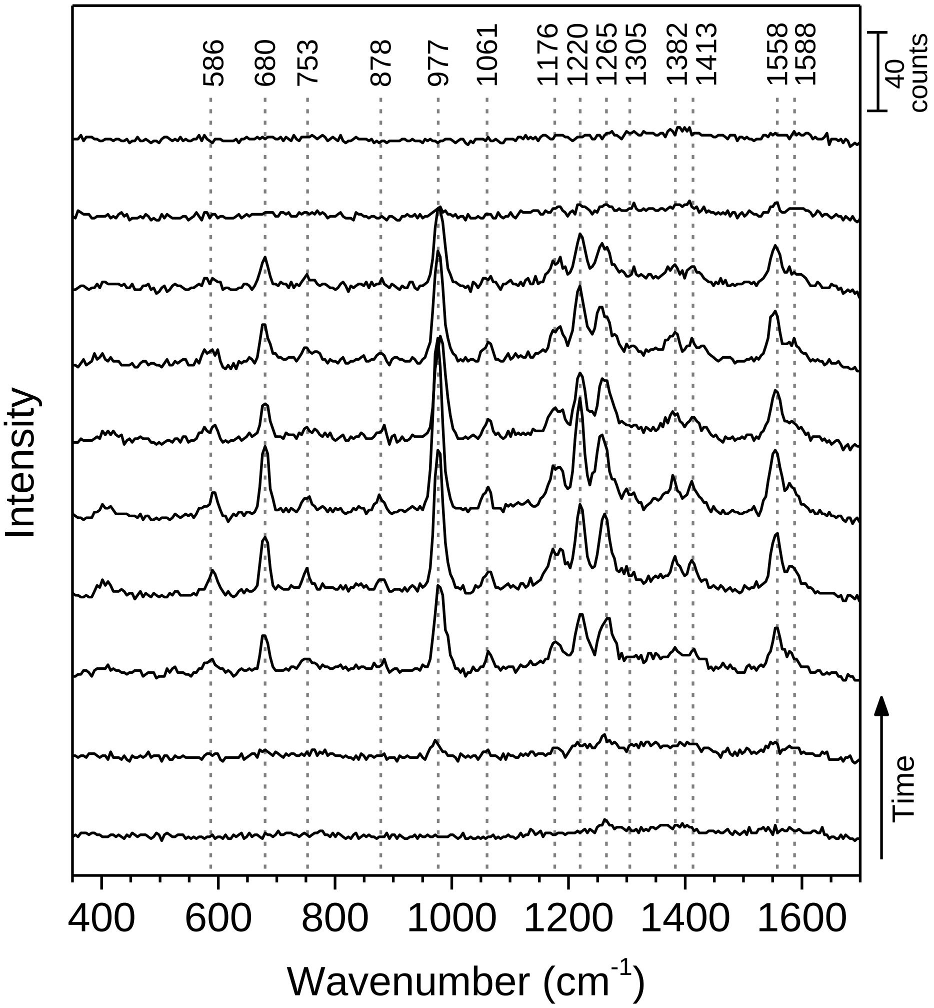

Figure A17: Time-series SERS spectrum of *t*-AB3 in 40 ms intervals.

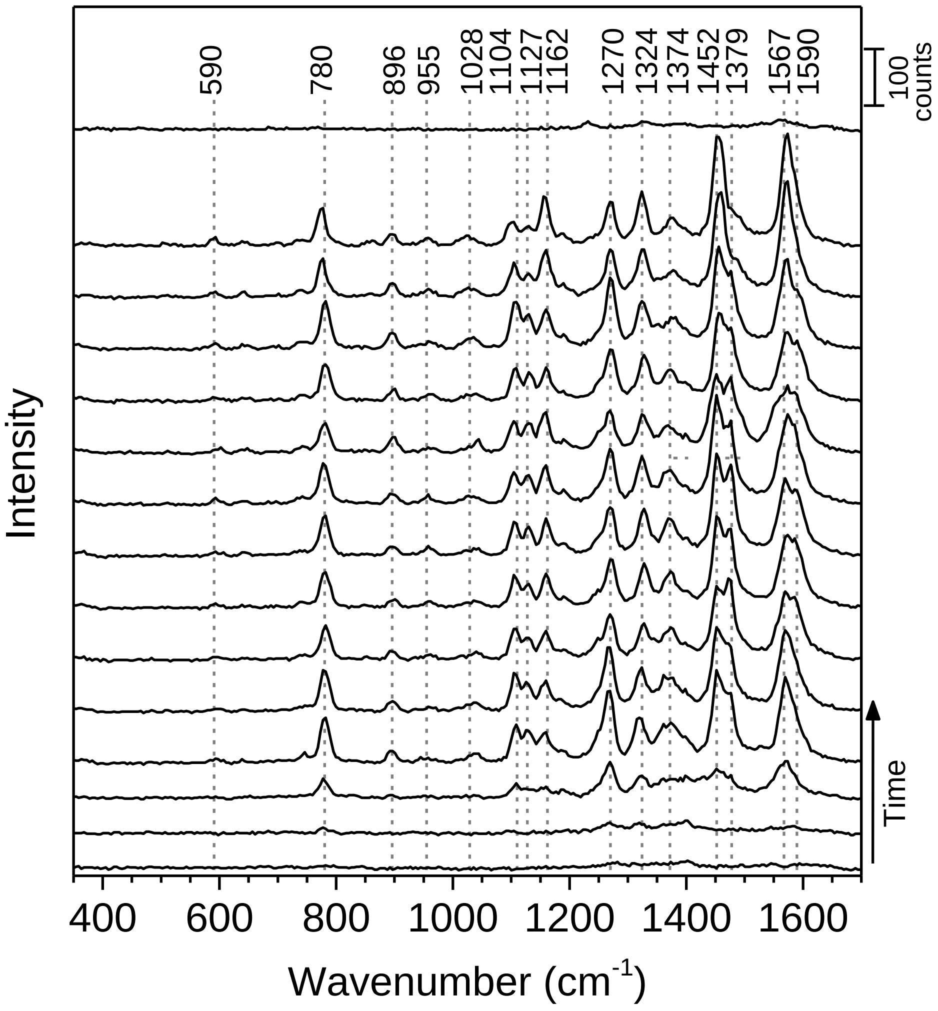

Figure A18: Time-series SERS spectrum of *t*-AB3 in 40 ms intervals.

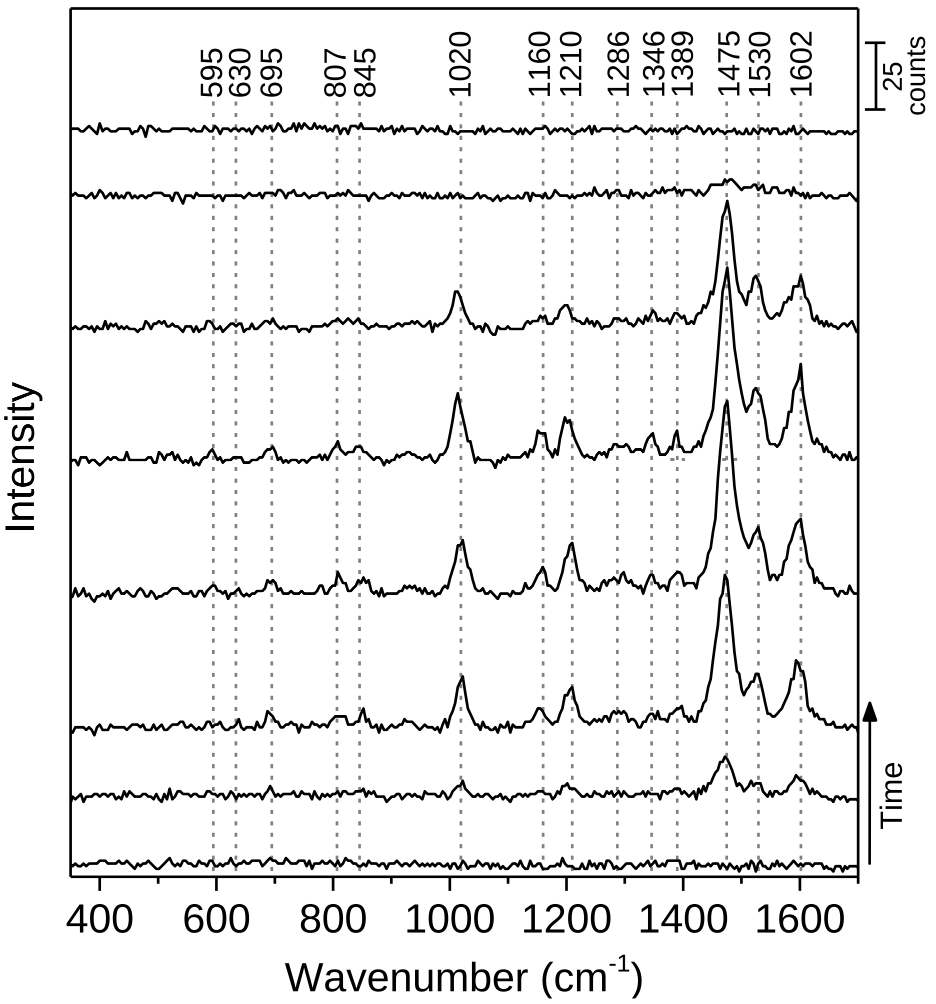

Figure A19: Time-series SERS spectrum of *c*-AB1 in 40 ms intervals.

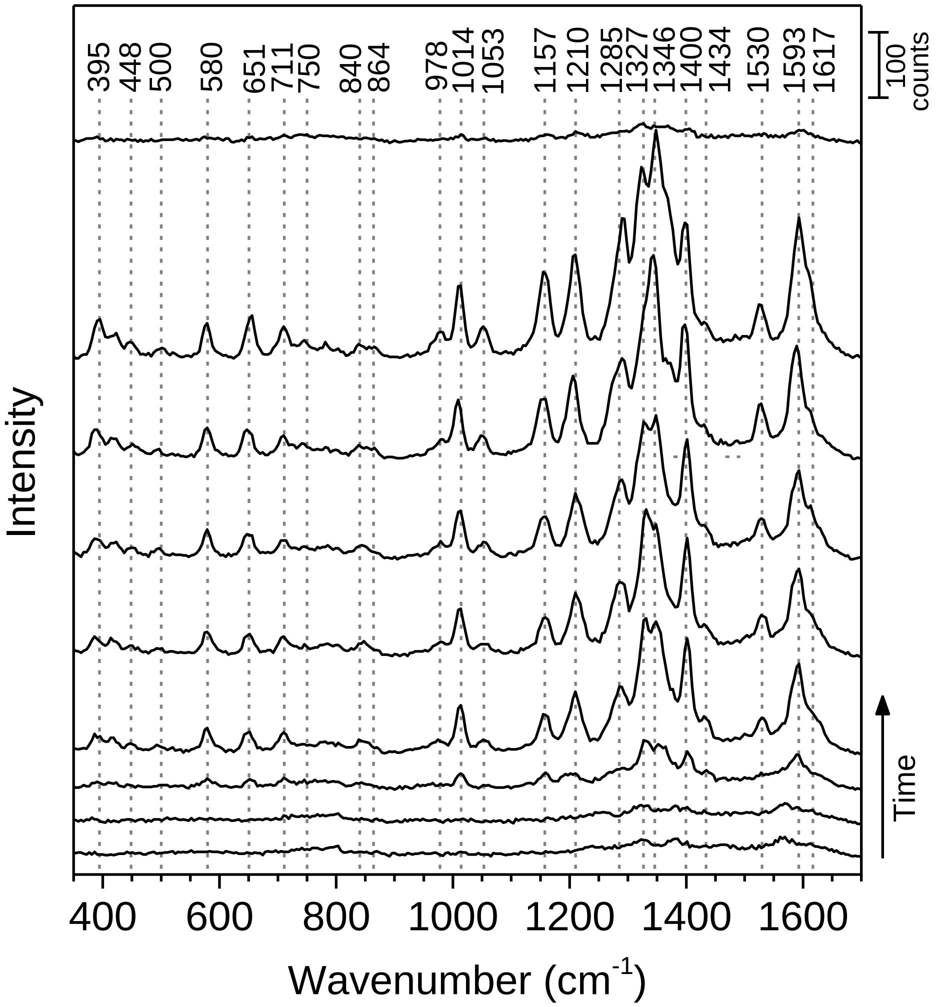

Figure A20: Time-series SERS spectrum of *c*-AB1 in 40 ms intervals.

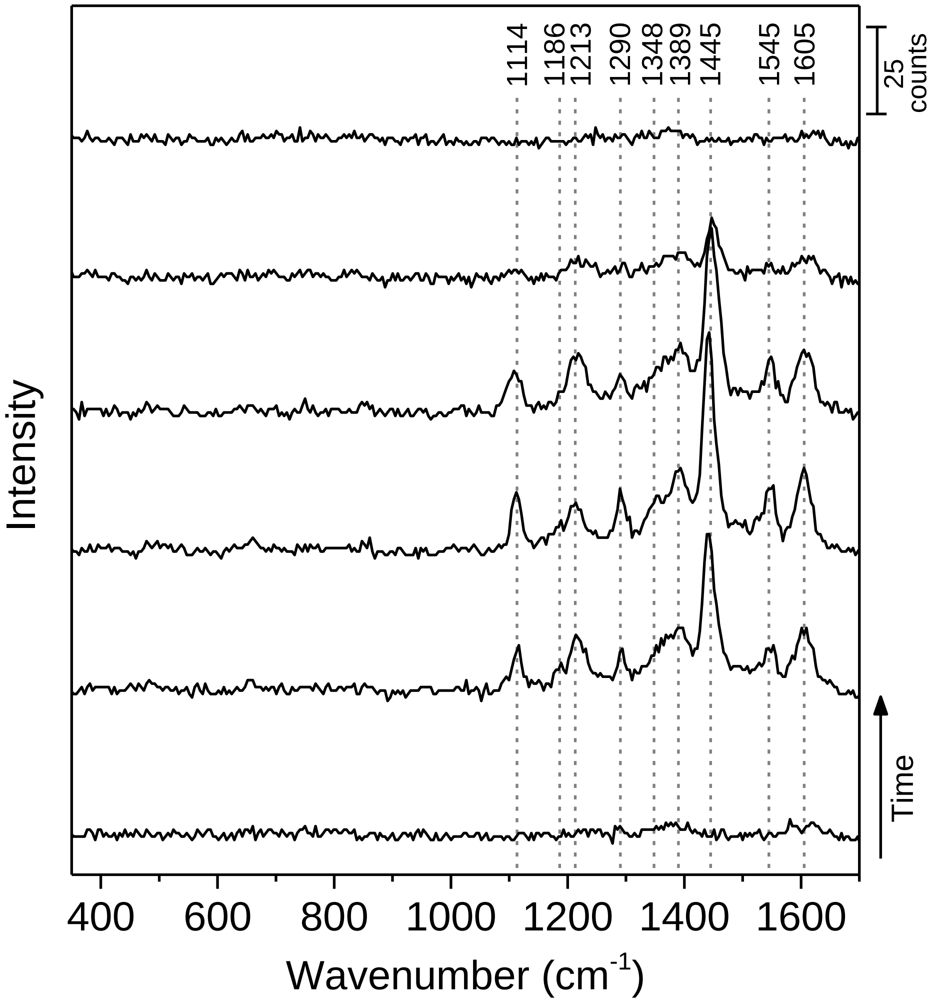

Figure A21: Time-series SERS spectrum of *c*-AB1 in 40 ms intervals.

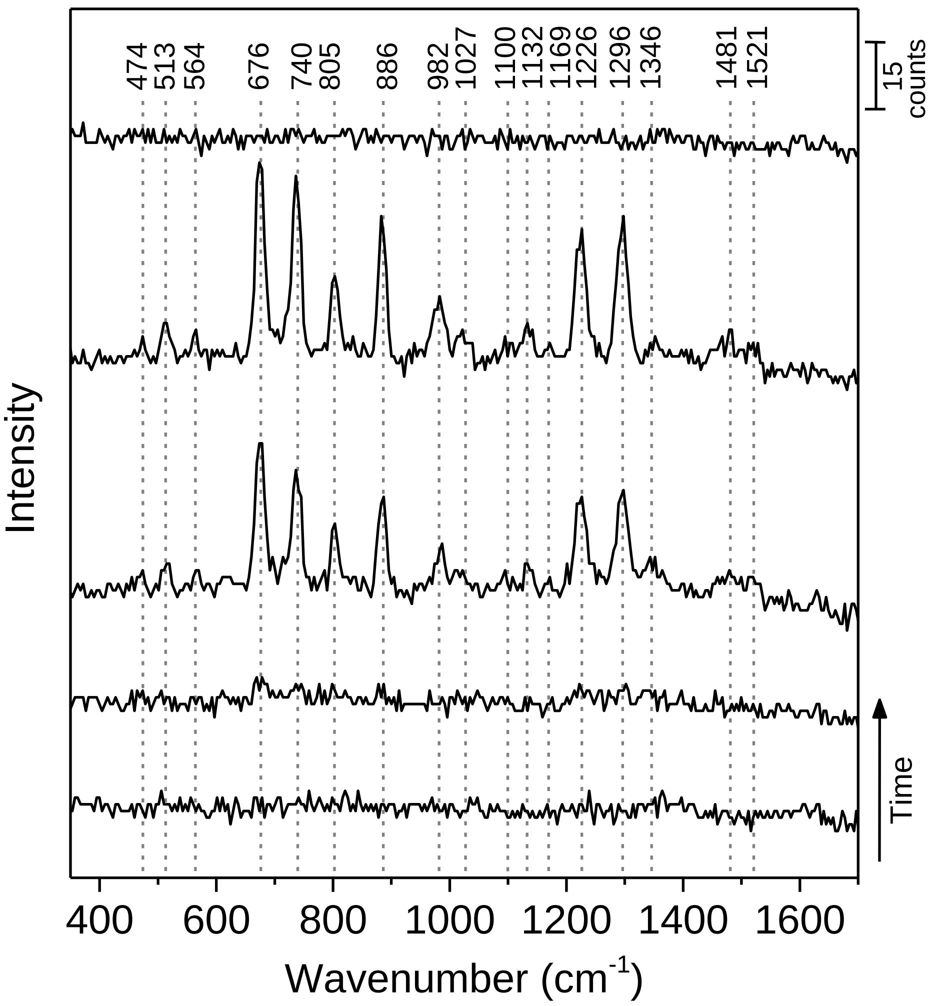

Figure A22: Time-series SERS spectrum of *c*-AB1 in 40 ms intervals.

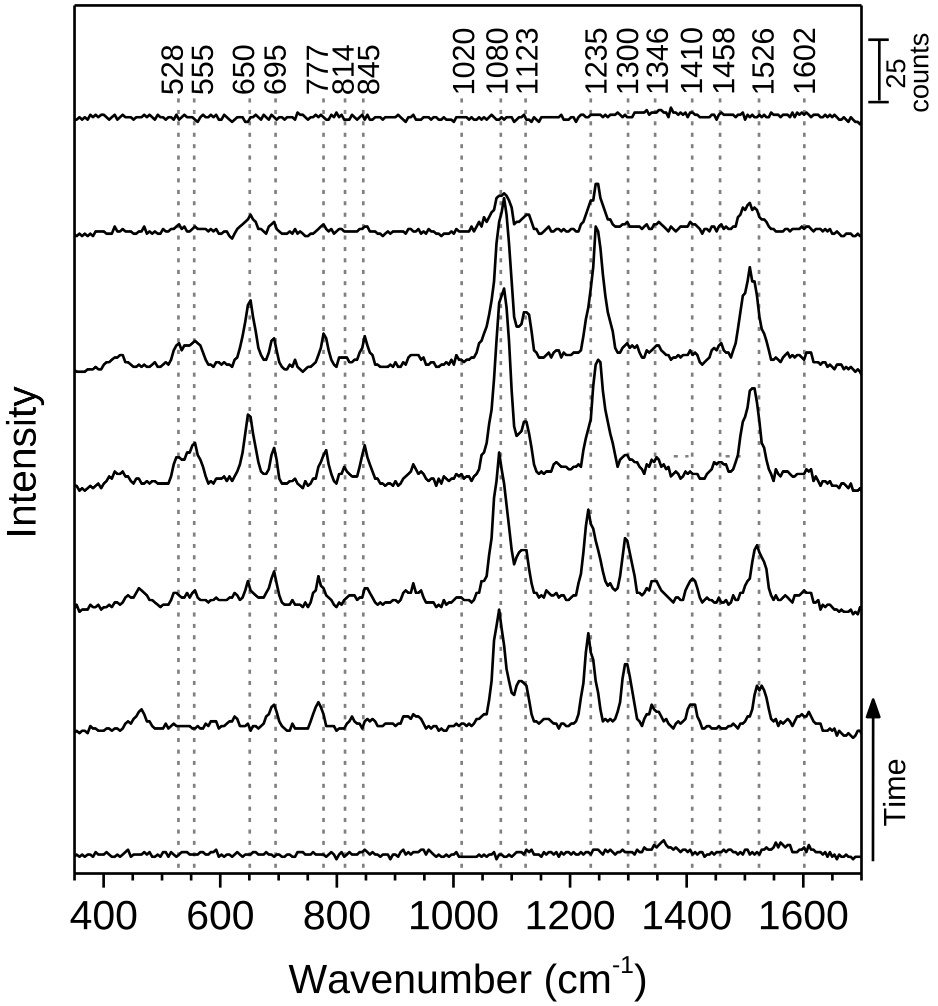

Figure A23: Time-series SERS spectrum of *c*-AB1 in 40 ms intervals.

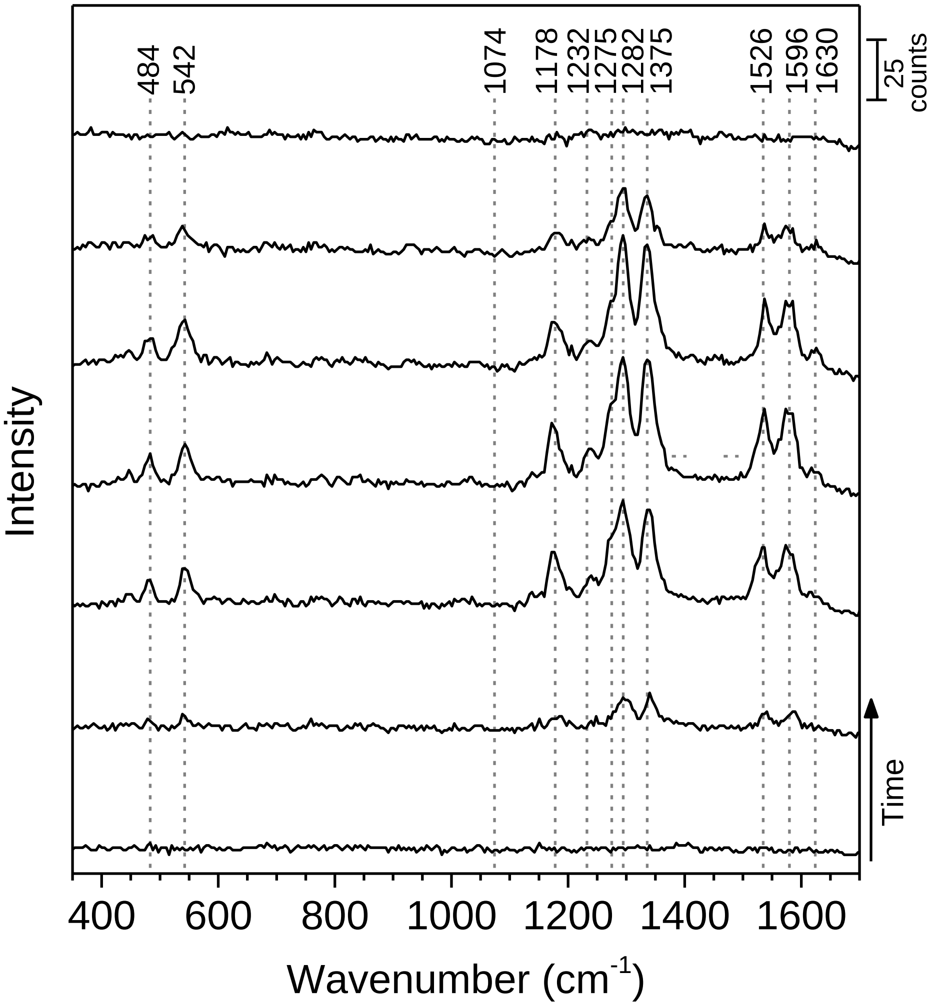

Figure A24: Time-series SERS spectrum of *c*-AB1 in 40 ms intervals.

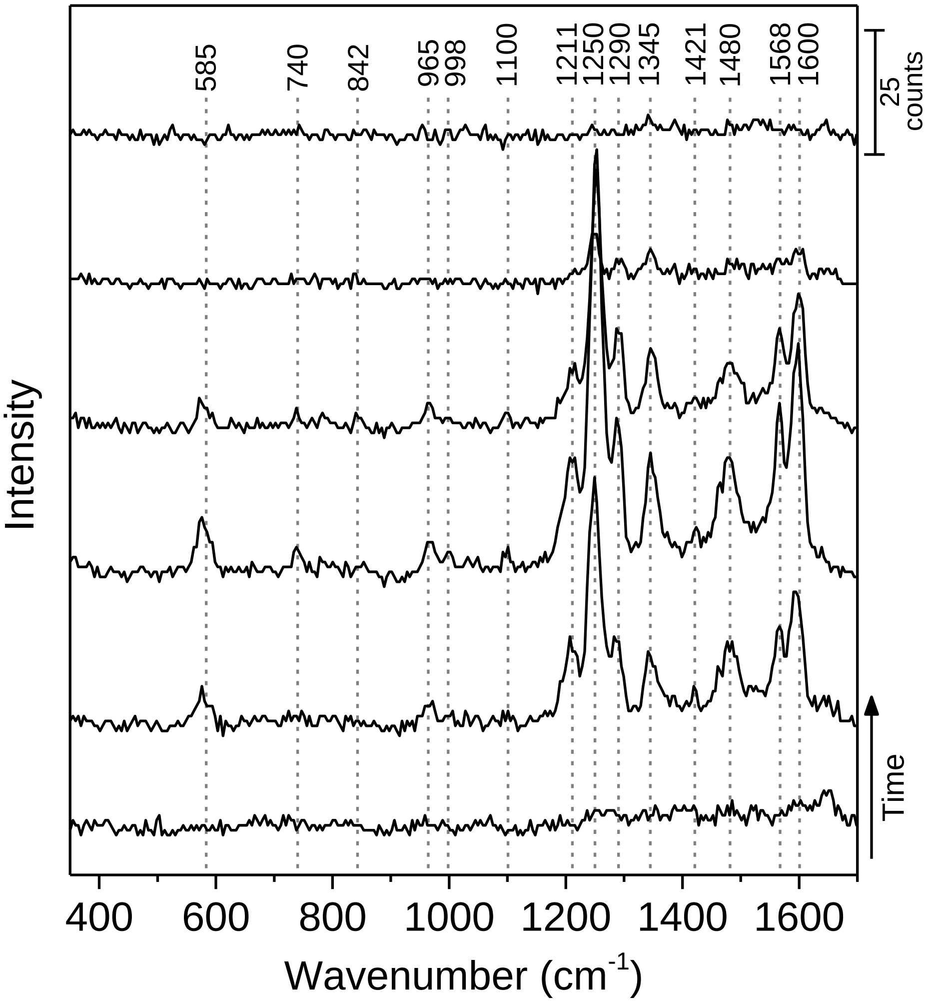

Figure A25: Time-series SERS spectrum of *c*-AB2 in 40 ms intervals.

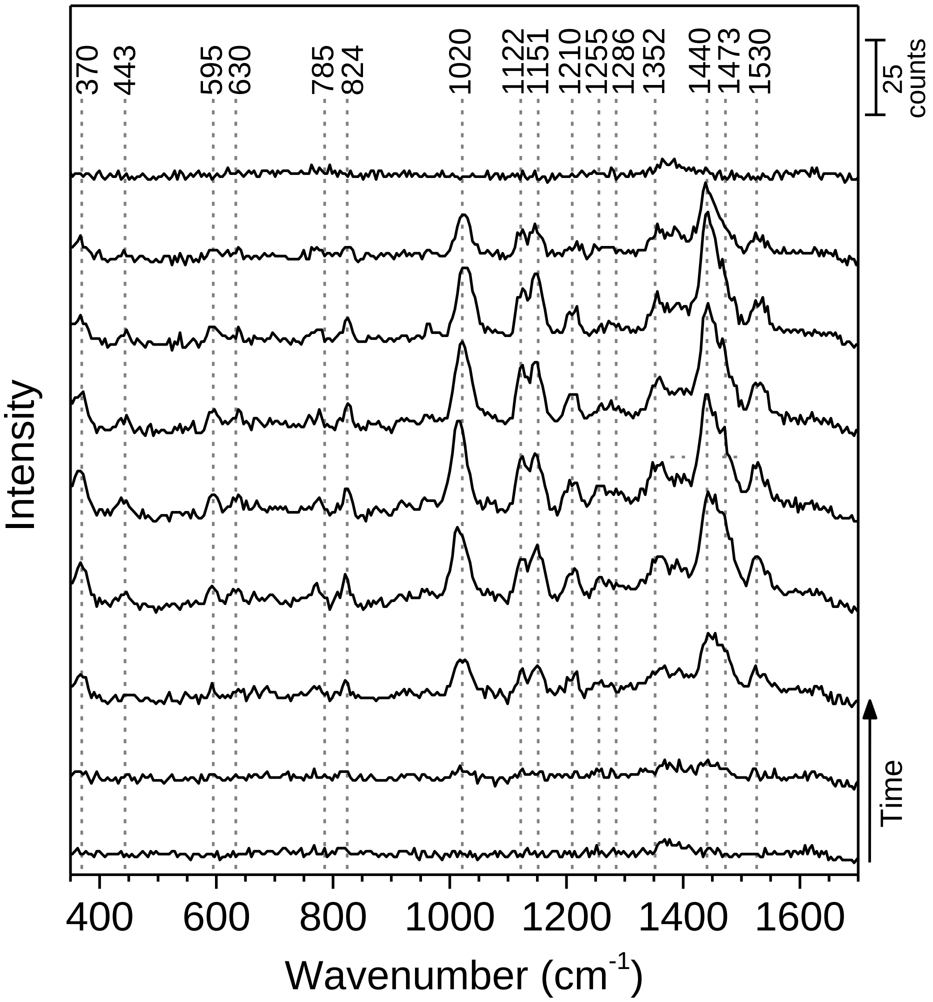

Figure A26: Time-series SERS spectrum of *c*-AB2 in 40 ms intervals.

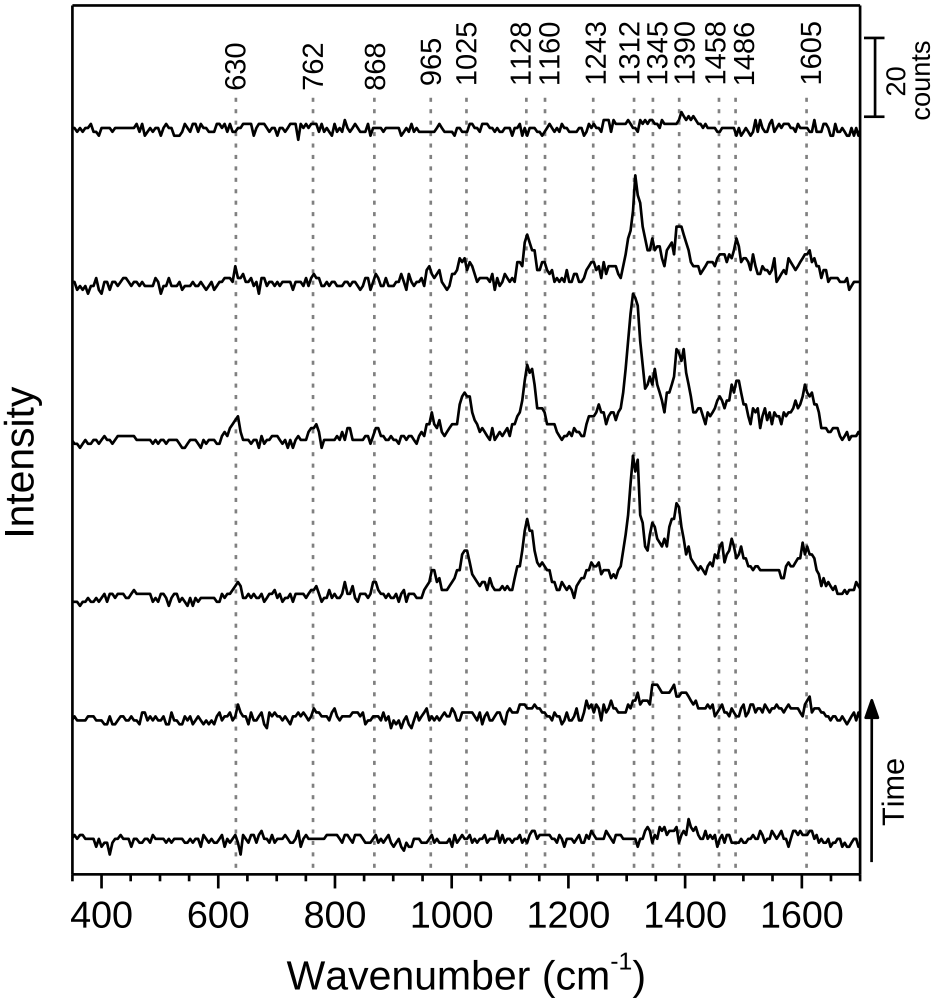

Figure A27: Time-series SERS spectrum of *c*-AB2 in 40 ms intervals.

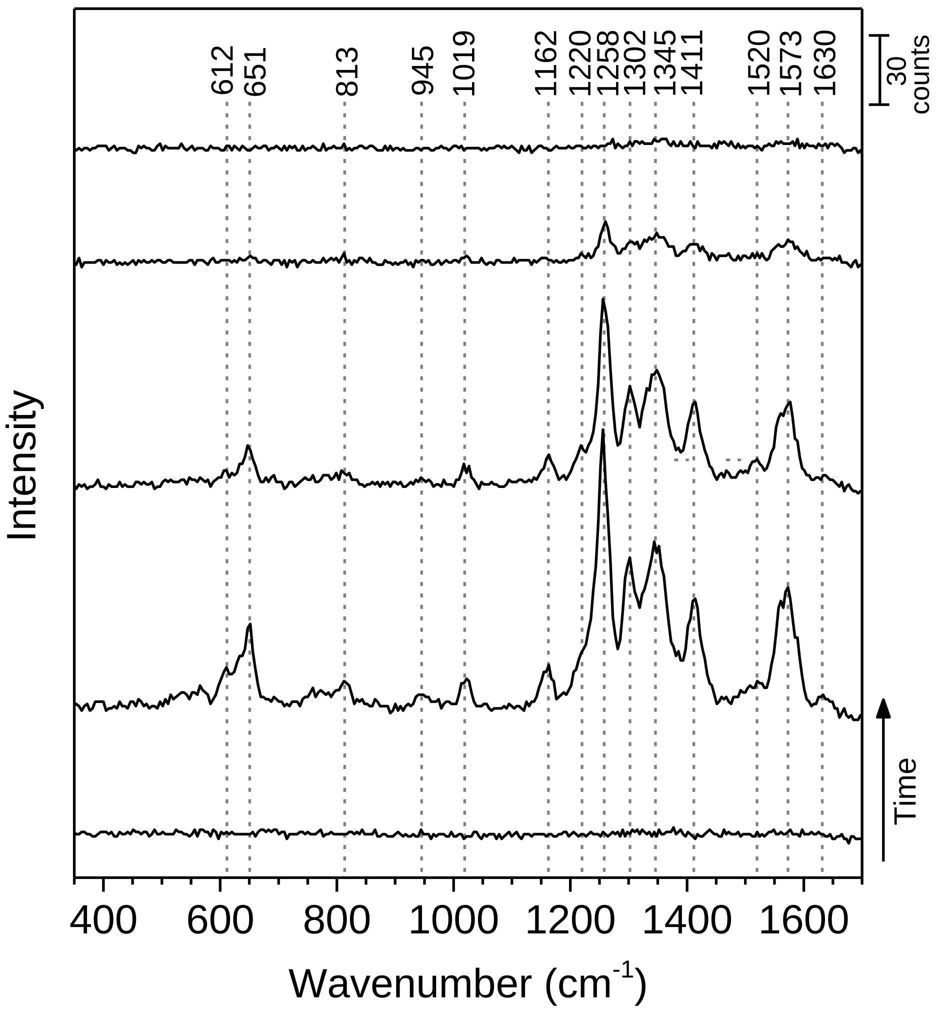

Figure A28: Time-series SERS spectrum of *c*-AB2 in 40 ms intervals.

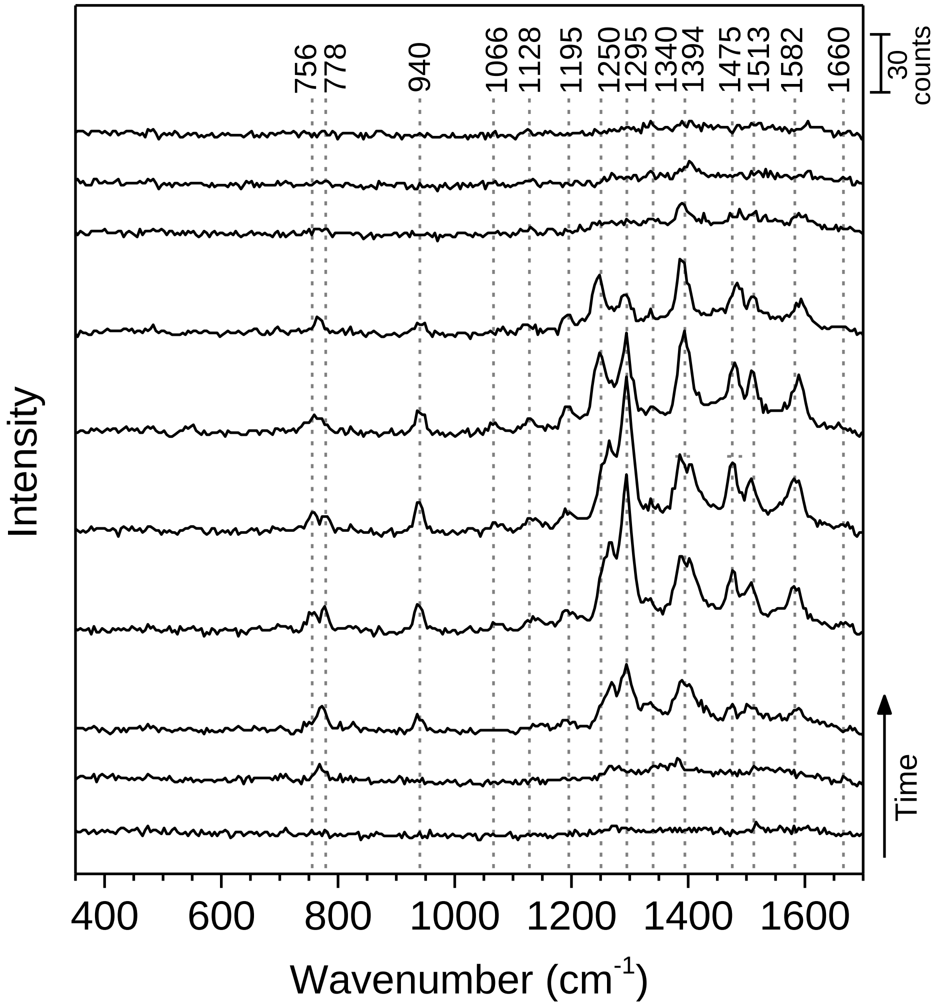

Figure A29: Time-series SERS spectrum of *c*-AB2 in 40 ms intervals.

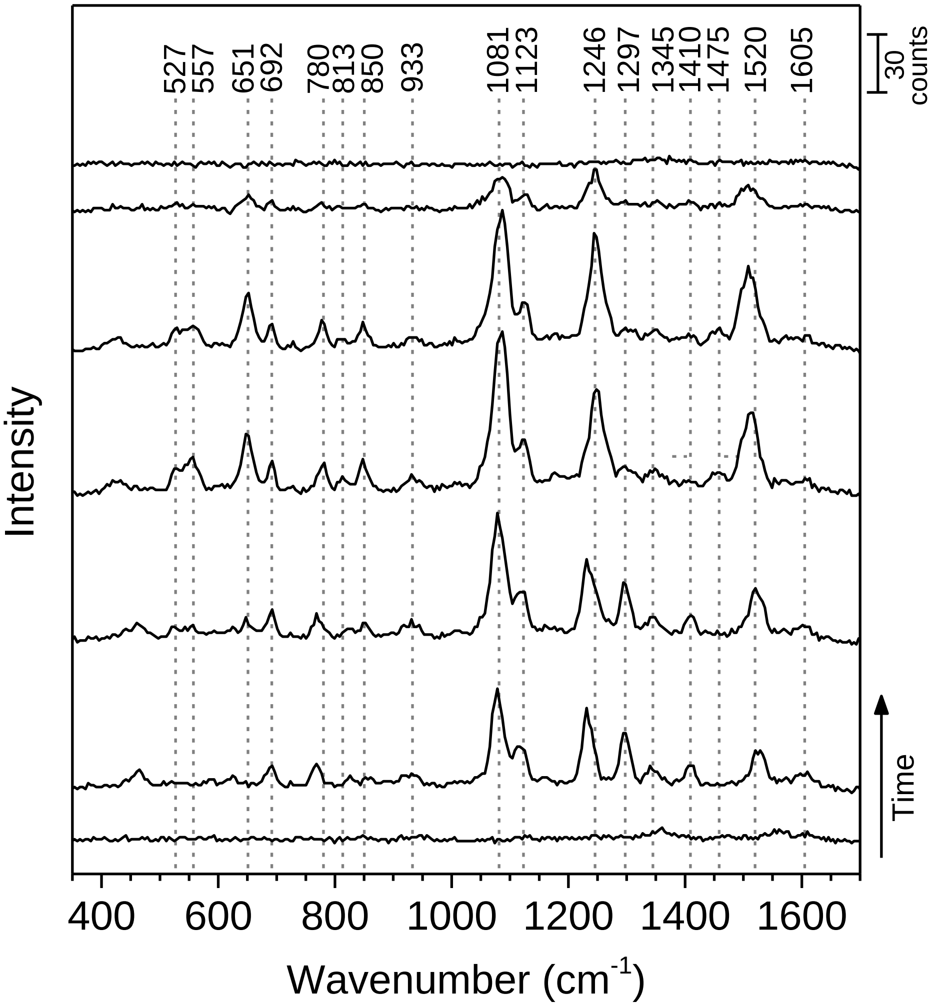

Figure A30: Time-series SERS spectrum of *c*-AB2 in 40 ms intervals.

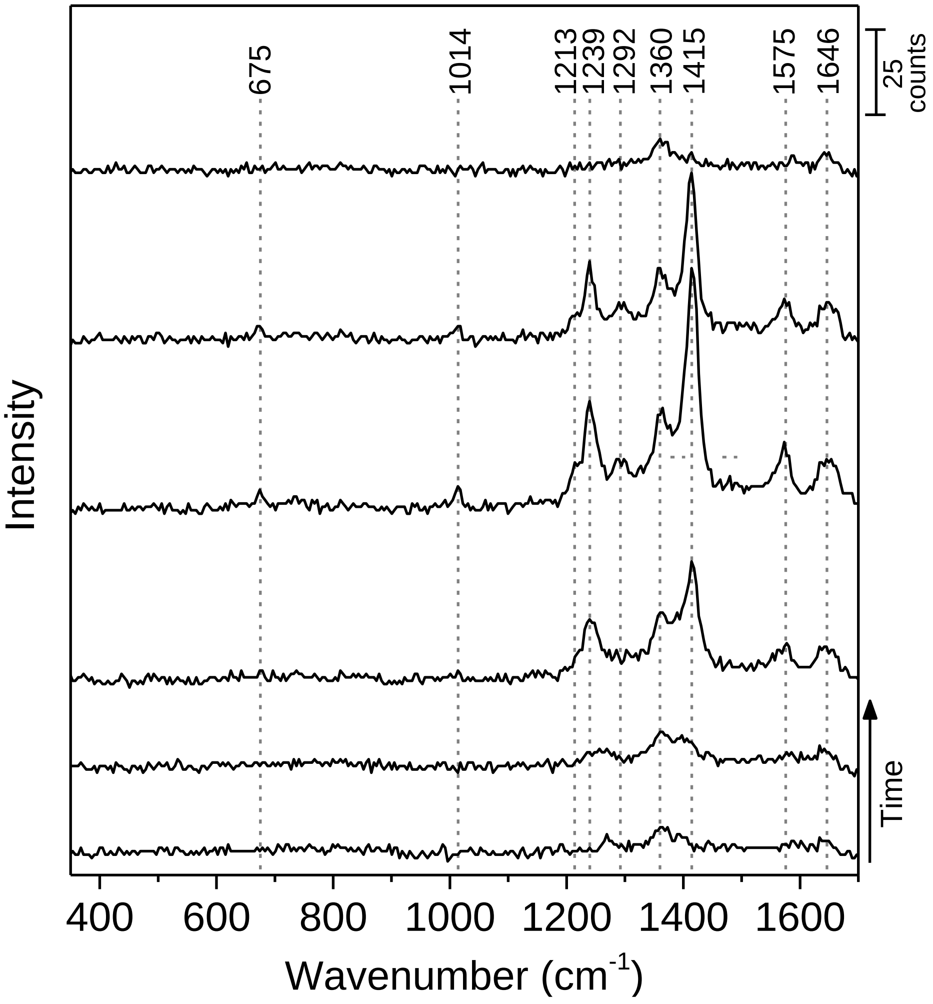

Figure A31: Time-series SERS spectrum of *c*-AB3 in 40 ms intervals.

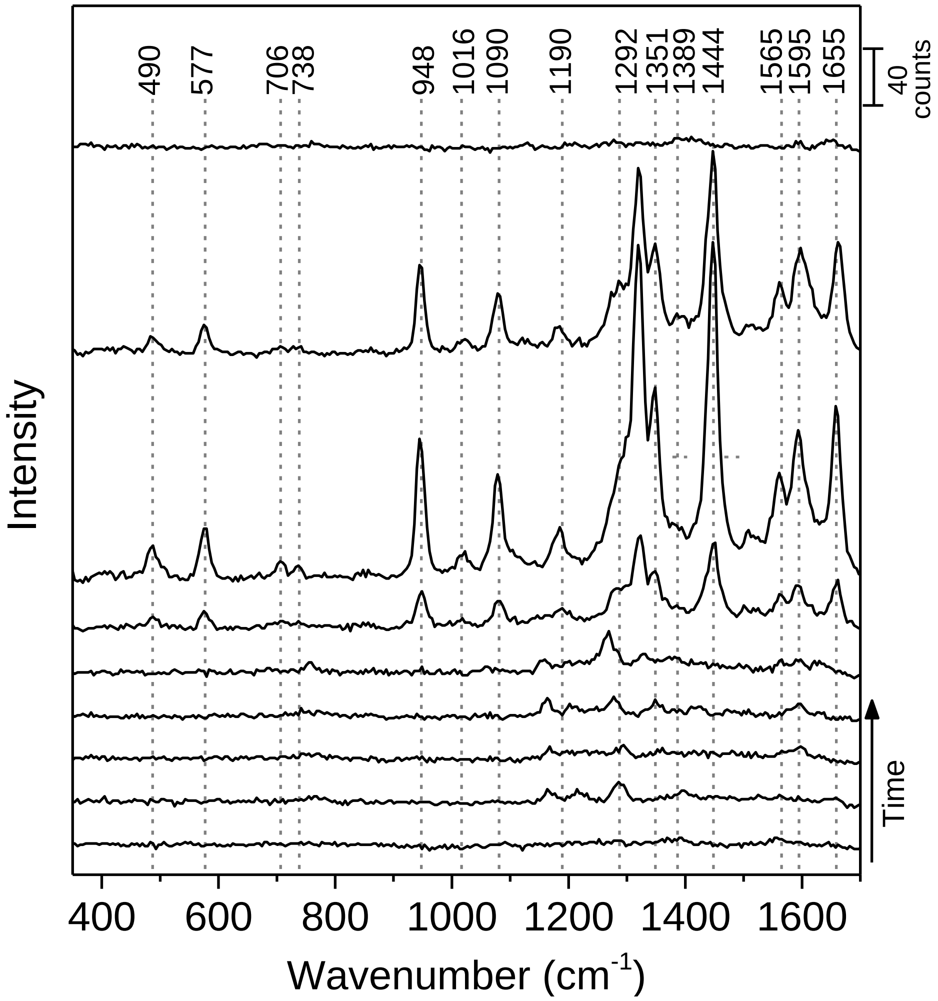

Figure A32: Time-series SERS spectrum of *c*-AB3 in 40 ms intervals.

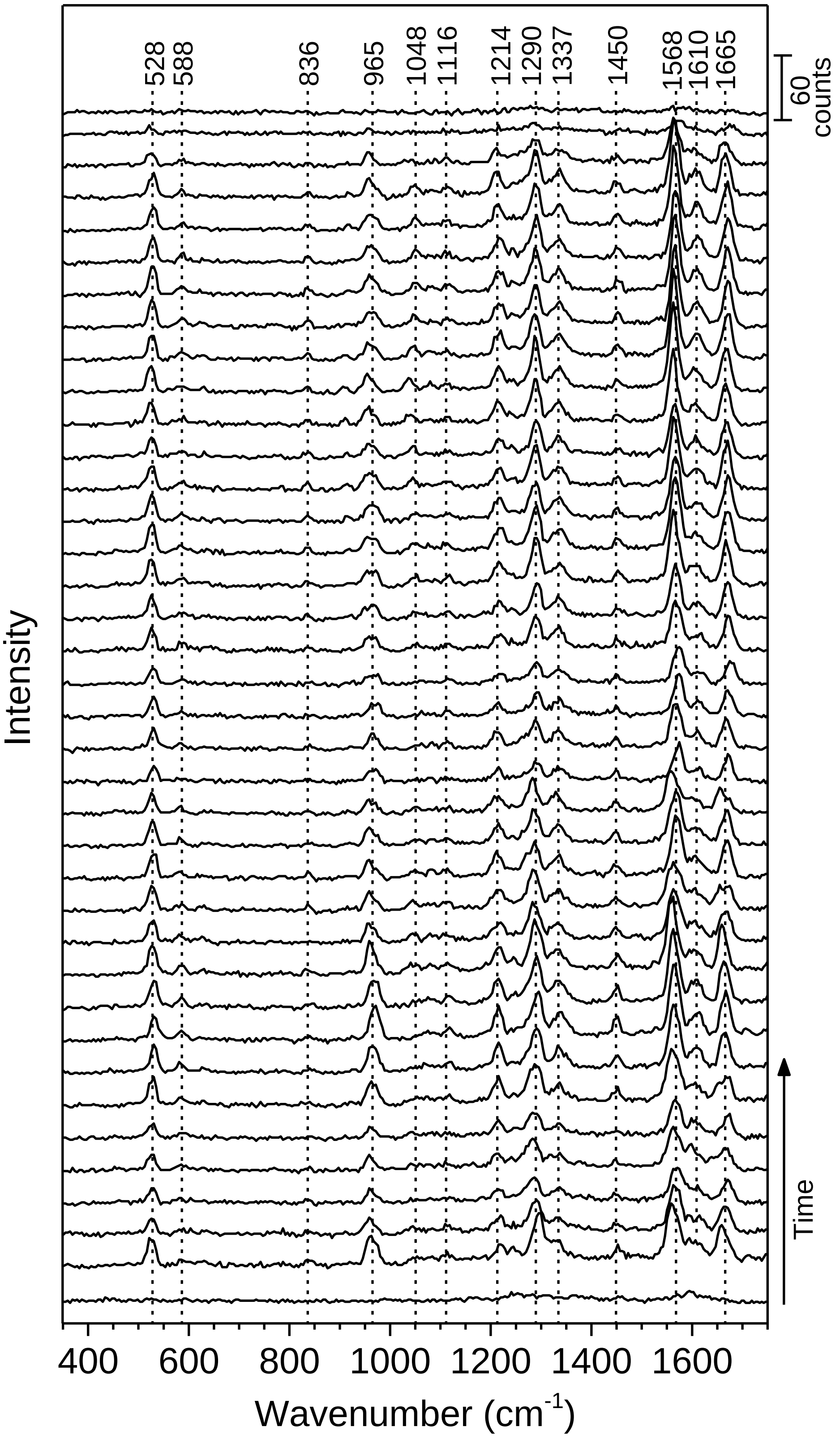

Figure A33: Time-series SERS spectrum of *c*-AB3 in 40 ms intervals.

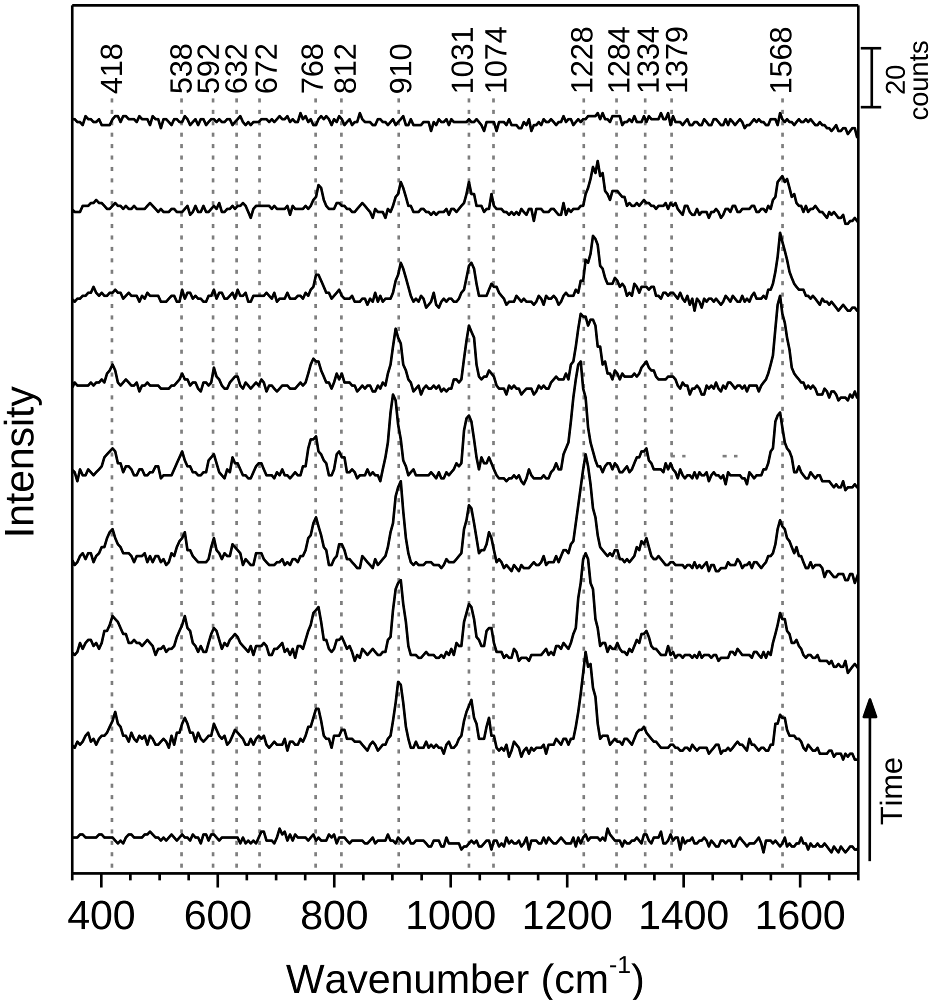

Figure A34: Time-series SERS spectrum of *c*-AB3 in 40 ms intervals.

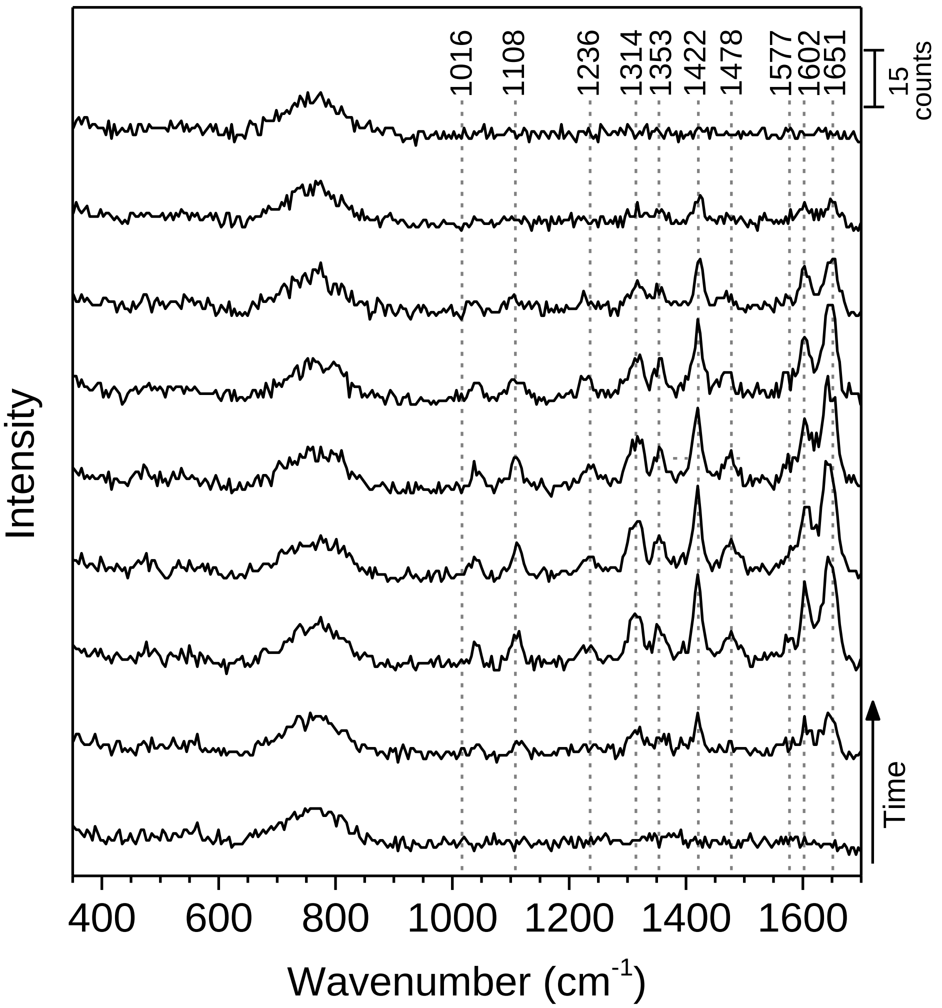

Figure A35: Time-series SERS spectrum of *c*-AB3 in 40 ms intervals.

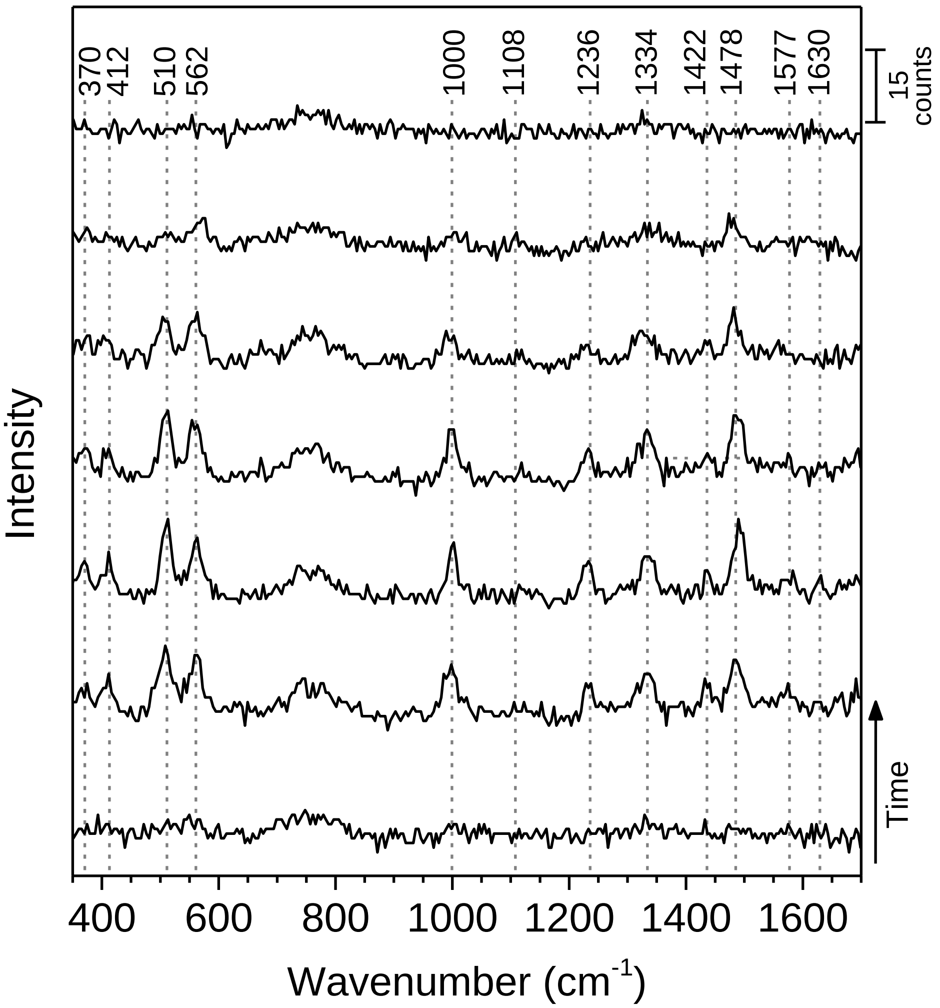

Figure A36: Time-series SERS spectrum of *c*-AB3 in 40 ms intervals

VITA

ÇAĞRI ÖZGE TOPAL

Candidate for the Degree of

Doctor of Philosophy

Dissertation: ADSORPTION AND SWITCHING OF SINGLE AZOBENZENE MOLECULES AT SILVER NANOHEMISPHERE FACETS STUDIED BY SURFACE−ENHANCED RAMAN SCATTERING

Major Field: Mechanical Engineering

Biographical:

Education:

Completed the requirements for the Doctor of Philosophy in Mechanical and Aerospace Engineering at Oklahoma State University, Stillwater, Oklahoma in July, 2019.

Completed the requirements for the Master of Science in Mechanical and Aerospace Engineering at Oklahoma State University, Stillwater, Oklahoma in 2010.

Completed the requirements for the Bachelor of Science in Mechanical Engineering at Dokuz Eylul University, Izmir, Turkey in 2006.

Experience:

Graduate Teaching and Research Associate at the School of Mechanical and Aerospace Engineering, Oklahoma State University, Stillwater, Oklahoma from May, 2008 through May, 2019.

Instructor at College of Engineering, Architecture and Technology, Oklahoma State University, Stillwater, Oklahoma from August, 2017 through May, 2018.

Professional Memberships:

American Chemical Society (ACS)